

**Optical Studies of Ultrafast Carrier  
Dynamics in Semiconducting Materials**

A thesis presented

by

Peter Ney Saeta

to

The Department of Physics

in partial fulfillment of the requirements

for the degree of

Doctor of Philosophy

in the subject of

Physics

Harvard University

Cambridge, Massachusetts

May 1991

© 1991 by Peter Ney Saeta  
All rights reserved

## Abstract

This thesis describes three experiments using pump-probe spectroscopy with picosecond and femtosecond laser pulses to study carrier dynamics in semiconductors. In the first experiment, highly excited gallium arsenide is studied with reflectivity and reflection second-harmonic probes using 160-fs pulses at 623 nm. Above a threshold incident fluence of  $\sim 0.1 \text{ J/cm}^2$ , the second-harmonic signal is observed to fall to zero in 100 fs. This drop shows that the valence electrons undergo a transformation to a centrosymmetric configuration and strongly suggests that the atomic lattice disorders before acquiring appreciable energy from the pulse. With an exponential time of 200 fs the reflectivity rises to a steady high value that is consistent with a metallic molten phase. Tens of picoseconds after excitation, the reflectivity drops considerably from the high value of the liquid and probe light is increasingly scattered out of the plane of incidence. The excitation produces  $\sim 90$ -nm-deep pits in the wafer surface that are covered with a layer of solidified droplets. An estimate of the absorption and scattering caused by a cloud of liquid droplets ejected from the surface suggests that ablated material can account for the reflectivity drop.

In the second experiment, femtosecond transient absorption spectroscopy is used to study the carrier dynamics of type II GaAs/AlAs multiple quantum wells. The spectra show a rapid partial recovery in the pump-induced bleaching near the absorption edge that is produced by the rapid scattering of conduction electrons in the  $\Gamma$  valley of the GaAs layers to the X valleys of the AlAs barrier layers. The scattering time is measured to be 100 fs for an 8-monolayer sample and 400 fs for an 11-monolayer sample.

In the third experiment, the picosecond laser melting of silicon is studied using a streak camera to provide spatial and temporal resolution. The reflectivity near Brewster's angle shows the expected eightfold increase following melting. Images of the excited silicon surface emphasize the importance of spatial resolution in near-threshold experiments.

## Acknowledgments

From the moment I joined his group, I have seen but one side of Professor Eric Mazur: the positive, enthusiastic one. Through the inevitable disappointments of equipment failure and lack of experimental progress, I could always count on Eric's encouragement, dedication, and friendship. His drive to understand the essence of physical problems infects all the members of his group and has made for many a lively lunchtime discussion. His attention to detail and the clarity of his lectures, writing, and talks serves as inspiration for my current and future endeavors. To him I owe an immense debt of gratitude, not only for his guidance in scientific work, but also for squash games, concerts, ski outings, compact disc recommendations, and an addiction to the Macintosh.

My thanks go also to the members of the Quantum Electronics and Molecular Physics group, who have made graduate work enriching, entertaining, and enjoyable. Special thanks go to Juen-Kai Wang for his unfailing enthusiasm, his expertise in electronics and lasers, his help with Chinese pronunciation, his dedication and scholarship, and for his inimitable belly laugh. Would that I could follow some of the jokes in the original Mandarin. I am grateful for the camaraderie and tidbits of shared experimental knowhow I received from the senior members of the group: Jyhpyng Wang, Kuei-Hsien Chen, Luis Avilés, and Doo Soo Chung. I wish to thank Maarten Buijs for his many contributions to the silicon work and the development of the femtosecond laser system. Thanks also to Ka Yee Lee for encouragement, memorable discussions, excellent stewardship at Dim Sum outings, and the opportunity to hone my data-recovery skills. Cheng-Zai Lü freely shared his considerable experimental expertise and provided interesting insights into Chinese medicine and

history. It has been a great pleasure to work with Yakir Siegal on both computational and experimental projects; besides his invariable optimism, I appreciate especially his help in managing some of the group's computer tasks. Thanks also to Jay Goldman and Shrenik Deliwala who offered helpful suggestions on papers and participated in innumerable discussions on everything from physics to Indian politics to tropical fish to Saddam Hussein.

I thank Nicolaas Bloembergen for many helpful suggestions and contributions to the understanding of the experiments. Our discussions have always helped clarify for me the essential physics. William Paul and Bertrand Halperin offered many useful suggestions for improving the manuscript. I wish also to thank Marco Malvezzi for his help with the research for my oral examination and for his interest in and contributions to our experimental work.

Emil Sefner, Louis DeFeo, and David Osier in the McKay machine shop helped immensely by making many pieces of equipment for the experiments, and even teaching me some rudimentary machining skills. And I would like to express to Elizabeth Hemingway my appreciation for her great kindness, including the weekly teas which bring together the different groups in the McKay Laboratory.

My experimental work was greatly facilitated by support from AT&T Bell Laboratories through the Ph.D. Fellowship program. Not only did the program support me at Harvard, it also made possible an enjoyable summer's collaboration with Ben Greene. I would also like to thank Hamamatsu Photonics for the picosecond streak camera, which was used in the time-resolved silicon melting experiment.

Bern Kohler and Niki Steckler helped bring a little family to my life at Harvard before Linda graduated. I'll always remember our theater outings, Thanksgivings, porch parties, and scotch tastings together. Mike Montgomery shared his considerable enthusiasm for complex variables, nonlinear dynamics, atmospheric science, and good beer.

Most importantly, my great thanks go to my entire family for support and encouragement throughout my years at Harvard. I never would have made it without their help. Brennan's arrival has made this past year especially fulfilling and he has been a most pleasant diversion from thesis-writing. And finally, my heartfelt thanks to my wife, Linda, for her support, her help, her love, and her conviction that this little opus *would* be finished on time.

To Steve

# Contents

<b>Abstract</b>	<b>iii</b>
<b>Table of Contents</b>	<b>v</b>
<b>List of Figures</b>	<b>viii</b>
<b>Acknowledgments</b>	<b>xi</b>
<b>1 Optical Studies of Carrier Dynamics in Semiconductors</b>	<b>1</b>
1.1 Interaction of Light with Semiconductors . . . . .	3
1.1.1 Propagation . . . . .	3
1.1.2 Reflection and Refraction . . . . .	3
1.1.3 Reflection Second-Harmonic Generation. . . . .	6
1.1.4 Photoexcited Carriers. . . . .	7
1.1.5 Nonlinear Absorption. . . . .	10
1.2 Drude Model . . . . .	11
1.3 Scattering Processes . . . . .	15
1.3.1 Carrier-Carrier Scattering in GaAs . . . . .	17
1.3.2 Carrier-Phonon Scattering. . . . .	19
1.3.3 Carrier Recombination . . . . .	22
1.3.4 High Density Effects . . . . .	24
1.4 Laser Annealing. . . . .	26
1.5 Overview of This Thesis. . . . .	28
<b>2 Amplified Femtosecond Dye Laser</b>	<b>31</b>
2.1 CPM Oscillator . . . . .	33

2.1.1	CPM Laser Components . . . . .	34
2.1.2	Initial Alignment . . . . .	40
2.1.3	Daily Operation . . . . .	47
2.2	Amplifier . . . . .	48
2.2.1	Prism Dye Cells . . . . .	50
2.2.2	Pumping. . . . .	55
2.2.3	Relay Imaging . . . . .	56
2.2.4	Setup and Alignment Procedure. . . . .	57
2.3	Pulse Compression . . . . .	59
2.4	Autocorrelation . . . . .	61
2.4.1	Angle Broadening of the Autocorrelation . . . . .	64
2.5	Conclusion . . . . .	68
<b>3</b>	<b>Femtosecond Laser Melting of GaAs</b>	<b>69</b>
3.1	Introduction . . . . .	69
3.2	Laser Setup . . . . .	74
3.3	Experimental . . . . .	75
3.4	Results from a (100) Surface . . . . .	78
3.5	Results from a (110) Surface . . . . .	82
3.6	Discussion of Short Time Results. . . . .	86
3.6.1	Reflectivity Rise . . . . .	94
3.6.2	Lattice Heating. . . . .	98
3.6.3	Lattice Disorder . . . . .	99
3.7	Reflectivity Drop . . . . .	102
3.8	Scattering of Probe Light. . . . .	104
3.9	Ablation of Material . . . . .	106
3.10	Surface Morphology. . . . .	107
3.11	Discussion of the Reflectivity Drop. . . . .	107
3.11.1	Evaporation . . . . .	109
3.11.2	Mie Scattering . . . . .	111

3.12	Conclusions. . . . .	.113
<b>4</b>	<b>Interlayer Transport of Photoexcited Carriers in Type II Multiple Quantum Well Structures</b>	<b>115</b>
4.1	Introduction . . . . .	.115
4.1.1	Semiconductor Heterostructures. . . . .	.116
4.1.2	Quantum Wells . . . . .	.116
4.2	Multiple Quantum Well Samples . . . . .	.118
4.3	Luminescence Excitation Spectra . . . . .	.120
4.4	Femtosecond Transient Absorption Spectroscopy . . . . .	.122
4.4.1	Differential Absorption Spectra . . . . .	.123
4.4.2	Time-resolved Differential Absorption Spectra . . . . .	.125
4.5	Discussion . . . . .	.128
4.5.1	Quantum-Confined Stark Effect . . . . .	.131
4.5.2	Scattering Rate Dependence on Well Thickness . . . . .	.132
4.6	Conclusions. . . . .	.136
<b>5</b>	<b>Picosecond Laser Melting of Silicon</b>	<b>138</b>
5.1	Experimental Technique. . . . .	.140
5.2	Results and Discussion . . . . .	.143
5.3	Conclusions. . . . .	.143
<b>A</b>	<b>Computer Model for Picosecond Laser Melting of Silicon</b>	<b>147</b>
A.1	Physical Model . . . . .	.148
A.2	Numerical Method . . . . .	.150
A.3	Material Properties . . . . .	.154
A.4	Results . . . . .	.156
A.5	Possible Improvements . . . . .	.159
	<b>Concluding Remarks</b>	<b>160</b>
	<b>References</b>	<b>162</b>

# List of Figures

1.1	Reflectivity of crystalline Si at 532 nm vs. incidence angle . . . . .	6
1.2	Electronic band structure of GaAs . . . . .	9
1.3	Carrier scattering processes . . . . .	15
1.4	Time scales for carrier interactions and thermal processes. . . . .	16
1.5	Electron-phonon scattering processes in semiconductors . . . . .	20
2.1	Overview of amplified femtosecond dye laser system. . . . .	32
2.2	CPM laser oscillator . . . . .	35
2.3	Dye circulation system . . . . .	37
2.4	Range of CPM lasing wavelengths . . . . .	38
2.5	Spectrum of CPM laser for various pulse durations . . . . .	39
2.6	Simple oscillator without absorber jet or prisms . . . . .	40
2.7	Aligning the prisms . . . . .	43
2.8	Rotating-arm autocorrelator . . . . .	45
2.9	Geometry of rotating-arm autocorrelator . . . . .	46
2.10	Overview of 10-Hz amplifier . . . . .	49
2.11	Prism dye cell . . . . .	51
2.12	Gain profile of a prism dye cell with Gaussian pumping . . . . .	53
2.13	Modified prism dye cell . . . . .	54

2.14	Relay imaging . . . . .	57
2.15	Grating pulse compressor . . . . .	60
2.16	Intensity autocorrelation. . . . .	61
2.17	Large-angle autocorrelation . . . . .	64
2.18	Pulse-broadening geometry . . . . .	65
2.19	Autocorrelation of the amplified pulses . . . . .	67
3.1	Experimental setup . . . . .	76
3.2	Detail of (100) probing geometry . . . . .	77
3.3	Relative <i>p</i> -polarized reflectivity from a (100) GaAs surface . . . . .	79
3.4	Relative second-harmonic intensity from a (100) surface . . . . .	80
3.5	Polarization rotation effect. . . . .	82
3.6	Factors producing rise in SHG on a (100) surface. . . . .	83
3.7	Detail of (110) geometry . . . . .	84
3.8	Relative <i>s</i> -polarized reflectivity from a (110) GaAs surface. . . . .	85
3.9	Relative second-harmonic intensity from a (110) GaAs surface. . . . .	86
3.10	Fluence dependence at 120-fs delay of a (110) GaAs surface . . . . .	87
3.11	Time dependence for a (110) GaAs surface at $F = 0.33 \text{ J/cm}^2$ . . . . .	88
3.12	Fluence dependence of the $1/e$ response time for a (110) GaAs surface . . . . .	89
3.13	Second-harmonic response time with convolution . . . . .	90
3.14	Vertical 2.0-eV transitions in GaAs . . . . .	91
3.15	Density of states of crystalline GaAs . . . . .	92
3.16	Dielectric constant and index of refraction vs. ionization fraction . . . . .	96
3.17	Free carrier density of molten GaAs . . . . .	97
3.18	Reflectivity drop at long time . . . . .	103
3.19	Scattering of probe light. . . . .	105

3.20	Depth of pits created by femtosecond laser excitation . . . . .	.106
3.21	Electron micrographs of the GaAs surface after laser excitation . . . . .	.108
3.22	Mie scattering. . . . .	.112
4.1	Semiconductor heterostructure band alignments . . . . .	.118
4.2	Recombination energies in GaAs/AlAs quantum wells. . . . .	.119
4.3	Low temperature cw luminescence spectrum of the 11-monolayer sample . . . . .	.121
4.4	Differential absorbance spectra of the 11-monolayer sample . . . . .	.124
4.5	Setup for time-resolved differential absorption measurements . . . . .	.125
4.6	Transient absorption spectrum of the 11-monolayer sample . . . . .	.127
4.7	Transient absorption spectrum of the 8-monolayer sample . . . . .	.128
4.8	Absorbance spectra of the 11-monolayer sample . . . . .	.129
4.9	GaAs and AlAs effective masses and band offsets. . . . .	.133
5.1	<i>p</i> -polarized reflectivity of crystalline and molten silicon . . . . .	.140
5.2	Experimental setup for picosecond melting studies . . . . .	.141
5.3	Streak camera images of the melting silicon surface. . . . .	.144
5.4	Reflectivity of silicon during picosecond laser melting . . . . .	.145
A.1	Temperature vs. time at near-threshold excitation of silicon . . . . .	.157
A.2	Temperature vs. time of a silicon surface at $0.25 \text{ J/cm}^2$ . . . . .	.158

# Chapter 1

## Optical Studies of Carrier Dynamics in Semiconductors

Semiconductors currently lie at the heart of the technology of the information age. The possibility to control and to modify their electrical properties with great precision gives them unsurpassed versatility for device fabrication. From rooms full of vacuum tubes to provide primitive computational power we have progressed to computers on a small chip of silicon. With miniaturization have come both power and flexibility. And with power comes the desire for even greater power and speed. As devices continue to shrink, fundamental material response times begin to limit performance. This thesis addresses the physical processes occurring in semiconductors on the fastest time scales.

Short laser pulses provide the means to study these ultrafast processes. They are able both to deliver excitation energy to semiconductors and to probe the material response to the excitation. The absorption of photons from the excitation laser pulse produces electron-hole pairs in the semiconductor. These charge carriers interact with each other, with lattice vibrations, and with the radiation field in a vari-

ety of processes before electrons and holes eventually come back together and recombine.

This thesis describes three short-pulse optical experiments on semiconducting materials. In two of these, an intense laser pulse is used to excite and melt a thin layer of material at the surface. Under irradiation with a 30-ps pulse, a silicon surface is observed to melt when energy from the incident laser beam heats the material to the melting temperature and supplies the latent heat of fusion, in agreement with the thermal model of laser annealing. Experiments on gallium arsenide surfaces using 160-fs pulses, however, reveal a phase transformation of the material near the surface in a time that is short compared to the lattice heating time. Under strong electronic excitation, the crystal lattice disorders while still cold. This differs from the majority of laser melting studies of semiconductors in which the onset of atomic disorder can be attributed to a lattice temperature rise.

In the third experiment, transient absorption spectroscopy is used to study the response of type II GaAs/AlAs multiple quantum well structures to femtosecond excitation above the absorption edge. An initial bleaching of the absorption around the energy of the injected electrons is observed to recover partially on a subpicosecond time scale. The partial recovery demonstrates that electrons injected by the excitation pulse into the conduction band of the GaAs layers scatter rapidly into the adjacent AlAs barrier layers.

Common to all the experiments is the interaction of short laser pulses with electrons in semiconductors. In this chapter, some basic aspects of this interaction are discussed. This is followed by a description of the scattering mechanisms that determine the dynamics of the photoexcited carriers. Next the high-excitation regime of laser annealing is described. The chapter concludes with an overview of the experiments described in this thesis.

## 1.1 Interaction of Light with Semiconductors

### 1.1.1 Propagation

The propagation of light in a non-magnetic linear absorbing medium is governed by the medium's (complex) index of refraction  $n = n_R + in_I = \sqrt{\epsilon}$ , where  $\epsilon$  is the frequency-dependent dielectric constant.<sup>1</sup> The real part of the index gives the factor by which the phase velocity is reduced in the medium, and the imaginary part is proportional to the rate of energy loss. For a plane wave of vacuum wavelength  $\lambda$  traveling in the  $z$ -direction, the intensity of the wave is reduced according to the expression

$$I(z) = I_0 e^{-\alpha z} , \quad (1.1)$$

where the absorption constant  $\alpha$  represents the spatial rate at which the wave loses energy. In terms of the imaginary part of the refractive index, it is given by

$$\alpha = \frac{4\pi n_I}{\lambda} . \quad (1.2)$$

The absorption constant can be quite large for energies above the gap. Its inverse, the absorption depth  $\alpha^{-1}$ , sets the length scale for an optical probe. As an example, for the 623-nm pump light used in the GaAs melting experiment of Chapter 3, the index of refraction of crystalline GaAs is  $3.873 + 0.207i$ , [Palik 1985] giving an absorption depth of  $\alpha_{623}^{-1} = 230 \text{ nm}$ .

### 1.1.2 Reflection and Refraction

---

<sup>1</sup> Gaussian units are used throughout this thesis. The tensorial character of the dielectric constant is ignored in this discussion, as is appropriate for cubic and isotropic media. See *e.g.* Jackson 1975, Chapter 4.

section, light is reflected and refracted to a degree that depends upon the direction and polarization of the incident beam and on the relative index of refraction of the two media. Boundary conditions obtained from Maxwell's equations apply to the fields at each point in the plane of the interface. In order for these boundary conditions to be satisfied, a necessary, but not sufficient, condition is that the component of the wave vector of each beam in the plane of the interface must be the same. This constraint is called the phase matching condition. It follows that the incident, reflected, and refracted beams must all lie in the same plane, which is called the plane of incidence. For the reflected beam, which travels in the same medium as the incident beam, the phase matching condition implies that the angle of reflection is equal to the angle of incidence. These angles are customarily measured with respect to the surface normal. Equating the in-plane component of the wave vector  $k = 2\pi n/\lambda$  of the two media gives Snell's law

$$n_1 \sin \theta_i = n_2 \sin \theta_r \quad . \quad (1.3)$$

In this expression,  $n_1$  is the refractive index of the medium in which the light wave is incident,  $n_2$  is the index of the medium in which the wave is transmitted, and  $\theta_i$  and  $\theta_r$  are the angles of incidence and refraction. By defining the relative index

$$n \equiv n_2/n_1 \quad (1.4)$$

Snell's law can be expressed as

$$\sin \theta_r = \frac{\sin \theta_i}{n} \quad . \quad (1.5)$$

The amplitudes of the reflected and refracted fields depend on the state of polarization of the incident beam. The reflectivity is the fraction of incident light intensity reflected at the interface and is proportional to the square of the reflected field amplitude. If the electric field lies in the plane of incidence, the beam is called *p*-polarized and the reflectivity is given by the Fresnel formula [Born 1980]

$$R_p = \left| \frac{n \cos \theta_i - \cos \theta_r}{n \cos \theta_i + \cos \theta_r} \right|^2 = \left| \frac{\tan(\theta_i - \theta_r)}{\tan(\theta_i + \theta_r)} \right|^2, \quad (1.6)$$

where Snell's law (1.5) has been used to obtain the second equality.

In the opposite case of an *s*-polarized beam with the electric field orthogonal to the plane of incidence, the intensities are

$$R_s = \left| \frac{n \cos \theta_r - \cos \theta_i}{n \cos \theta_r + \cos \theta_i} \right|^2 = \left| \frac{\sin(\theta_i - \theta_r)}{\sin(\theta_i + \theta_r)} \right|^2. \quad (1.7)$$

At normal incidence,  $\cos \theta_r \rightarrow \cos \theta_i \rightarrow 1$  and both expressions reduce to

$$R = \left| \frac{n - 1}{n + 1} \right|^2 = \frac{(n_R - 1)^2 + n_I^2}{(n_R + 1)^2 + n_I^2}. \quad (1.8)$$

As an illustration of these expressions, the *s*- and *p*-polarized reflectivities of crystalline silicon at  $\lambda = 532$  nm are plotted in Fig. 1.1.

The *s*-polarized reflectivity is a monotonically increasing function of incidence angle  $\theta_i$ . The *p*-polarized reflectivity, however, has a minimum for incidence at Brewster's angle where  $n \cos \theta_i = \cos \theta_r$ . Using Snell's law (1.3), Brewster's angle can be expressed as

$$\theta_{\text{Brewster}} = \tan^{-1}(n). \quad (1.9)$$

Light of *p*-polarization incident at Brewster's angle on a lossless dielectric is perfectly transmitted. This property has a variety of uses. For example, optics inserted at Brewster's angle in the beam path of an oscillator polarize the beam by strongly rejecting the *s*-polarized component of the field while passing without loss the *p*-polarized component. Such optics are used both in the femtosecond dye laser and in the prism pulse compressor described in Chapter 2. The Brewster minimum can also be exploited in reflectivity studies by choosing an incidence angle for the probe beam close to Brewster's angle. Changes in the dielectric response of the material shift Brewster's angle, resulting in large changes in reflectivity. Such a prob-

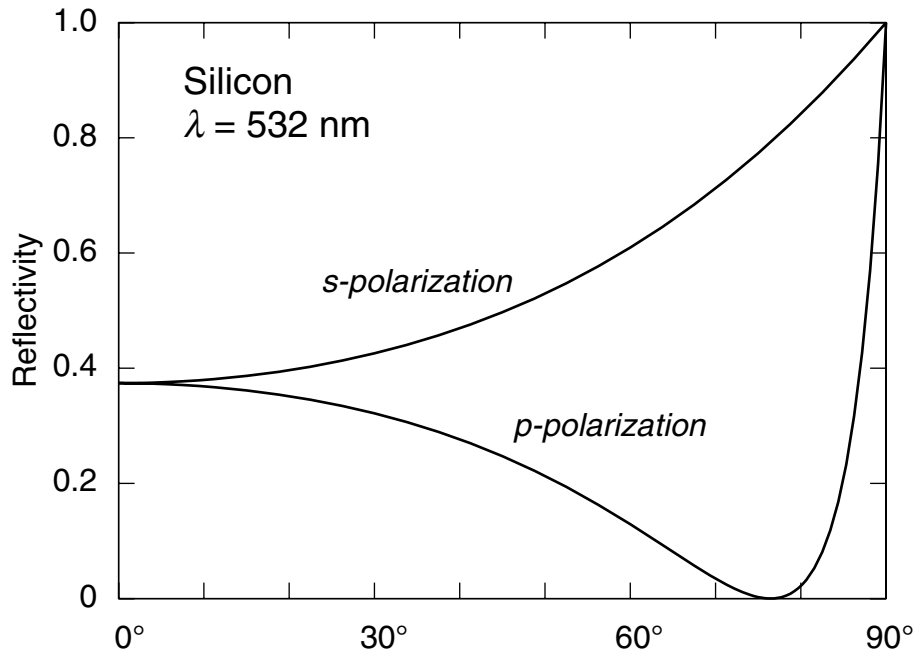


**Fig. 1.1** The *s*- and *p*-polarized reflectivity of crystalline silicon at the 532-nm wavelength of doubled Nd:YAG laser light. The index of refraction is  $4.148 + 0.044i$ , [Palik 1985] giving a reflectivity of  $2.8 \times 10^{-5}$  at Brewster's angle of  $76.4^\circ$ .

ing geometry is exploited in the picosecond laser melting studies of Chapter 5.

### 1.1.3 Reflection Second-Harmonic Generation

Whereas the linear reflectivity of media having a diagonal dielectric tensor does not contain information about the crystal symmetry, the generation of a reflected wave at the second-harmonic frequency is governed by a third-rank tensor that depends on the crystal symmetry. The theory of second-harmonic generation in reflection was developed by Bloembergen and Pershan [Bloembergen 1962] and has been used in a number of experiments on surfaces and bulk layers near the surface. [Shen 1984] Briefly, the transmitted beam at the fundamental frequency generates a nonlinear polarization at the second-harmonic frequency in the nonlinear medium.

This nonlinear polarization drives an inhomogeneous (forced) wave inside the medium. In order to satisfy Maxwell's equations at the interface, it is necessary to include a reflected second-harmonic wave. This wave is strongly peaked in the phase-matched direction, which is the direction of specular reflection of the incident light.

If the medium is transparent to radiation at the second-harmonic wavelength, the absorption constant at the fundamental wavelength sets the depth scale for a reflection second-harmonic probe. More commonly, the linear absorption constant  $\alpha$  is greater at the second-harmonic wavelength. In this case, second-harmonic light generated deep in the medium is absorbed while propagating towards the surface. Hence, the effective depth probed by second-harmonic generation in reflection is the absorption depth at the second-harmonic wavelength. In Chapter 3, a reflection second-harmonic probe of GaAs is used to study the process of laser melting with femtosecond pulses. In this case, the absorption depth of the second-harmonic is 13 nm, which is much shorter than the 230-nm absorption depth of the fundamental. Hence, the second-harmonic probe is sensitive only to roughly the upper 13 nm.

The high intensities of short laser pulses are ideally suited for nonlinear probing. For an  $n$ th order process, the instantaneous signal intensity is proportional to  $I^n$ , where  $I = E/\tau$  is the probe intensity,  $E$  the pulse energy, and  $\tau$  the pulse duration. For a detector that integrates over the pulse duration, the detected signal is proportional to  $(E/\tau)^n \times \tau = E^n \tau^{1-n}$ . Thus, for a fixed pulse energy the detected signal increases as the pulse duration decreases for nonlinear processes ( $n > 1$ ).

### **1.1.4 Photoexcited Carriers**

An excitation beam incident in air on a semiconductor surface is reflected and absorbed according to the expressions (1.1), (1.6), and (1.7). From a microscopic

point of view, the dominant loss mechanism is the creation of an electron-hole pair by the absorption of a photon from the beam. In the absorption process, the electron acquires the energy and momentum of the photon. While the photon's energy is substantial, its momentum is negligible compared to the extent of the Brillouin zone. Equivalently, the wavelength of visible light lies in the range 0.4–0.7  $\mu\text{m}$  whereas wavelengths at the edge of the Brillouin zone are of the order of the interparticle spacing in the lattice, or about 0.2 nm. Since momentum is inversely proportional to wavelength, the photon momentum is less than one-thousandth the width of the Brillouin zone, and can therefore be neglected. The electron is said to make a vertical transition because the transition represented on an electronic band structure diagram of energy vs. wave vector is a vertical line.

The band structure of GaAs is shown in Fig. 1.2. Gallium arsenide is a direct gap material because the valence band maximum and the conduction band minimum occur at the same place in the Brillouin zone. The lowest energy vertical transitions are therefore in the  $\Gamma$  valley at the zone center. At room temperature, the absorption edge occurs at an energy of 1.42 eV ( $\lambda = 870$  nm). [Ridley 1988] Silicon, by contrast, is an indirect gap semiconductor. Although the top of the valence band is at the zone center, the minimum in the conduction band is near the edge of the Brillouin zone in the  $\langle 100 \rangle$  directions (near the X points). The onset of absorption corresponding to the indirect gap (1.12 eV in Si [Ashcroft 1976]) necessitates the participation of a high-momentum phonon (or crystal defect) in order to conserve crystal momentum.

In either direct or indirect gap semiconductors, the dominant absorption process when the photon energy exceeds the gap energy is single-photon absorption. The rate of generation of photoexcited electrons (and holes) per unit volume inside the surface is then simply the rate at which energy is absorbed from the light beam divided by the photon energy

$$N = \frac{I\alpha(1-R)}{h\nu} , \quad (1.10)$$

where  $I$  is the incident light intensity and  $h\nu$  is the photon energy. The factor  $(1-R)$  accounts for the fraction of incident intensity that is reflected at the interface. This expression assumes that the linear optical constants are not significantly modified by the radiation, which is the case for low-intensity experiments. At higher excitation levels, the linear optical constants  $\alpha$  and  $R$  may indeed be modified by the excitation. An accurate determination of the injected carrier density in such cases is difficult and depends on detailed knowledge of the time evolution of the

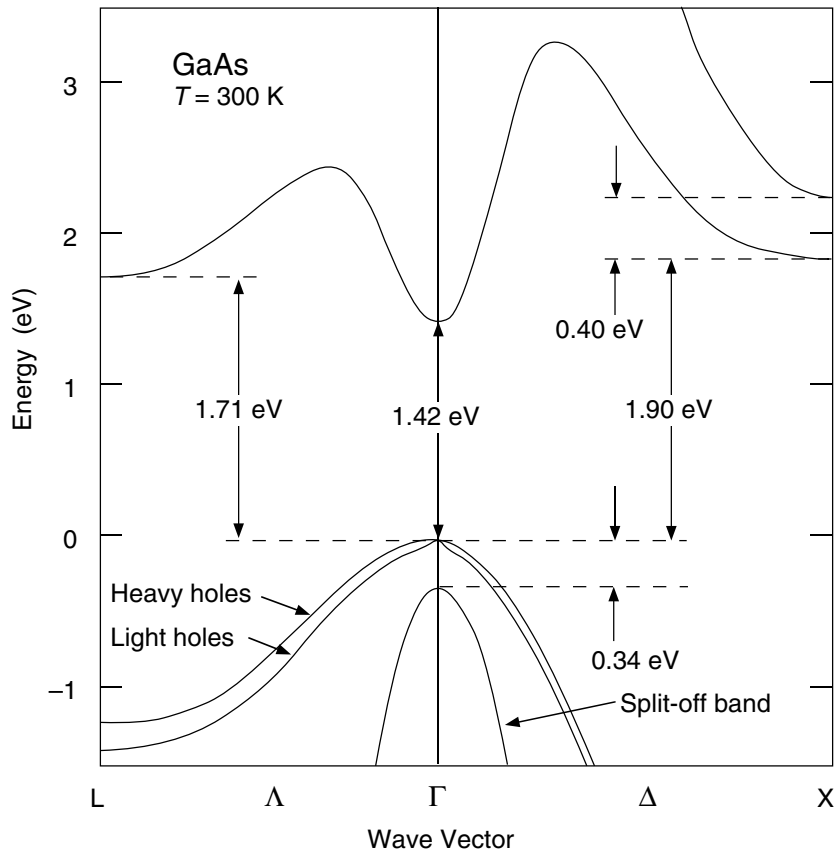


**Fig. 1.2** Electronic band structure of GaAs at room temperature, taken from Pierret 1987.

reflectivity and absorption constant  $\alpha$ .

### 1.1.5 Nonlinear Absorption

For photon energies below the gap and any excitonic resonances (bound electron-hole states [Ziman 1986, §6.7]), single-photon absorption is forbidden.<sup>1</sup> However, with high incident laser intensity higher-order absorption processes are possible. The lowest-order nonlinear process is two-photon absorption, in which the attenuation is proportional to the square of the laser intensity,

$$\frac{dI}{dz} = -\beta I^2 . \quad (1.11)$$

Two-photon absorption of 1.064- $\mu\text{m}$  (1.17-eV) radiation in several semiconductors has been studied using 30-ps pulses from a passively mode-locked Nd:YAG laser. [Bechtel 1976] For GaAs,  $\beta$  was measured to be 0.028 cm/MW, indicating that  $I$  must be at the terawatt/cm<sup>2</sup> level for absorption rates to approach above-gap linear absorption. Two-photon absorption can occur for incident photon energies above the gap, but it is dominated by linear absorption under normal circumstances. It may become significant in femtosecond excitation experiments when linear transitions are strongly bleached.

For strong enough field intensity, higher order nonlinear processes can compete with linear absorption and the whole basis of a perturbative treatment of the light-matter interaction breaks down. Roughly speaking, one expects this to occur when the electric field of the light pulse is comparable to the atomic fields. Bound

---

<sup>1</sup> Impurity levels in the gap give rise to some linear absorption at energies below the band gap. The density of carriers that can be excited in this manner depends, of course, on the purity of the sample. In any case, it is small compared to the density that can be excited with a photon energy appreciably above the gap energy.

field, leading to strong ionization of the outer electronic shells. The average field amplitude just inside the surface is given approximately by

$$\bar{E} \approx \sqrt{\frac{8\pi(1-R)F}{n_R c \tau}} \quad , \quad (1.12)$$

where  $\tau$  is the pulse duration and  $F$  is the incident energy per unit area, or fluence. From the ionization potential (a few eV) and the atomic dimension (roughly 1 Å), a field of a few tens of volts per nanometer should ionize the outer electrons directly. For a 100-fs pulse, Eq. (1.12) gives an incident fluence of order 4 J/cm<sup>2</sup> for direct ionization. Femtosecond pulses at fluences higher than this have been used to produce dense, hot plasmas in both metals and semiconductors up to plasma temperatures of a few hundred electron volts. [Murnane 1989]

Conduction electrons and valence holes can absorb a laser photon directly, absorbing or emitting a phonon to conserve momentum. [Seeger 1989] These free-carrier absorption processes provide an additional absorption mechanism in photo-excited semiconductors. Free-carrier absorption depends strongly on both density and wavelength. In general, it is significant only at high carrier densities for below-gap radiation where linear absorption is forbidden. It is also strong in molten semiconductors which have metallic conductivities.

## 1.2 Drude Model

A small density of thermally activated carriers is present in semiconductors at room temperature. In very pure silicon, for example, the density of conduction electrons (and holes) is roughly 10<sup>10</sup> cm<sup>-3</sup>. This is quite a small density; it leads to very low conductivity and has a negligible effect on the optical response away from the band edge. By comparison the free electron density in typical metals is in the range

$1-25 \times 10^{22} \text{ cm}^{-3}$ . [Ashcroft 1976] Photoexcitation of a semiconductor, however, can increase the carrier density by many orders of magnitude. The photoinjected free-carrier plasma can then have an important effect on the optical properties of the material.

A number of theoretical models have been proposed to describe the dynamics of carriers in semiconductors and their interaction with optical fields. The simplest is the Drude model which treats the carriers as a sea of free charged particles with a simple form of collisional damping. This model was originally put forth to account for the high conductivity of metals but has been successfully applied to photoexcited and molten semiconductors. [Liu 1983, Fauchet 1988]

An applied electric field  $\mathbf{E}$  causes free carriers of charge  $q$  and mass  $m$  in the material to accelerate under the applied force  $q\mathbf{E}$  with an acceleration  $\mathbf{a} = q\mathbf{E}/m$ . In the absence of momentum-changing collisions, the current density for an applied dc field, given by  $\mathbf{j} = q\mathbf{v}N$ , would increase linearly with time. In normal (not superconducting) metals and plasmas, however, the charge carriers suffer collisions with lattice defects, phonons, and other carriers that tend to randomize their velocities. In the Drude model, the effect of these collisions is described simply by a momentum relaxation time  $\tau$ , or equivalently by its inverse  $\gamma = \tau^{-1}$ , the scattering rate, which is independent of carrier energy and momentum. The velocity of a charged particle is then given by the equation

$$\frac{d\mathbf{v}(t)}{dt} = -\frac{\mathbf{v}(t)}{\tau} + \frac{q\mathbf{E}}{m}, \quad (1.13)$$

which yields an average drift velocity of  $\frac{q\tau\mathbf{E}}{m}$  and a dc conductivity of

$$\sigma = \frac{Ne^2\tau}{m} = \frac{Ne^2}{m\gamma}. \quad (1.14)$$

In this expression the unit electronic charge  $e$  is substituted for  $q$  because in semiconductor plasmas, both electrons and holes carry unit electronic charge.

If the applied electric field is time dependent, Eq. (1.13) can be Fourier transformed to yield the frequency-dependent conductivity [Jackson 1975]

$$\sigma(\omega) = \frac{Ne^2\tau}{m} \left( \frac{1}{1-i\omega\tau} \right) = \frac{Ne^2}{m} \left( \frac{1}{\gamma-i\omega} \right) . \quad (1.15)$$

This ac conductivity gives rise to a complex dielectric constant

$$\varepsilon(\omega) = 1 + \frac{4\pi\sigma i}{\omega} = 1 - \frac{4\pi Ne^2}{m} \left( \frac{1 - \frac{i\gamma}{\omega}}{\omega^2 + \gamma^2} \right) . \quad (1.16)$$

It is customary to rewrite this expression in terms of the plasma frequency, defined by

$$\omega_p \equiv \sqrt{\frac{4\pi Ne^2}{m}} . \quad (1.17)$$

Then the dielectric constant of the plasma can be expressed as

$$\varepsilon_{\text{plasma}}(\omega) = 1 - \frac{\omega_p^2}{\omega^2 + \gamma^2} \left( 1 - \frac{i\gamma}{\omega} \right) . \quad (1.18)$$

If there are also bound charges, their contribution must be added to (1.18). The full dielectric constant is then

$$\varepsilon(\omega) = 1 + 4\pi\chi_e - \frac{\omega_p^2}{\omega^2 + \gamma^2} \left( 1 - \frac{i\gamma}{\omega} \right) , \quad (1.19)$$

where  $\chi_e$  is the linear electric susceptibility of the bound charges. [Malvezzi 1986]

At low carrier density, the plasma frequency is well below optical frequencies. The primary effect of the plasma on the dielectric response of the medium is a reduction of the real part of  $\varepsilon$ , which also reduces  $n_R$ . Neglecting damping, when the plasma term just cancels the bound electron dielectric constant  $\varepsilon_b = 1 + 4\pi\chi_e$ , the refractive index becomes purely imaginary. By Eq. (1.8), the material totally reflects the incident light. For a free-electron gas and optical frequencies, this hap-

pens at an electron density of approximately  $3 \times 10^{21} \text{ cm}^{-3}$ . Roughly speaking, this explains the high reflectivity of good metallic conductors to light at visible and longer wavelengths. If damping is non-negligible, the index has both real and imaginary parts, the reflectivity is less than unity, and the light that penetrates the interface is strongly absorbed by the plasma. Such is the case in molten semiconductors, which typically have reflectivities around 70% in the visible.

In photoinduced semiconductor plasmas, both the electrons and the holes make a Drude-type contribution to the dielectric constant. Then the dielectric constant can be expressed as

$$\epsilon(\omega) = \epsilon_b - \sum_j \frac{4\pi N_j e^2}{m_j} \left( \frac{1 - \frac{i\gamma_j}{\omega}}{\omega^2 + \gamma_j^2} \right), \quad (1.20)$$

where the sum is over the different conduction band minima and valence band maxima, each characterized by a mass  $m_j$  and momentum scattering rate  $\gamma_j$ . In practice, a single effective mass and scattering rate are frequently used to describe the ensemble of hole bands and another effective mass and scattering rate are used for the electrons. [Malvezzi 1986]

Despite its simplicity, the Drude model satisfactorily accounts for the free-carrier contribution to the dielectric response in a number of semiconductors under conditions of carrier internal equilibrium. [Malvezzi 1986] It has been applied successfully to silicon both below the melting threshold [Shank 1983] and in the molten phase, where optical measurements at various wavelengths interpreted with the Drude model confirm the complete ionization of valence electrons. [Liu 1983] Optical measurements on laser-excited (molten) GaAs using 20-ps pulses at  $\lambda = 532 \text{ nm}$  [Liu 1986] and using 160-fs pulses at  $\lambda = 620 \text{ nm}$  described in Chapter 3 of this thesis, however, are inconsistent with a *fully-ionized* Drude model. It appears that roughly half of the valence electrons are ionized in the liquid phase.

## 1.3 Scattering Processes

A great many interactions affect the state of the electrons and holes following their initial excitation, including electron-electron, hole-hole, and electron-hole scattering; intervalley scattering; phonon emission; Auger recombination and impact ionization; screening; plasmon emission; defect scattering; diffusion; and radiative recombination. The scattering processes are depicted schematically in Fig. 1.3.

The rates of these processes have different dependence on temperature and

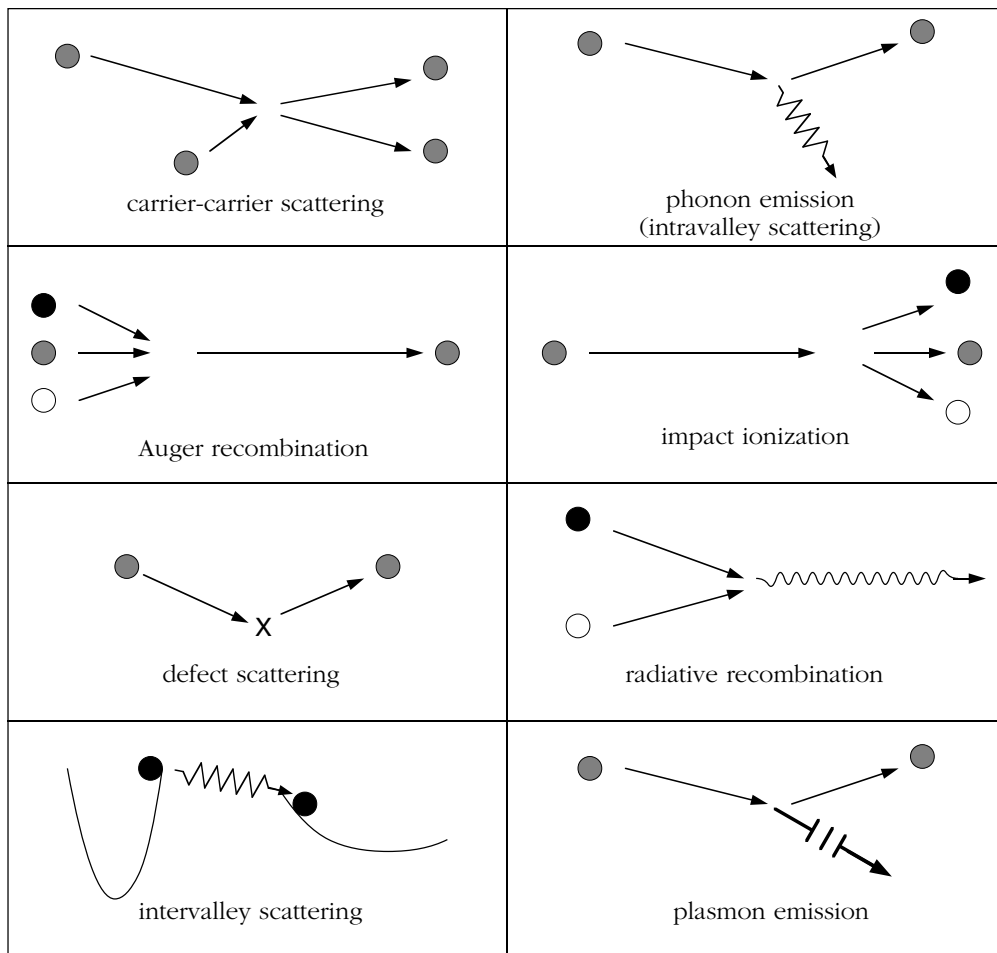


**Fig. 1.3** Schematic representation of carrier scattering processes in semiconductors.

carrier density. For example, the carrier-carrier collision time in GaAs depends inversely on the carrier density (in the absence of screening) and is given approximately by  $2 \times 10^4 N^{-1} \text{s cm}^{-3}$  [Conwell 1966]. The emission time of longitudinal optical phonons at these densities is independent of density, essentially independent of lattice temperature, and equal to  $\sim 200 \text{ fs}$ . [Kash 1988] A carrier density of  $10^{17} \text{ cm}^{-3}$ , therefore, marks a boundary between regimes in which carrier-carrier scattering or phonon emission is the dominant scattering process at short times. Figure 1.4 shows the approximate time scales for the various interaction processes at high density.

Many of the scattering rates are difficult to calculate accurately from known equilibrium properties of the semiconductor. High photoexcited carrier densities

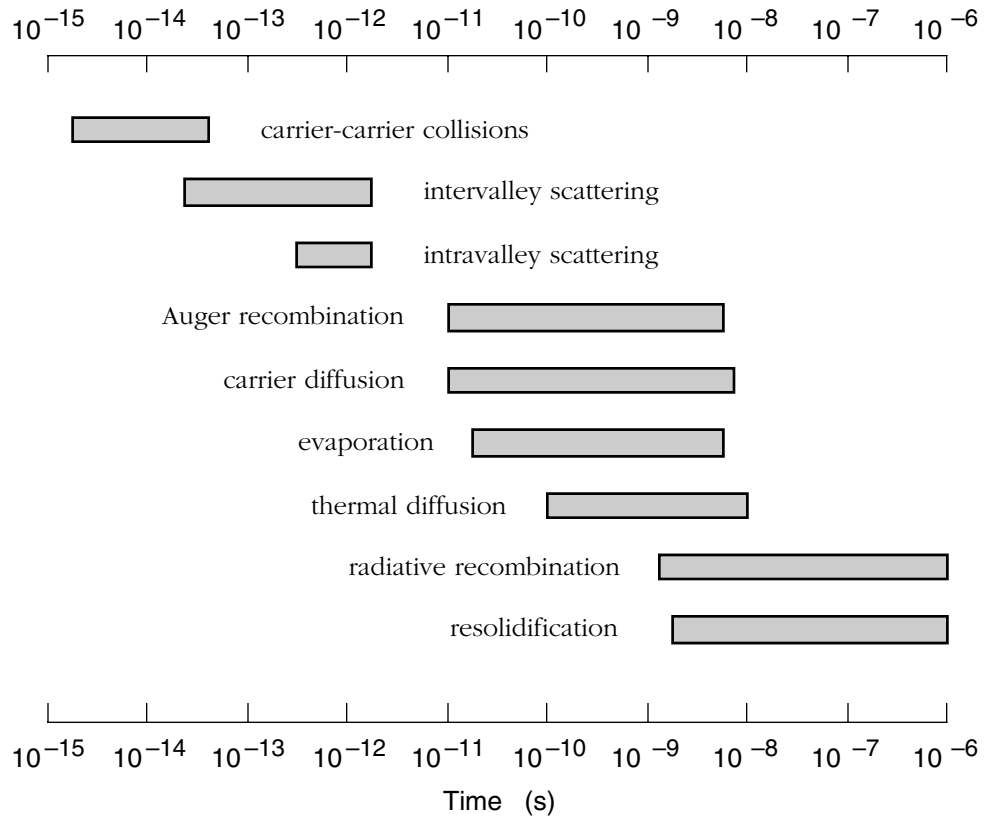


**Fig. 1.4** Approximate time scales for carrier interactions and thermal processes in GaAs. Many time scales depend on density and/or temperature; the figure assumes moderate to high photoexcited carrier density ( $N > 10^{18} \text{ cm}^{-3}$ ).

further complicate the calculations. Much of the understanding of scattering rates comes from time-resolved optical experiments. A brief examination of these mechanisms, with an emphasis on the relevant experiments and time scales in GaAs, is given in the following sections.

### **1.3.1 Carrier-Carrier Scattering in GaAs**

A number of experiments on bulk GaAs and on GaAs quantum wells indicate that for injected carrier densities above  $\sim 10^{17} \text{ cm}^{-3}$ , electrons and holes scatter out of their initially occupied states in less than 10 fs and achieve quasi-equilibrium within tens of femtoseconds. [Lin 1988, Knox 1988] Carrier-carrier collisions are largely responsible for this rapid thermalization, and insofar as this is the case, the energy content of the carrier system remains unchanged by the thermalization process. The high temperature of the hot carriers reflects the amount by which the photon energy exceeds the band gap. For instance, 2-eV photons inject electrons from the light and heavy hole bands into  $\Gamma$  states  $\sim 0.4$  eV above the conduction band minimum. A thermalized nondegenerate electron plasma at an average energy of 0.4 eV has a temperature of 4600 K. Thus, electron temperatures several thousands of degrees above the lattice temperature are easily obtained with visible femtosecond and picosecond excitation pulses.

Using transient absorption spectroscopy on a thin GaAs sample, Lin and coworkers observed a rapid partial recovery in absorption after excitation with pulses as short as 35 fs. [Lin 1988] For a pump and probe energy of 1.98 eV, at which transitions from the heavy-hole, light-hole, and split-off valence bands create electron distributions at approximately 500 meV and 150 meV above the conduction band minimum, the absorbance of the excited material initially decreases, then shows a two-component recovery. The initial bleach is attributed to state filling by

the excited electrons. The fast partial recovery has two components: carrier-carrier scattering and scattering to satellite valleys accompanied by phonon emission. For carrier densities of  $1 \times 10^{17}$ ,  $3 \times 10^{17}$ , and  $1 \times 10^{18} \text{ cm}^{-3}$  the fast component has exponential response times of 30, 17, and 13 fs, respectively. Although it is impossible to separate the fast scattering mechanisms in these experiments, [Lin 1988] the density dependence of the scattering time suggests that carrier-carrier collisions are an important scattering mechanism.

Further evidence of rapid carrier-carrier scattering was obtained with a femto-second continuum probe pulse. [Lin 1988] Transient absorption spectra display an extremely rapid broadening with respect to the spectrum of the pump pulse. In analogy with hole-burning in 2-level systems, the minimum spectral width of the hole is attributed to a homogeneous dephasing time  $T_2$ . [Oudar 1985] The authors conclude that within tens of femtoseconds, carriers scatter out of initially occupied states and begin to form a quasi-thermal distribution.

Using modulation-doped GaAs quantum wells, Knox and coworkers observed an enhanced thermalization rate for photoexcited electrons in the presence of a dense Fermi sea of electrons at room temperature, whereas no enhancement was detected for a similar dense Fermi sea of holes. [Knox 1988] In these experiments, the excitation pulse energy was only slightly above the band edge, eliminating absorption from the split-off valence band and scattering to satellite valleys. Using a relaxation-time approximation to model the data, the thermalization time for a density of  $2.5 \times 10^{17} \text{ cm}^{-3}$  of photoexcited electrons in the presence of an equal density of thermalized electrons was determined to be roughly 10 fs. No deviation from a Boltzmann distribution of carriers was detected using 100-fs pulses. For a thermalized sea of holes, and for the undoped sample, the thermalization time of 60 fs is significantly longer.

In the undoped sample, the density dependence of the thermalization time was

studied for the density range from  $1.7 \times 10^{16}$  to  $4 \times 10^{17} \text{ cm}^{-3}$ . The thermalization time was determined to depend approximately as  $N^{-1/4}$ , going from 100 fs to 30 fs over this range. At high density, screening and degeneracy decrease the intrinsic scattering rates, but collisions are more inelastic, resulting in shorter thermalization times. At low density, the intrinsic collision rate is faster, but the collisions are more elastic so that more scattering events are necessary before the carriers attain a quasi-thermal distribution. [Goodnick 1987]

### **1.3.2 Carrier-Phonon Scattering**

Whereas carrier-carrier scattering and Auger recombination, to be discussed below, preserve the energy of the carrier system, the emission of phonons by hot carriers transfers energy from the carriers to the lattice vibrations, cooling the carriers. The leading interaction between carriers and phonons depends on whether the material is polar. In polar semiconductors, the compressions and rarefactions of longitudinal optical (LO) phonons establish periodic electric fields in the direction of the phonon wave vector  $q$ . These couple strongly to charge carriers, giving rise to a scattering Hamiltonian, first derived by Fröhlich, [Fröhlich 1937] that is proportional to  $q^{-2}$ . In nonpolar semiconductors, the coupling is via the optical deformation potential, which is proportional to the magnitude of the displacement of atoms in the phonon mode. Optical deformation potential scattering is independent of phonon wave vector  $q$ . The deformation potential interaction also gives rise to scattering with acoustic phonons, although in general, since the energy of an acoustic phonon is very small, energy loss rates are significant only when scattering from optical phonons is energetically forbidden. [Yoffa 1981]

Several types of phonon scattering processes are possible, some of which are indicated schematically in Fig. 1.5. In indirect gap semiconductors such as silicon,

the absorption of a photon by a valence electron requires the absorption or emission of an optical phonon to conserve momentum. Compared to the photon energy ( $\sim 2.3$  eV), the phonon energy ( $\sim 0.060$  eV) is quite small; the electron carries away the majority of the excitation energy. In both polar and nonpolar semiconductors, the excess kinetic energy of photoexcited electrons relaxes to the lattice by the emission of  $\sim 10$ – $15$  optical phonons on a time scale of 2–4 ps. Kash, Tsang, and Hvam used spontaneous Raman scattering on GaAs to measure the rate of (low-momentum) LO-phonon emission from electrons cascading down the sides of the  $\Gamma$  valley after excitation with 588-nm pulses. [Kash 1985] Below a density of  $2 \times 10^{17}$   $\text{cm}^{-3}$ , they claim an average emission time of 165 fs. Further experimental

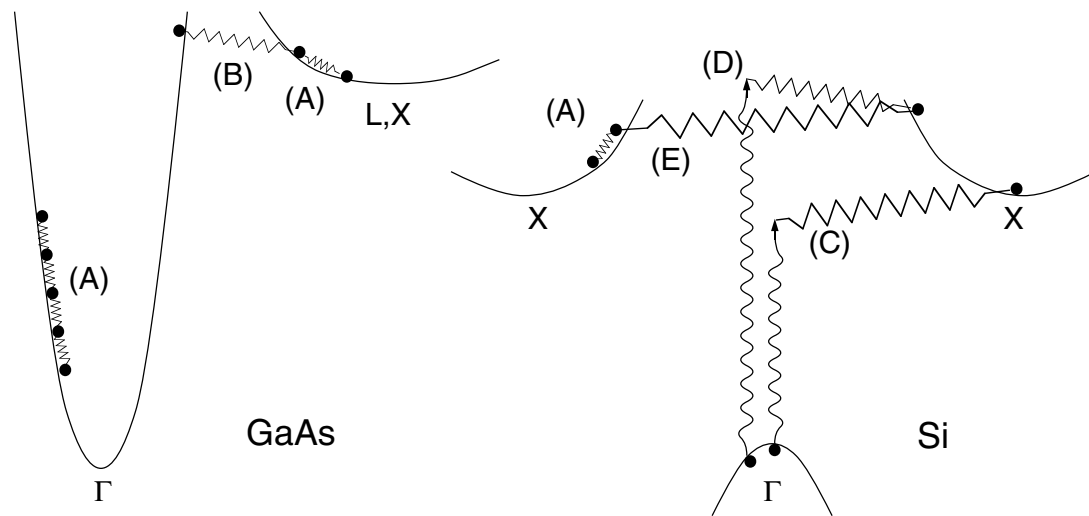


**Fig. 1.5** Schematic representation of scattering processes between electrons and optical phonons: (A) intravalley scattering by optical phonon emission, (B) scattering to high-momentum satellite valleys with high momentum LO and TO phonons, (C) electron-hole pair creation accompanied by the absorption of an optical phonon, (D) electron-hole pair creation with phonon emission, and (E) intervalley scattering between equivalent high-momentum valleys.

work by the same authors, as well as a theoretical calculation based on the frequency splitting between LO and TO phonons at the zone center, put the low density scattering time at 200 fs. [Kash 1991]

The coupling between optical phonons and holes leads to rapid equilibration of holes at the lattice temperature. Shah and coworkers have observed energy loss rates for holes up to 25 times those for electrons in GaAs quantum wells. [Shah 1985] In many circumstances, photoexcited electrons equilibrate at a temperature significantly above the temperature of the holes. [Shah 1985, Höpfel 1986] This comes about not only because of the faster loss rate to phonons, but also because the lighter electrons carry away the majority of excess kinetic energy at excitation.

At higher energies in GaAs, when scattering into the satellite L and X valleys is energetically allowed, these processes rapidly remove electrons from the  $\Gamma$  valley, contributing to the very rapid dephasing time of photoinjected electrons. The  $\Gamma \rightarrow L$  and  $\Gamma \rightarrow X$  scattering rates are high because of the high density of final states in the high-mass satellite valleys. Shah *et al.* have observed a 100-fs  $\Gamma \rightarrow L$  scattering time using 0.5-ps pump pulses at 2.04 eV, and a subsequent 2-ps  $L \rightarrow \Gamma$  return time. [Shah 1987] Using 6-fs pulses centered at 2.0 eV, Becker *et al.* measured a scattering time of 33 fs at room temperature when both the L and X valleys are accessible, and 80 fs at 35 K when electrons could scatter only to the L valleys. [Becker 1988] The 6-fs pulses had considerable spectral bandwidth, covering the range from 1.85–2.15 eV. As noted by the authors, the initial carrier distribution injected with such pulses differs significantly from the distribution obtained with spectrally narrow pulses. Transform-limited pulses of 100-fs duration, for instance, have a bandwidth of  $\sim 3$  meV. The greater spectral width of the injected carriers most likely decreases degeneracy effects resulting in more efficient scattering.

Intervalley scattering is less affected by screening effects than intravalley scattering because of the large momenta involved. [Yoffa 1981] In Si, intervalley scattering

among the equivalent X valleys is always energetically allowed, resulting in efficient energy transfer from carriers to phonons.

### 1.3.3 Carrier Recombination

Photoinjected electrons and holes eventually recombine in pairs and annihilate each other. In the process, the electron energy is transferred to a photon, to another charge carrier, or to phonons. Radiative recombination rates in GaAs for thermal electrons and holes at the band edge are on the order of 1 nanosecond. [Hwang 1973] In silicon, radiative recombination (like photoexcitation) requires the participation of a momentum-conserving phonon. Consequently, luminescence is weak and nonradiative recombination at defects and impurities competes with radiative recombination. For the high carrier densities of laser melting experiments, Auger recombination is the dominant recombination mechanism.

In an Auger process, the energy of a recombining electron-hole pair is given to a third charged particle, either an electron or a hole (see Fig. 1.3). Auger recombination decreases the density of the carriers while increasing their average energy. It therefore acts effectively as a heat source for the charge carriers. [van Driel 1987] At low densities, the Auger recombination rate is proportional to the cube of the electron (hole) density  $N$ ,

$$\frac{dN}{dt} = -\gamma N^3, \quad (1.21)$$

where  $\gamma$  is the Auger coefficient. In silicon,  $\gamma = 3.8 \times 10^{-31} \text{ cm}^6 \text{ s}^{-1}$ . [Shank 1983] To estimate the effective Auger recombination time, Eq. (1.21) can be integrated for a given initial electron density  $N_0$  to give

$$N(t) = \frac{N_0}{\sqrt{1 + \gamma N_0^2 t}}. \quad (1.22)$$

This expression gives the carrier density after a delta-function excitation in the absence of diffusion. Taking as the effective recombination time  $\tau_{\text{Auger}}$  the interval over which the carrier density is reduced to half its starting value, we have

$$\tau_{\text{Auger}} = \frac{1}{\gamma N_0^2} . \quad (1.23)$$

For an injected density of  $4 \times 10^{20} \text{ cm}^{-3}$  in silicon, this expression gives an Auger time of 16 ps. For excitation with nanosecond and intense picosecond pulses, therefore, Auger recombination plays an important role in limiting the photoexcited carrier density.

With femtosecond excitation, however, Auger recombination is unable to limit the carrier density. Furthermore, the cubic dependence on carrier density is modified by screening, leading to a saturation at the high density value of  $\sim 6$  ps. [Haug 1978, Yoffa 1980] Evidence of this saturation was obtained by Shank, Yen, and Hirlmann using intense 90-fs excitation pulses. [Shank 1983] They observed the reflectivity of highly-excited silicon to recover on a time scale consistent with a carrier density decrease resulting from diffusion, not Auger recombination.

The inverse of Auger recombination is called impact ionization, in which an energetic electron collides with a valence electron, causing it to make a transition to the conduction band (see Fig. 1.3). Because the “reactant” in this process is a single particle, impact ionization scales linearly with carrier density. [van Driel 1987] For spherical parabolic bands in a direct gap semiconductor, the energy threshold for impact ionization is given by [Ridley 1988]

$$E_{\text{th}} = \left( \frac{1 + 2\mu}{1 + \mu} \right) E_g , \quad (1.24)$$

where  $\mu = m_c/m_v$  is the ratio of the effective masses of the conduction and valence bands. In GaAs, this gives a threshold of 1.6 eV above the conduction band minimum. Roughly speaking, this corresponds to a plasma temperature of  $2 \times 10^4 \text{ K}$ .

For temperatures significantly below this, as is the case in the experiments described in this thesis, impact ionization is negligible.

### 1.3.4 High Density Effects

When the density of photoexcited carriers grows large, degeneracy and screening effects can significantly modify scattering rates. In a degenerate carrier gas, scattering rates are lowered by the reduction in the density of available final states. In GaAs at room temperature, the onset of degeneracy occurs at an electron density of about  $5 \times 10^{17} \text{ cm}^{-3}$  (or a hole density of  $10^{19} \text{ cm}^{-3}$  in the case of *p*-doped material). [Wight 1985] At the elevated carrier temperatures of laser-excited plasmas, the degeneracy densities are somewhat higher. For a scattering process with a nondegenerate scattering rate  $W_o$ , degeneracy reduces the rate to

$$W = W_o(1-f_i)(1-f_f) \quad , \quad (1.25)$$

where  $f_f$  is the fraction of final states that are occupied and  $f_i$  the fraction of initial states that are *unoccupied*. In the case of weak degeneracy, this is often simplified to

$$W = W_o(1-f_i-f_f) \quad . \quad (1.26)$$

The bleaching of near-band-edge absorption in a direct gap semiconductor quantum well has been attributed principally to Pauli exclusion (degeneracy or “phase-space filling”), as opposed to Coulomb screening. [Knox 1986]

Screening of the bare carrier charge and of the charge density waves in longitudinal phonons of polar semiconductors by the electron-hole plasma also reduces carrier interaction rates, particularly at long wavelengths. Simple Coulomb screening [Ashcroft 1976] reduces the Coulomb potential  $V = q/r$  to  $V = qe^{-k_0 r} r^{-1}$ , where  $k_0^{-1}$  is the density-dependent Thomas-Fermi screening length. For wavelengths long compared to this screening length, static screening strongly reduces the interaction

potential. Haug [Haug 1978] has calculated that screening modifies the Auger recombination rate according to

$$\left(\frac{\partial N_e}{\partial t}\right)_{\text{Auger}} = \frac{-\gamma N_e^3}{[1 + (k_0/k_G)^2]^2} \quad , \quad (1.27)$$

where  $k_G = \frac{2\pi}{\hbar} \sqrt{2m_e^* E_G}$  is the wave vector corresponding to the energy gap  $E_G$ . Strong screening of Auger recombination in silicon was observed by Shank, Yen, and Hirlimann using femtosecond excitation pulses. [Shank 1983]

Yoffa has pointed out that the  $q^{-2}$  Fröhlich interaction in polar semiconductors is particularly susceptible to screening, which reduces the energy loss rate of electrons in the  $\Gamma$  valley to LO phonons in GaAs. [Yoffa 1981] She predicts that phonon emission rates begin to decrease at  $N \approx 6 \times 10^{16} \text{ cm}^{-3}$ , although experimental evidence [Kash 1985] suggests that the density has to be perhaps an order of magnitude higher before screening becomes significant. The carrier cooling rate is also reduced by a high density of non-thermal LO phonons (the hot phonon effect), [Shah 1985] as the carriers begin to gain appreciable energy by phonon absorption. In contrast to LO phonon emission by intravalley scattering, intervalley scattering is not particularly susceptible to screening, due to the large phonon wave vectors involved.

As the plasma density increases, eventually the plasma frequency comes into resonance with the band gap. It has been predicted [Rasolt 1985, Rasolt 1987] that at this resonance the carrier recombination rate is greatly increased by a plasmon-emission recombination channel. In silicon, the indirect nature of the gap requires the participation of a high-momentum phonon in a plasmon-assisted recombination process. Plasmon-phonon-assisted recombination (PPAR) has been invoked to explain anomalously high recombination rates in a picosecond experiment on silicon. [Malvezzi 1986] However, a density- and temperature-dependent reduction in

the diffusion coefficient can also explain the data. [van Driel 1987]

## **1.4 Laser Annealing**

Two of the experiments of this thesis, discussed in Chapters 3 and 5, concern the carrier dynamics in semiconductors excited by intense short laser pulses. This topic has been of considerable interest since it was first observed in the 1970s that damage to the crystalline lattice introduced by ion bombardment during doping could be removed by exposure to intense laser radiation. [von der Linde 1990] A dispute as to the underlying mechanism of the “laser annealing” process ensued. Most workers supported a thermal model which assumes that the absorbed light energy is converted essentially instantaneously into heat. If enough heat is absorbed for the damaged surface layer to melt, one might expect epitaxial regrowth to take place on the undamaged bulk substrate. A contrary thesis was advanced by J. A. Van Vechten. [Van Vechten 1979a, Van Vechten 1979b, Van Vechten 1981] In his “plasma annealing” picture, the dense electron-hole plasma created by photoexcitation plays a dominant role in increasing atomic and defect mobility in the excited semiconductor. By relaxing the interatomic bonds, the plasma enables defects to diffuse to the surface before significant energy is relaxed to lattice vibrational modes.

The basic physics of laser annealing is discussed in a number of review articles. [Brown 1980, Wood 1981, Brown 1984, Bloembergen 1986, von der Linde 1990] In view of pulsed-laser experiments performed in the last decade, it is clear that phonon emission efficiently couples hot carriers to optical phonon modes. Redistribution of the vibrational energy throughout the phonon spectrum arises from anharmonicities in the phonon potential, although the time scale for this thermalization can depend strongly on phonon energy. Experiments performed with pulses longer

than the carrier-phonon coupling time of a few picoseconds can be satisfactorily analyzed in the framework of the thermal model.

Melting is observed to take place during pulses of 20-ps duration and longer, as judged by a sharp rise in reflectivity. A liquid layer forms at the surface and propagates into the bulk of the material at a rate that approaches the speed of sound in the crystal. [Spaepen 1986] Until the molten layer is thick enough to absorb the transmitted probe light, the reflectivity of the excited material is determined by the interference of the waves reflected at the air-liquid and liquid-solid interfaces. [Born 1980] Heat from the high-conductivity molten region at the surface diffuses into the bulk substrate. Because the laser spot size is much larger than the absorption depth of the irradiation, the heat conduction can be treated as a one-dimensional flow problem along the normal. The thermal diffusion time can be estimated from the (temperature-dependent) diffusivity  $D = \kappa/c$ , where  $\kappa$  is the thermal conductivity and  $c$  is the specific heat. Ignoring the temperature dependence, the characteristic diffusion time is related to the length scale of the temperature variation by

$$t_D \sim \frac{l_D^2}{4D} . \quad (1.28)$$

This leads to resolidification on nanosecond time scales. [Spaepen 1986] With very large temperature gradients in the material at the solid-liquid interface and large resolidification interface velocities, an amorphous layer can result. This has been observed in both semiconductors and metallic glasses.

Tens of picoseconds after excitation the reflectivity of semiconductor samples has been observed to drop significantly below the high value of the metallic liquid phase. [Downer 1985, Liu 1986] The origin of this reflectivity drop has inspired some controversy. Bloembergen [Bloembergen 1986] and others have pointed out that negligible evaporation of atoms from the surface can take place during picosecond excitation pulses. In essence, the atoms do not have enough time to expand into a

high-temperature gas phase in front of the surface. On the other hand, Downer *et al.* [Downer 1985] have attributed the reflectivity drop to absorption and scattering by a cloud of silicon droplets in front of the surface. Our work on laser-excited GaAs, presented in Chapter 3, indicates that sufficient material is ejected from the surface to account for the observed decrease in reflectivity and to produce scattering of probe light away from the specular direction. Furthermore, it is likely that strong body forces in the highly-excited material lead to a shock wave that ejects material much more efficiently than does evaporation.

The invention of femtosecond dye lasers and high-energy amplifiers in the early 1980s opened the possibility to probe the breakdown of the thermal model. An intense femtosecond pulse can deliver its energy to the electronic system before appreciable energy has time to relax to the lattice vibrational modes. The system of a hot plasma and cold lattice present immediately following excitation bears some resemblance to Van Vechten's plasma annealing picture of laser annealing. Our experiments suggest that the high level of electronic excitation severs the interatomic bonds, enabling the ions of the lattice to disorder rapidly even before they acquire appreciable energy from the carrier system.

## **1.5 Overview of This Thesis**

Having introduced in this first chapter the principal physical processes and time scales governing the ultrafast dynamics of photoexcited carriers in semiconductors, the remainder of this thesis describes three excite-and-probe experiments on semiconductor surfaces and on GaAs/AlAs multiple quantum well structures. The amplified femtosecond dye laser system we have constructed in order to perform carrier and phonon dynamics measurements with improved temporal resolution is described in Chapter 2. The oscillator is a colliding-pulse mode-locked dye laser

producing a 125-MHz train of 70–900-fs pulses at 620 nm. These are amplified at a 10-Hz repetition rate in a 5-stage dye amplifier to yield 160-fs pulses with an average energy of 0.5 mJ. The amplifier employs prism dye cells and relay imaging to produce pulses with a smooth spatial profile that can be focused nearly to the diffraction limit.

The application of these amplified pulses to a laser melting study of GaAs is presented in Chapter 3. Reflection second-harmonic generation and linear reflectivity are used to study the transformation of the electronic state of roughly the upper one hundred atomic layers. On a time scale of 100 fs the second-harmonic signal is observed to vanish, indicating a transformation to a centrosymmetric state. Within half a picosecond, the reflectivity rises to a steady high value characteristic of a metallic molten phase. These response times are slightly faster than those observed on silicon.

Several picoseconds following excitation, the reflectivity is observed to drop. The origins of this drop have been investigated with time-resolved scattering experiments, as well as with mechanical probes and electron micrographs of the damaged region of the surface following excitation. These indicate that roughly 90 nm of material is ejected from the surface following excitation, some of which appears to fall back to the surface and resolidify in the form of droplets of 100–200-nm diameter. If this material were to be ejected rapidly enough from the surface in the form of droplets of appreciable size, both the observed rise in scattering and drop in reflectivity can be accounted for.

Chapter 4 is devoted to a study of ultrafast interlayer transport of photoexcited electrons in staggered type II multiple quantum well structures. Most work on GaAs/(Ga)AlAs quantum wells prior to this study concentrated on type I wells, in which photoexcited electrons and holes remain in the GaAs well layers. This research demonstrates that electrons created in the GaAs layers scatter on a subpi-

cosecond time scale to adjacent ALAs layers in type II structures. The fast scattering leads to a rapid partial recovery in the transient absorption spectrum, which remains partially bleached at the band edge due to the presence of holes in the GaAs layers.

In Chapter 5 an experiment on the picosecond laser melting of silicon is described. The experiment uses reflectivity near the Brewster angle and a streak camera to record the melting dynamics with spatial resolution across the excited surface region and a temporal resolution of 1.8 ps. The streak camera images show the expected reflectivity rise when the surface melts and illustrate the importance of spatial resolution in near-threshold experiments.

A computer model of the thermal and carrier-density dynamics in highly excited silicon is described in an appendix. Application of the model to the case of intense picosecond laser pulses indicates that the surface can be heated considerably above the melting temperature, and even strongly superheated above the vaporization temperature. The thesis concludes with some remarks about possible future experiments.

## Chapter 2

# Amplified Femtosecond Dye Laser

Time-resolved optical studies of the carrier dynamics of highly excited materials require short high-energy pulses of smooth, well-characterized spatial profile. Early investigations were conducted with amplified ruby and Nd:YAG lasers producing infrared and visible pulses with nanosecond duration. Passive mode-locking by incorporation of a saturable absorber dye in the cavity coupled with  $Q$ -switching or active mode-locking brought the pulse duration down to the picosecond regime. Since 1980, a number of designs have been developed to generate intense pulses in the femtosecond regime. One must choose among the various designs to satisfy the pulse requirements of the intended experiment. For the laser melting experiments on GaAs discussed in the following chapter, pulses of roughly 100-fs duration with energies at the millijoule level are required to supply the necessary energy in a time short compared to the carrier-lattice coupling time and to time-resolve the transformation. These criteria are met by the amplified colliding-pulse mode-locked (CPM) dye laser we have constructed at Harvard.<sup>1</sup>

The femtosecond dye laser system is shown schematically in Fig. 2.1. The CPM

oscillator is a seven-mirror ring cavity with two dye jets, one to provide gain, the other to mode-lock the cavity. In addition, four quartz prisms in a symmetric configuration provide tunable negative group velocity dispersion inside the cavity to compensate the normal dispersion of the two jets. The oscillator produces two 125-MHz beams of femtosecond pulses with an average power of 5 mW in the red (near  $\lambda =$

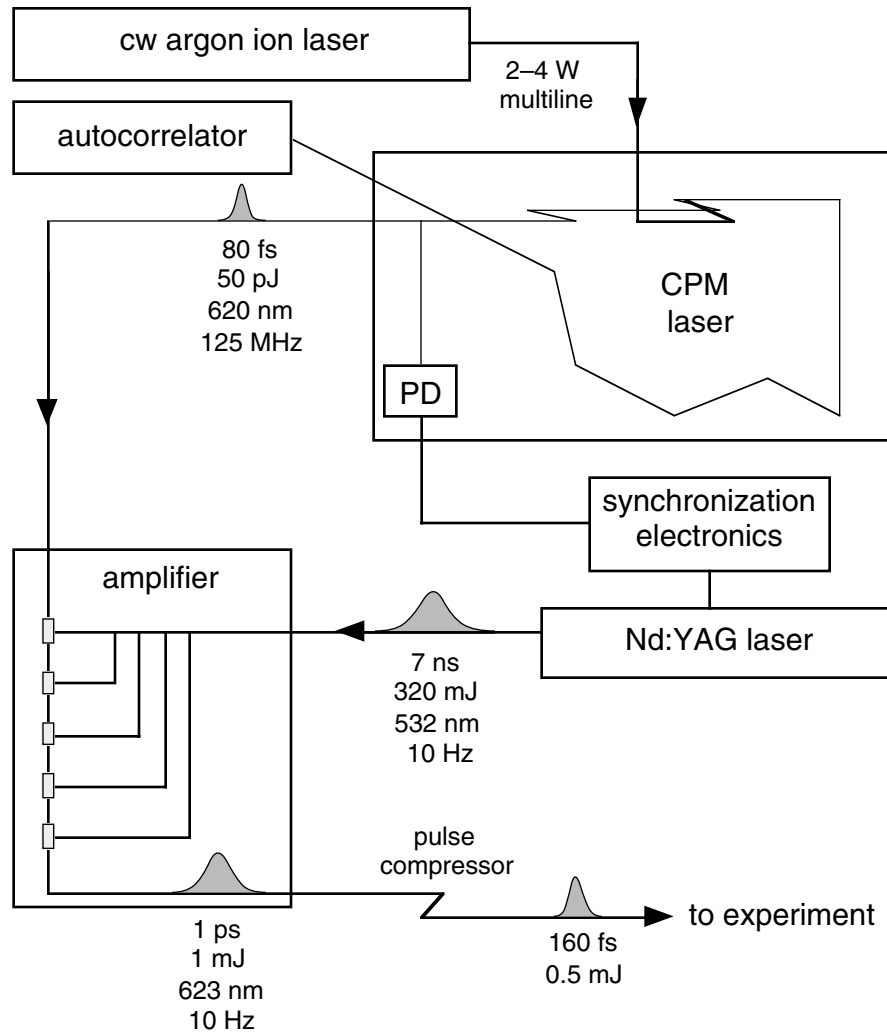


**Fig. 2.1** Schematic representation of the laser system illustrating the generation of 160-fs (FWHM) pulses at millijoule energies.

<sup>1</sup> The CPM oscillator and 10-Hz transverse-pumped dye amplifier were constructed by Juen-Kai Wang, Maarten Buijs, and Peter Saeta.

620 nm) that can be tuned in the range 70–900 fs. One beam is used for pulse diagnostics; the other seeds a five-stage dye amplifier transverse-pumped at a repetition rate of 10 Hz by a frequency-doubled Nd:YAG laser. Saturable absorber jets block the unamplified CPM pulses and suppress amplified spontaneous emission from the dye cells. Relay imaging and low-aberration optics are used to minimize diffraction distortion of the beam, yielding pulses with a “top hat” profile and an average energy of 1 mJ. These are compressed with either a prism pair or grating pair to give pulses of 160-fs duration (full width at half maximum) centered at  $\lambda = 623$  nm. The amplified beam is divided into pump and probe beams, which either are used as is or are frequency shifted by continuum generation, followed by frequency-selective optics, amplification, and compression.

In this chapter the oscillator and amplifier are described in detail. Initial alignment and daily operating procedures are summarized. Simple background-free intensity autocorrelation of pulses is discussed and an expression is derived to account for the temporal broadening of the autocorrelation signal caused by a large angle between the beams.

## 2.1 CPM Oscillator

The femtosecond CPM dye laser was designed and demonstrated by Fork, Greene, and Shank in 1981. [Fork 1981] In contrast to the linear cavities of actively and passively mode-locked YAG lasers, the standard CPM cavity is a “ring” (actually a modified triangle) with counter-propagating beams. Mode-locking is accomplished in a thin jet of the saturable absorber 3,3'-diethyloxadicyanine iodide (DODCI) dissolved in ethylene glycol. Losses in the absorber jet are minimized for counter-propagating pulses that collide in the jet, effectively bleaching the absorption for one another. Although it is possible to achieve colliding pulse mode-locking

in a linear cavity, the position of the jet must be very carefully controlled with respect to an end mirror to ensure that two pulses arrive simultaneously in the jet. In a ring cavity, on the other hand, the timing between the two counter-propagating pulses is established automatically by the colliding-pulse mechanism in the absorber jet. For most effective mode-locking, the two pulses should have equal energy. Hence, they should arrive at equal time intervals at the gain jet. This can be accomplished by separating the jets by one-quarter of the cavity optical path length.

The original CPM oscillator produced 100-fs pulses in stable trains with an average power of 50 mW. In this laser the pulse duration is limited by the normal group velocity dispersion of the dye jets, in which short-wavelength components of the pulse travel more slowly than longer-wavelength components. It was known that a pair of matched gratings could provide negative group velocity dispersion, [Treacy 1969] but gratings are too lossy to place in the oscillator cavity. In 1984 Gordon and Fork showed that a pair of prisms when suitably arranged could also provide negative group velocity dispersion. [Fork 1984, Gordon 1984] Furthermore, for prism faces cut at Brewster's angle the reflection loss can in principle be made to vanish, so that the introduction of prisms into the cavity has at most a slight impact on the lasing threshold. To facilitate alignment, and to avoid the spatial segregation of the various frequencies in the pulse, the standard CPM configuration includes not two but four Brewster-angle prisms in the symmetric arrangement indicated in Fig. 2.2.

### **2.1.1 CPM Laser Components**

All components of the CPM dye laser are mounted on a standard 2' × 4' optical breadboard (Newport Corporation) with two 4"-diameter holes drilled through to accommodate the two dye jets. A plexiglass case encloses the breadboard and optics to reduce air currents and improve the long-term stability of the laser. The

layout of the optical components is indicated in Fig. 2.2.

The gain jet (rhodamine 6G  $1 \times 10^{-3}$  M in ethylene glycol) is pumped by the output of a cw argon ion laser (Coherent Innova 200-10) operating in multiline mode that is focused by a spherical dielectric mirror with 15-cm radius of curvature. The plane of the jet is angled with respect to the  $p$ -polarized pump beam to reduce reflection loss at the jet surface. The nozzle is a standard 200- $\mu\text{m}$  dye laser nozzle (Coherent).

Typical operating pump powers in multiline mode lie in the range 2–4 W, depending on the age of the rhodamine solution, the degradation of the saturable absorber, and the accumulation of dust and condensed ethylene glycol on the

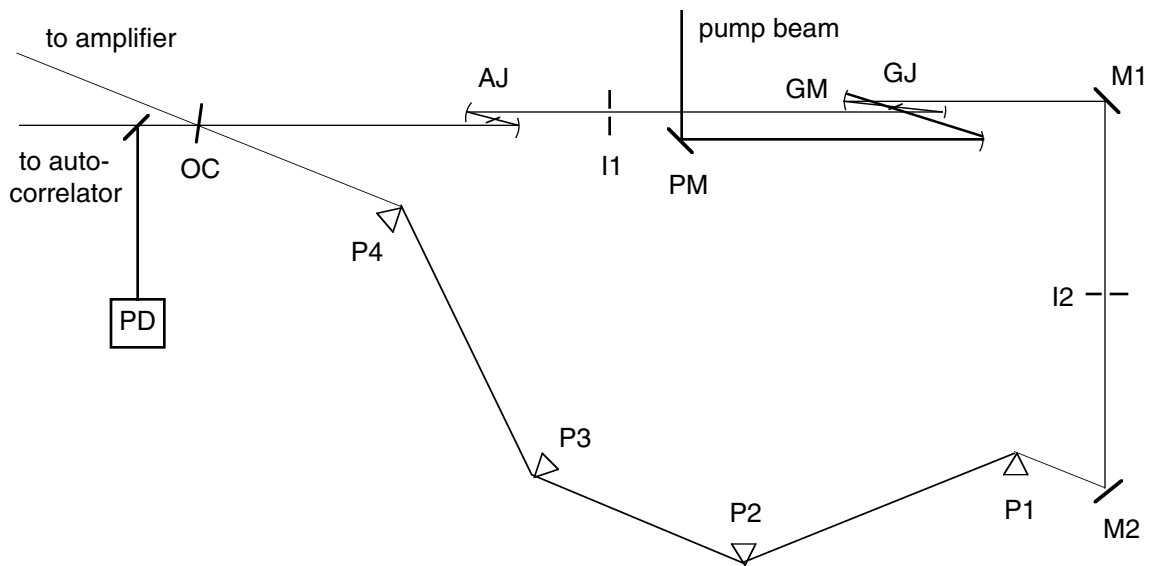


**Fig. 2.2** Layout of the CPM laser oscillator. The argon pump beam is directed by power mirror PM off a curved mirror into the rhodamine 6G gain jet GJ. A pair of curved mirrors recollimate the fluorescence and direct it towards mirror M1 to the right and the absorber “zee” to the left, where it is focused into the saturable absorber jet AJ and recollimated. Four prisms P1-P4 in a symmetric arrangement provide negative group velocity dispersion to compensate the positive dispersion of the dye jets. Two beams emerge from the output coupler OC, one of which seeds the amplifier, and the other is used for pulse diagnostics.

optics. Rhodamine is one of the more stable laser dyes, but it does suffer some oxidation or photochemical degradation over time and must be replaced roughly every 6 months.

It is also possible to pump with the 514.5-nm green line of the argon laser. As this is close to the peak in the absorption curve of rhodamine, the required pump power is reduced somewhat with respect to multiline pumping. We have found, however, slightly more stable operation in multiline mode. Some researchers have observed a high-frequency perturbation in the output of the CPM laser when pumped in single-line mode that corresponds to the beat frequency between adjacent longitudinal modes of the argon laser. The insertion of an etalon inside the argon laser cavity to constrain the output to a single longitudinal mode evidently removes this high frequency noise. Multiline pumping may also significantly reduce the mode beating.

A theory of colliding pulse mode-locking has been advanced that suggests that efficient mode-locking occurs only in a jet of roughly the same thickness as the optical pulses. [Kühlke 1983, Valdmanis 1986] Absorption loss in the jet is minimized for colliding pulses which establish an intensity grating or standing wave pattern in the jet. At the nodes of this pattern, the light intensity, and hence the absorption, vanishes. Furthermore, at the peaks absorption saturation occurs more readily than at the lower intensity of a single beam. Diffraction of light from one beam to the other by the index grating also appears to play a role in the CPM mechanism. [Kühlke 1983] Since a 70-fs pulse is only about 20  $\mu\text{m}$  thick in air, efficient colliding pulse mode-locking requires an absorber jet of approximately this thickness.

The mode-locking jet uses the saturable absorber dye DODCI ( $10^{-4}$  M) dissolved in ethylene glycol. DODCI is not nearly as robust as rhodamine and must be replaced roughly once a month. As the absorber solution degrades, the stability of the laser decreases until it fails to mode-lock entirely. Moisture in the dye solution

appears to accelerate the degradation of the dye and should be excluded as much as possible. To prolong the life of the DODCI solution, the dye reservoir should be covered, and if available, a positive pressure of *dry* nitrogen should be bubbled through the reservoir and inside the plexiglass enclosure.

The jet issues from a specially squeezed nozzle (Coherent) to reduce the thickness of the dye stream to about  $30\ \mu\text{m}$ . Squeezing the nozzle successfully requires practice and luck. The technique we have employed involves inserting a piece of trimmed 0.005" shim stock into the end of the nozzle. It is important to deburr and clean the trimmed stock before inserting it into the nozzle to keep the nozzle surface smooth. Heating the nozzle before squeezing with flat-jawed pliers seems to help. Once the nozzle has been squeezed and the shim removed, it can be tested by connecting it to the dye pump and flowing ethylene glycol at about 30 p.s.i. The center of the jet should be flat and the flow steady. The thickness of the jet can be estimated by preparing a dye solution of known absorptivity and measuring the attenuation of a He-Ne laser beam.

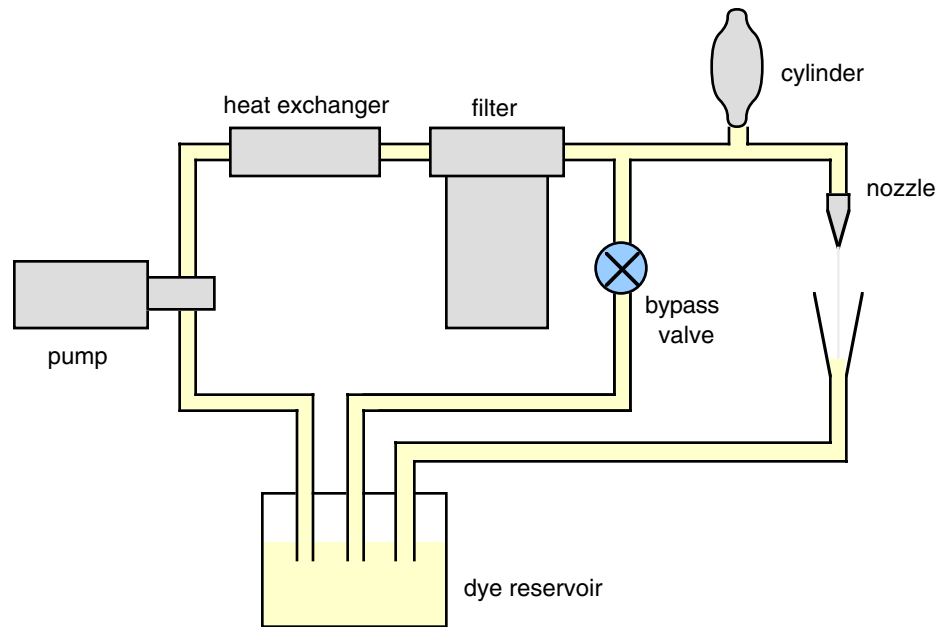


**Fig. 2.3** Dye circulation system for CPM jets.

The dye solutions are circulated by a pump (Micropump) connected in series with a 1- $\mu\text{m}$  particle filter (Cole-Parmer) and a small heat exchanger cooled with a modest flow of chilled water (see Fig. 2.3). A bypass valve that shunts dye solution back to the reservoir after the filter allows the nozzle pressure to be adjusted. Both jets are typically operated at 30 p.s.i. To reduce pressure fluctuations, a tee is inserted in the line before the nozzle and a cylinder (Hoke Industries) that is closed at the top is connected to the tee. The air trapped inside the cylinder functions analogously to a smoothing capacitance on the dye line.

Surrounding the gain jet is a pair of spherical mirrors with 10-cm radius of curvature (5-cm focal length). The mirrors are coated with a single-stack dielectric coating optimized for 632.8 nm (Virgo Optics). Single-stack coatings are used both in the oscillator<sup>1</sup> and in the subsequent handling of femtosecond pulses in order to

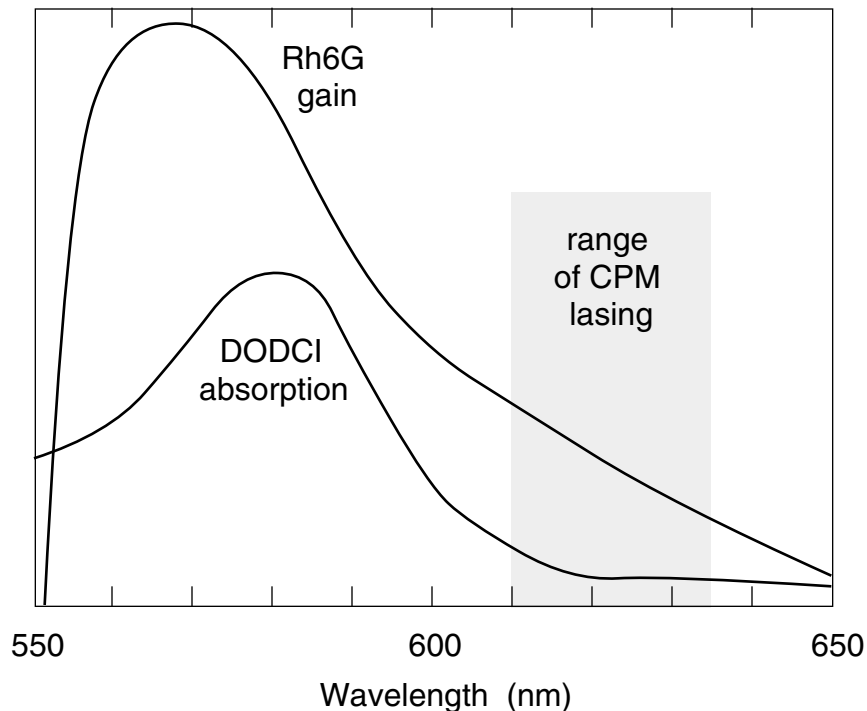


**Fig. 2.4** Wavelength range over which a CPM laser using rhodamine 6G and DODCI oscillates when producing femtosecond pulses. (Spectra after Nakazawa 1987.)

avoid significant phase distortion and broadening of the pulses. [Weiner 1985] Around the absorber jet is a similar pair of curved mirrors, with 5-cm radius of curvature. The two flat mirrors M1 and M2 are coated with single stacks optimized for *p*-polarized light at 632.8 nm and 45° incidence (Virgo Optics). The output coupler has a transmission of 3%.

The choice of gain and saturable absorber dyes dictates approximately the lasing frequency. As indicated in Fig. 2.4, the combination of rhodamine 6G and DODCI lases in the range 610–635 nm. The actual lasing wavelength is influenced

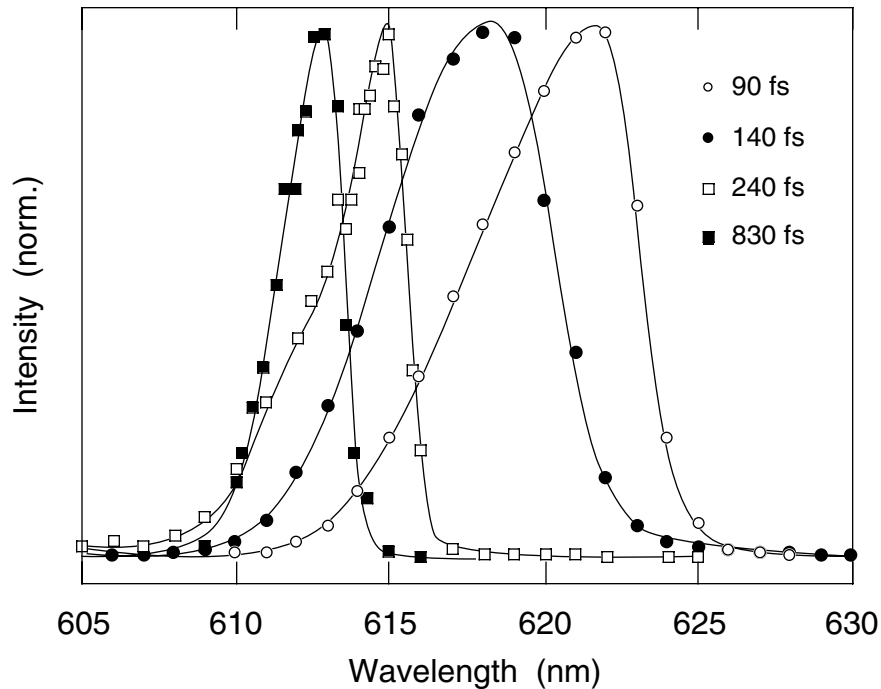


**Fig. 2.5** Spectrum of the CPM laser for various pulse durations. The spectrum broadens and shifts to longer wavelengths as the prisms are tuned to produce shorter pulses.

<sup>1</sup> In some designs a single spherical mirror is used both to focus the pump beam and to collimate the dye laser beam. In this case it is necessary to lay down first the coating stack for the pump beam, then the stack optimized at the desired lasing wavelength.

by the coatings on the mirrors and on the positioning of the prisms, as well as the degree of degradation of the gain and absorber dyes. With fresh dyes and the prisms tuned to provide 70–80-fs pulses, our CPM oscillator lases around 620 nm with a spectral width of ~8 nm as shown in Fig. 2.5.

### 2.1.2 Initial Alignment

With seven mirrors, four prisms, and two dye jets, the laser cavity is complicated. A crude estimate gives 60 translational and rotational degrees of freedom of the various components to be adjusted for “optimal” alignment. We have found it most efficient to assemble the finished oscillator step by step from simpler cavities, re-optimizing the cavity each time a new element is added. The sequence is described below and illustrated in Figs. 2.6 and 2.7.

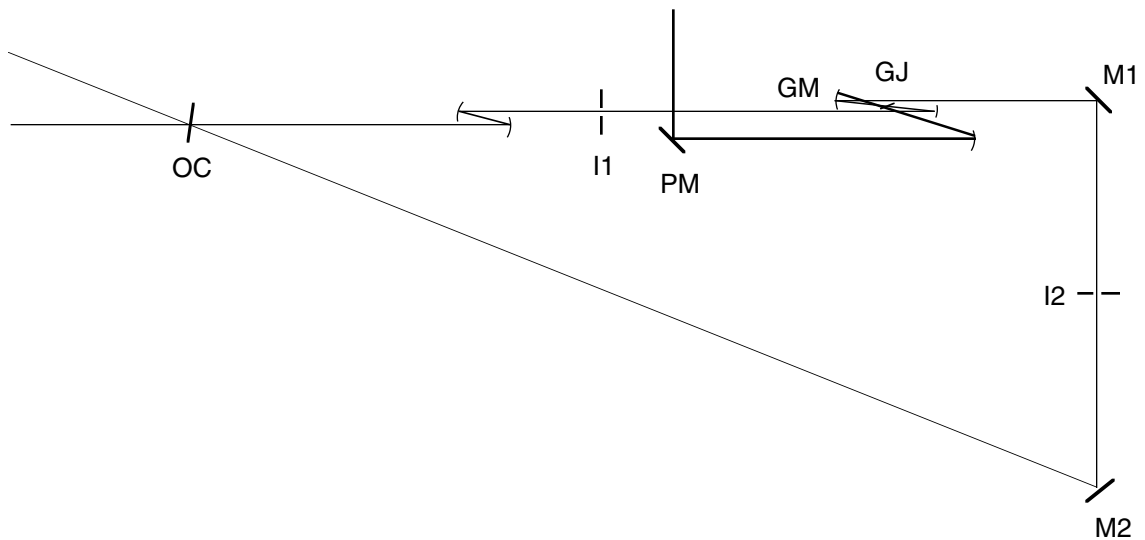


**Fig. 2.6** Simplified oscillator, without absorber jet or prisms, used to facilitate alignment. Optics are aligned with a He-Ne beam and irises I1 and I2 are set to establish the beam path. Mirror M2 and the output coupler OC are tilted to send the beam reflected from the output coupler through I1.

Most optics are mounted on inexpensive flexure mounts (Newport Corporation) as they are seldom adjusted after the initial alignment. The flat mirror that directs the pump beam to its focusing mirror and one of the curved mirrors around the gain jet (marked GM in Fig. 2.6) are mounted on gimbal mounts (Klinger Scientific) to facilitate fine adjustment. In general, the flexure mounts perform satisfactorily but are less convenient than well-built gimbal mounts. In either case, it is important to secure the optics tightly to their mounts and the mounts to the breadboard. After the optics have been mounted, the oscillator can be set up and aligned with the following procedure.

A linearly polarized He-Ne laser is mounted on the breadboard surface so that the electric field is horizontal and the beam is parallel to the surface at a height of 3 inches.<sup>1</sup> The position of the output coupler should be fixed with an eye towards the eventual position of the two jets. The He-Ne beam is directed through the center of the output coupler so that the reflected beam is directed towards the hole in the plexiglass case for the output beam. The height of the curved mirrors is adjusted to match the He-Ne beam height, and the mirrors are positioned around the absorber jet to produce a tight “zee” from which the beam emerges collimated and parallel to the input beam. The mirrors are adjusted to leave a small space between the side of the first mirror and the exiting beam so that there will be an unobstructed path for lasing. The gain zee is assembled in similar fashion and the He-Ne beam is aligned with the gain jet on to account for the displacement of the beam caused by the jet. The simple ring cavity is completed by placing the two flat mirrors M1 and M2, making sure that they do not deviate the beam in the vertical. The mirror M2 should be positioned so that a beam from the output coupler leaking through M2 will not

---

<sup>1</sup> The  $p$ -polarization of the He-Ne laser facilitates the alignment of the prisms.

mode. The tilt of mirror M2 is adjusted to overlap the He-Ne spot on the output coupler with the entering beam.

A pair of irises (I1 and I2) are used to define the beam path and to ensure that it is not altered as the prisms and absorber jet are added. Iris I1 is positioned around the beam between the two jets, making sure that it does not obstruct the pump beam. By closing the iris around the He-Ne beam and tilting the output coupler, the He-Ne reflection from the output coupler can be made to pass through the center of the iris. Iris I2 is placed between mirrors M1 and M2 to further define the beam path. At this point the simple cavity is complete. The beam height should be 3 inches at all points and the beam should pass cleanly through both two irises.

At this point the gain jet is added. The jet is run for a few minutes to let it stabilize. Once the argon laser has stabilized (roughly one hour after being powered up), the pump beam can be directed into the jet. The power should be low, only a few tenths of a watt. The pump beam height should be 3 inches with respect to the breadboard, both before and after the power mirror PM (see Fig. 2.6). The focusing mirror is adjusted to produce as small a spot as possible in the center of the jet, as observed through a neutral density filter. The pumped spot should coincide with the He-Ne beam. With the argon intensity low and the irises opened slightly, the fluorescence from the gain jet is checked along the oscillator beam path to be sure it does not diverge. The curved mirrors are adjusted, if necessary, to remove divergence and to overlap the two beams between M2 and the output coupler. Since these adjustments may alter the alignment of the He-Ne laser, it should be realigned to agree with the apertures and the fluorescence.

As the pump power is increased, the fluorescence grows and its color should shift from yellow to orange as the lasing threshold is approached. By adjusting the power mirror, the two orangish spots on the output coupler can be made to overlap, thereby aligning the cavity with respect to the pump focus. Lasing should be

observed at a power less than 4 W. Once the cavity is oscillating, the position of the power mirror should be adjusted to minimize the threshold. The other mirrors and the jet position can also be optimized to minimize the threshold. Care should be taken to ensure that the beam is round and that there are no beam waists outside the zees. When the cavity is properly aligned, the threshold is roughly 1 W. At this point the irises are moved to respect the lasing path and the He-Ne beam is realigned.

It is easier to use the He-Ne beam to align the prisms than to depend on lasing in the ring cavity, which is frequently interrupted by the prisms. Hence, the pump beam can be blocked until all four prisms have been aligned. Since a slight tilt in the plane of a prism can produce a large deflection of the beam out of the horizontal plane, the tilt of each prism must be adjusted carefully to keep the beam height at 3 inches. Furthermore, the base of the prism should be perpendicular to the direction of travel of the translation stage. The first prism (P1 in Fig. 2.7) is positioned about

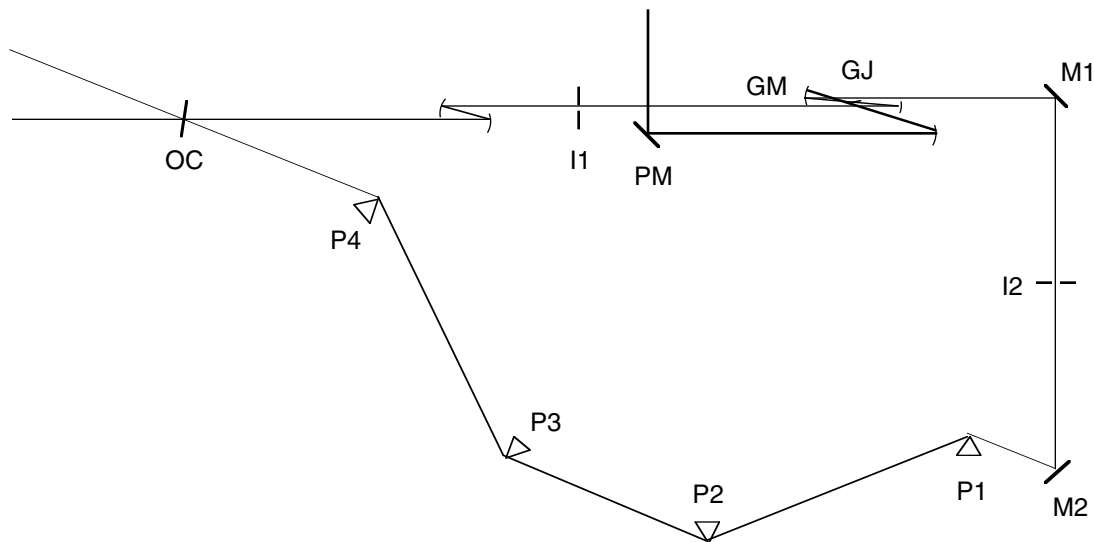


**Fig. 2.7** Aligning the prisms. The tilt of each prism should be adjusted to preserve the beam height of 3". The rotation of the prisms is adjusted to minimize reflections. The apex-to-apex distance between prisms P1 and P2 should equal that between P3 and P4.

6 inches from M2 and its rotation is adjusted to minimize the (*p*-polarized) reflection of the He-Ne beam. As it is useful to be able to remove the prisms entirely from the beam path, the prism's translation stage should be positioned accordingly. The second prism P2 is placed with its base parallel to the base of P1 at a distance of ~30 cm from the apex of P1 and checked for minimum reflection. The second pair of prisms is then added so that the apex-to-apex distances P1–P2 and P3–P4 are equal. With prisms P1 and P4 backed out half way, the He-Ne beam should separate at P1 and reunite at P4.

The final check of the prism alignment is made with the cavity lasing. The prisms are backed out completely and the pump power is increased to roughly twice the threshold. As P1 is translated slightly into the beam, a portion splits off and should pass through the other three prisms. When P1 and P4 are inserted so the entire beam is directed along the prism path, lasing is most likely interrupted. In this case, the overlap of the fluorescence from the gain jet travelling in opposite directions is checked between P2 and P3, and M2 is adjusted as necessary. Once lasing is achieved, the rotation of the prisms is checked for minimum reflection loss and the power mirror, the output coupler, and M2 are adjusted to give the lowest threshold. The threshold should be only slightly higher than without the prisms, 30% at most.

The last step is to add the absorber jet. With the pump beam blocked, the jet is added and the curved mirrors of the absorber zee are adjusted slightly if necessary to realign the He-Ne. The jet is positioned as closely as possible to the focus of the He-Ne beam. The pump beam is unblocked and its power is raised to double the threshold with prisms. The cavity may already lase, but it may be necessary to adjust the output coupler, mirror M2, and/or the power mirror. With the He-Ne off, the orangish fluorescence spot on the output coupler serves as a guide for mirror optimization. The spots must be overlapped and then the power increased until lasing

begins. Once the cavity oscillates, the jet position and the tilt of the power mirror are adjusted to obtain a large, round mode with the lowest possible threshold ( $\sim 2.7$  W).

At this point the He-Ne laser can be removed and a beam splitter inserted in its place to direct a portion of the output beam to a PIN photodiode (PD in Fig. 2.1). The output of the diode can be monitored with a  $50\text{-}\Omega$  oscilloscope channel to

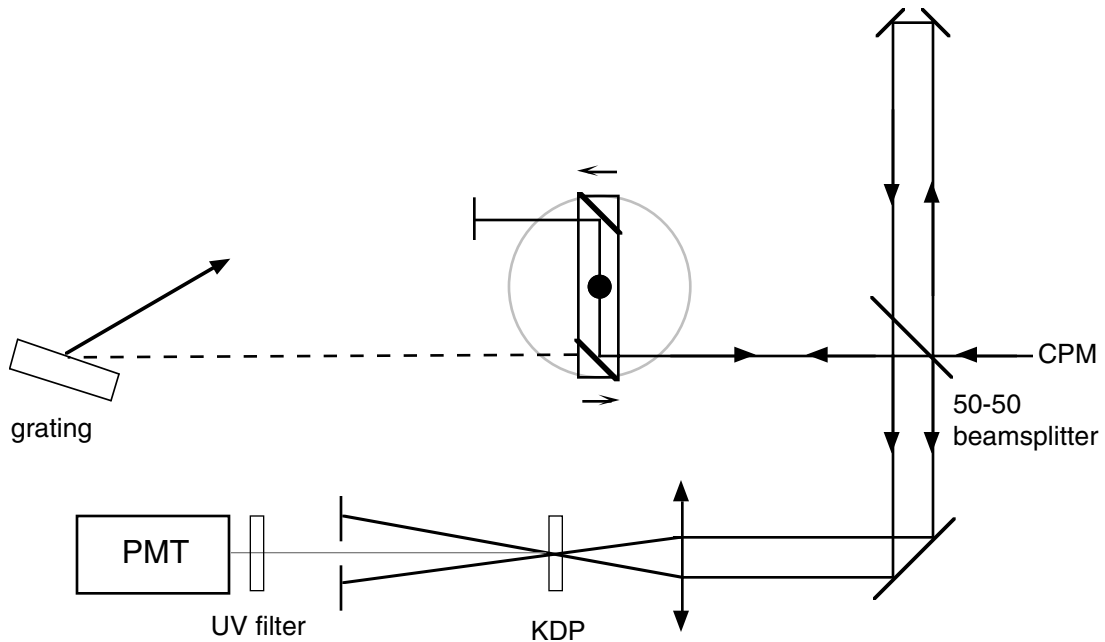


**Fig. 2.8** Rotating-arm autocorrelator. The CPM beam is divided by a 50-50 beam splitter. The reflected beam strikes a pair of mirrors forming a right angle and is retroreflected displaced by roughly 3 cm. The transmitted beam encounters two mirrors mounted on a platform (arm) that rotates at 5 Hz. When the arm is oriented as in the figure, the beam is reflected back on itself. The two parallel beams are focused by a lens into a thin crystal of KDP, producing a sum-frequency beam when the pulses overlap in time in the crystal. As the arm rotates, the path difference between the two legs sweeps through zero, at which point the sum frequency signal is a maximum. A filter blocks visible light, passing the UV to a photomultiplier tube. The output of the PMT is observed on a  $1\text{-M}\Omega$  oscilloscope channel in parallel with a  $20\text{-k}\Omega$  resistor to achieve the proper temporal smoothing. Note that since successive pulses are separated by 8 ns, corresponding to 2.7 m, a pulse is never correlated with its predecessor or successor.

resolve the pulse train. The rest of the beam enters the rotating-arm autocorrelator, which is illustrated in Fig. 2.8. In the autocorrelator, the pulse is divided into two by a 50-50 beam splitter. One pulse travels a fixed-length delay line while the other sees a delay path that varies with time. After retroreflection the beams emerge parallel from the beam splitter and are overlapped spatially inside a nonlinear crystal. When the path length in the two arms is the same, the two pulses arrive simulta-

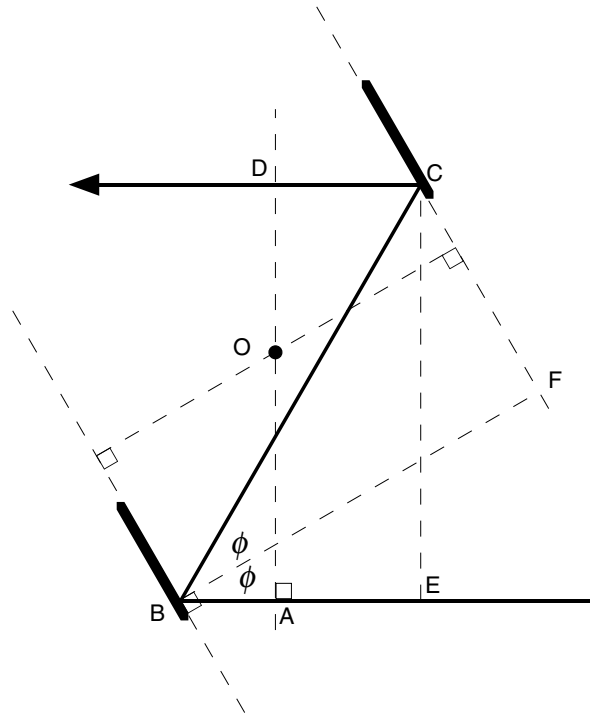


**Fig. 2.9** Geometry of the rotating-arm autocorrelator. The path length followed by the light in a double pass is a constant plus  $s = 2(\overline{AB} + \overline{BC} + \overline{CD})$ . Since  $\overline{CD} = \overline{EA}$ ,  $s = 2(\overline{EB} + \overline{BC})$ . Let  $d$  equal the perpendicular distance between the mirror planes  $\overline{BF}$ . Then  $\overline{BC} = d \sec \phi$  and  $\overline{EB} = \overline{BC} \cos 2\phi$ . Hence,  $s = 2(d \sec \phi) \times (1 + \cos 2\phi) = 4d \cos \phi$ . If the arm rotates about  $O$  at  $d\phi/dt = 2\pi f$ , the rate of change in the path length with respect to time is  $ds/dt = -8\pi f d \sin \phi$ , and the rate of change in the time delay for a pulse propagating at  $c$  is  $|d\tau/dt| = (8\pi f d/c) \sin \phi$ . For our autocorrelator,  $d = 4.3$  cm,  $f = 5$  Hz, and  $\phi = 60^\circ$ ,  $d\tau/dt = 1.56 \times 10^{-8}$ . Hence,  $1 \mu\text{s}$  on the oscilloscope corresponds to  $15.6$  fs for the autocorrelation and  $11$  fs for the pulse width (assuming a Gaussian envelope).

neously at the doubling crystal and a peak in the second-harmonic signal is detected along the path bisecting to the two beams. As the arm rotates the path length changes (see Fig. 2.9), causing one pulse to be slightly delayed with respect to the other, which decreases the second-harmonic signal. By using a detector with a response time that averages over several pulses, the autocorrelation can be seen directly on an oscilloscope with the time scale stretched by the factor

$$\frac{dt}{d\tau} = \frac{c}{8\pi f d \sin\phi} \approx 6.4 \times 10^7 . \quad (2.1)$$

In this expression,  $f$  is the frequency at which the arm rotates,  $d$  is the perpendicular distance between the mirror planes,  $\phi$  is the angle of incidence at the mirror, and  $c$  is the speed of light (see Fig. 2.9). The relation between the autocorrelation signal and the actual pulse duration is discussed in § 2.4.

The grating behind the rotating arm provides a simpler and equally useful diagnostic tool. When the arm is oriented to permit the beam to pass, the grating disperses the pulse spectrum on the wall. When proper mode-locking is achieved, the spectrum broadens and displays an intensity pattern that increases gradually with wavelength, then decreases rapidly. Often it is most efficient to tune the prisms and absorber jet while observing the spectrum to monitor the mode-locking, consulting the autocorrelator for final verification.

### 2.1.3 Daily Operation

Stable operation of the CPM laser requires the pump laser, and to a lesser degree the dye solutions, to attain steady temperatures. Tweaking the alignment of the oscillator before the argon laser has warmed up merely wastes time. We typically run the argon laser at an output slightly above the previous day's operating power for an hour before touching the alignment of the oscillator. During this time, the beam is blocked with a beam stop. It is probably not a bad idea to run the dye

systems during this warm up time, too. At hour's end, we check the prisms for dust and clean them carefully with a methanol-soaked cotton swab, if necessary. This should be done every few days even if there is no obvious dust, as a film of ethylene glycol gradually collects on the prism faces. With the pump power low and the beam unblocked, the focal spot of the argon beam should be centered in the gain jet. As the power is raised, the characteristic orange glow should develop in a single spot on the output coupler. The power mirror and the pump power are adjusted to brighten this spot until the cavity lases.

Next the absorber jet is aligned. With the power about 2 W above threshold, the jet position and the power mirror are adjusted to produce a stable interference grating in reflection from the absorber jet. Then the pump power is lowered to a few tenths of a watt above threshold to restore mode-locking.

Over the course of the day, it is necessary to adjust the power mirror and argon power level slightly every so often. It may also be necessary to adjust the absorber jet position using the method outlined in the previous paragraph. When stability is poor, check also for dust on the prisms and optics and instabilities in the dye jets. The jets should contact the catcher tubes far from the nozzle, preferably at the node in the stream. If the surface of the dye stream is not flat, the pressure can be varied slightly and if necessary, the nozzle should be checked for blockage.

## **2.2 Amplifier**

The development of low repetition rate amplifiers for femtosecond optical pulses followed soon after the invention of the CPM laser. [Fork 1982, Migus 1982, Fork 1983, Valdmanis 1984]. A satisfactory amplifier design must overcome a number of difficulties arising from linear and nonlinear dispersion of the pulse in the gain medium as well as a variety of pulse-distorting nonlinear interactions, including

nonlinear frequency generation, wavelength-dependent gain, saturable absorption, gain saturation, self-phase modulation, and self-focusing. In general, the nonlinear distortions are held to acceptable levels by keeping the light intensity low enough, and the linear chirp impressed on the pulse by normal group velocity dispersion is removed with either a grating or prism pulse compressor after the final stage of amplification. The resulting pulses have a temporal width only slightly greater than the femtosecond seed pulse and peak powers in the gigawatt range.

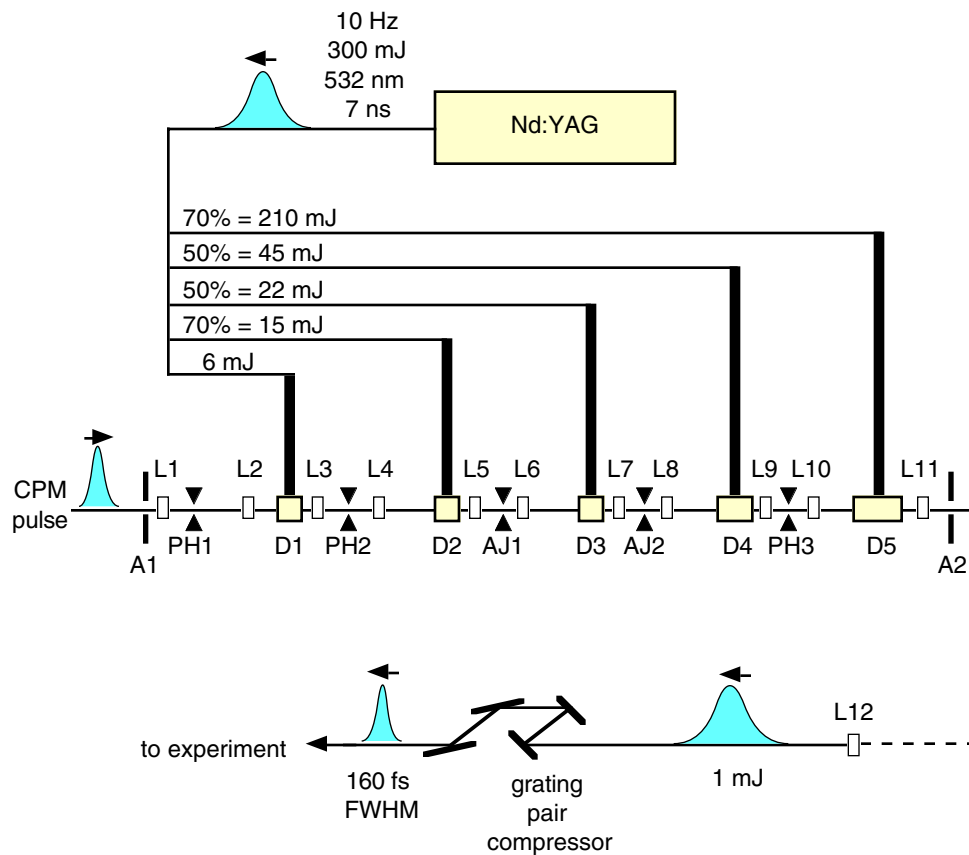


**Fig. 2.10** Schematic overview of the 10-Hz GW femtosecond amplifier. Five prism dye cells (D1-5) are pumped by the 532-nm output of a 10-Hz Nd:YAG laser. Lens pairs (L1-L2, etc.) relay the image of aperture A1 to successive dye cells, expanding the beam in the process. Pinholes (PH1-3) and saturable absorber jets (AJ1-2) reject amplified spontaneous emission and unamplified pulses. A grating pair compresses the final pulses to a width of 160 fs (FWHM).

The layout of the amplifier is indicated schematically in Fig. 2.10. A doubled Nd:YAG laser (Quintel International [Continuum] model 661-10), producing 300-mJ, 7-ns pulses at the second-harmonic wavelength of 532 nm transversely pumps 5 prism dye cells of increasing size. The Q-switch in the YAG laser is synchronized to the pulse train of the CPM laser measured by a photodiode (PD in Fig. 2.2) using a pulse synchronization module (Spectra Physics model SM-1) with an adjustable delay. The femtosecond seed pulse is clipped by an aperture (A1) that passes roughly the central third by diameter to produce a “top hat” profile. Lens pair L1 and L2 forms an inverse telescope that reduces the beam diameter to approximately 0.9 mm for amplification in the first prism dye cell (D1). Successive lens pairs expand the beam and relay the image to successive dye cells. Pinholes (PH1-PH3) and saturable absorber jets (AJ1-AJ2) of malachite green in ethylene glycol partially isolate adjacent stages and reduce amplified spontaneous emission from the photo-excited dye. The jets also trim the leading edge of the pulse. [Fork 1982] After the final cell (D5), a pair of 0.5-m focal length lenses (L11-L12) relays the aperture image through a grating compressor. The resulting pulses have 160-fs duration (FWHM) centered at  $\lambda = 623$  nm.

### **2.2.1 Prism Dye Cells**

The amplifier has been designed to produce a beam with a well-characterized smooth spatial profile. In a longitudinally pumped amplifier, the spatial mode of the pump beam is impressed on the amplified beam. If the mode has hot spots or other defects, these can degrade the beam profile excessively. Transverse pumping avoids this problem, but can introduce spatial mode distortion as well. In standard transverse pumping, the excitation beam is focused by a cylindrical lens to a line towards the back of the dye cell. The beam being amplified is sent through as close to the

front face of the cell as possible to extract the greatest gain. However, the exponential absorption of the pump light produces a transverse gradient in the gain that distorts the profile of the amplified beam. Several alternative transversely pumped cells have been developed to provide high gain with a minimum of pulse distortion. [Bethune 1981, Schäfer 1986, Kuhnle 1988] Our amplifier uses five prism dye cells of the type invented by D. S. Bethune. [Bethune 1981]

A cross section of a Bethune prism dye cell is shown in Fig. 2.11. A hole is drilled parallel to the axis of a right-angle glass prism (Esco Products) as indicated in the figure. Pump light in an expanded, collimated beam enters the front face of the prism and is directed to all four sides of the hole by total internal reflection

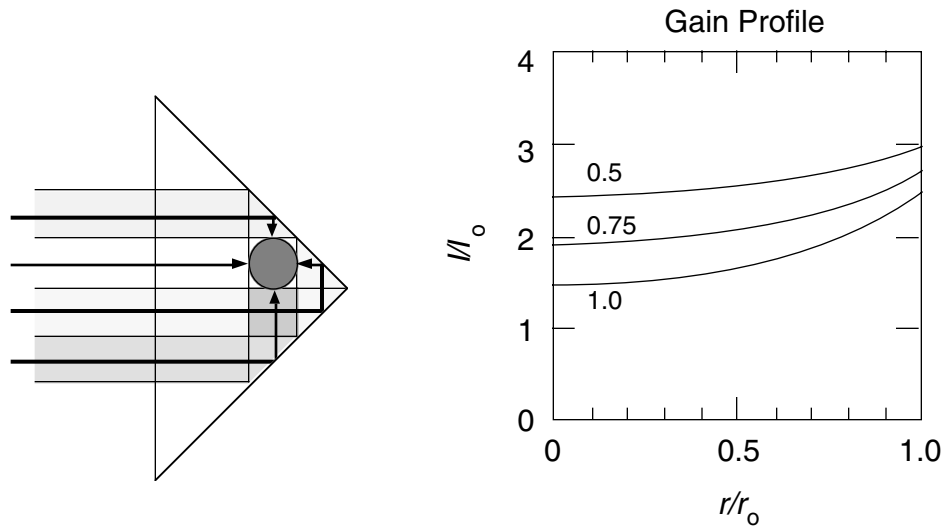


**Fig. 2.11** Cross section of a transversely pumped prism dye cell. The dye solution and beam to be amplified pass down the bore of a hole drilled parallel to the axis of a right-angle prism. The pump beam is expanded to four times the diameter of the hole and aligned so that the different portions of the beam illuminate the hole from all four sides by total internal reflection of the light inside the prism.

The gain profile is fairly flat at the center of the hole, increasing somewhat towards the perimeter. Increasing the dye absorption constant  $\alpha$  increases the total gain at the expense of introducing a bright ring from high gain at the perimeter. A slight azimuthal dependence near the perimeter has been suppressed in the figure.

inside the prism. The four pump “beamlets” are exponentially attenuated at a rate given by the absorption constant  $\alpha$  of the dye solution. If the pump beam is uniform across its profile, and the dye solution is index-matched to the glass so that no refraction occurs at the perimeter of the hole, the pump intensity at a position  $(x,y)$  inside the hole of radius  $r_0$  is given by

$$\frac{I}{I_0} = e^{-\alpha(\sqrt{r_0^2 - x^2} - y)} + e^{-\alpha(\sqrt{r_0^2 - x^2} + y)} + e^{-\alpha(\sqrt{r_0^2 - y^2} - x)} + e^{-\alpha(\sqrt{r_0^2 - y^2} + x)}, \quad (2.2)$$

where the coordinate system is centered at the hole and aligned with the incoming beam. The intensity turns out to be only weakly dependent on the azimuthal angle  $\phi = \tan^{-1}(y/x)$  for  $r \geq 0.7r_0$ , and this dependence has been suppressed in Fig. 2.11.

The gain profile, assumed to be proportional to the pump intensity, has a minimum at the center of the cell and increases more steeply near the perimeter of the hole. The pumping nonuniformity increases with  $\alpha$ , so that better amplified profiles are obtained for small  $\alpha$ . However, the total gain of the cell also increases with  $\alpha$ , leading to a trade-off between profile and energy. The best compromise, in our experience, is for  $\alpha r_0$  between 0.7 and 0.8.<sup>1</sup>

The gain profile is slightly modified for a nonuniform pump beam. Our dye cells are pumped by a roughly Gaussian Nd:YAG profile expanded by a pair of diverging cylindrical lenses with crossed axes, and collimated with a large spherical lens. The resulting pump intensity profile is elliptical, having different Gaussian widths in the vertical and horizontal directions. The central portion of the beam, which pumps the front and back of the hole (see Fig. 2.11), is stronger than the

---

<sup>1</sup> Note that the exponential absorption constant  $\alpha$  refers to base  $e$ , not base 10.

pumping, provided the Gaussian is not too narrow, the gain profile remains reasonably smooth and uniform, as illustrated in Fig. 2.12.

The prisms are mounted between wedged flanges that channel the dye solution down the prism hole and admit the beam through plane windows. For large prisms thin teflon gaskets are inserted between the end faces of the prism and the wedged flanges. Four tapped spacer bars machined to the length of the prism plus the thickness of a single gasket are used to seal the flanges against the prism and to avoid overstressing the glass. For smaller prisms, a satisfactory seal is made with silicone rubber. In this case the spacer bars are about 0.008" longer than the prism. A bead of sealer is placed around the hole on the end face of the prism. Then a teflon dowel is inserted through the hole in the flange and into the hole in the prism. The

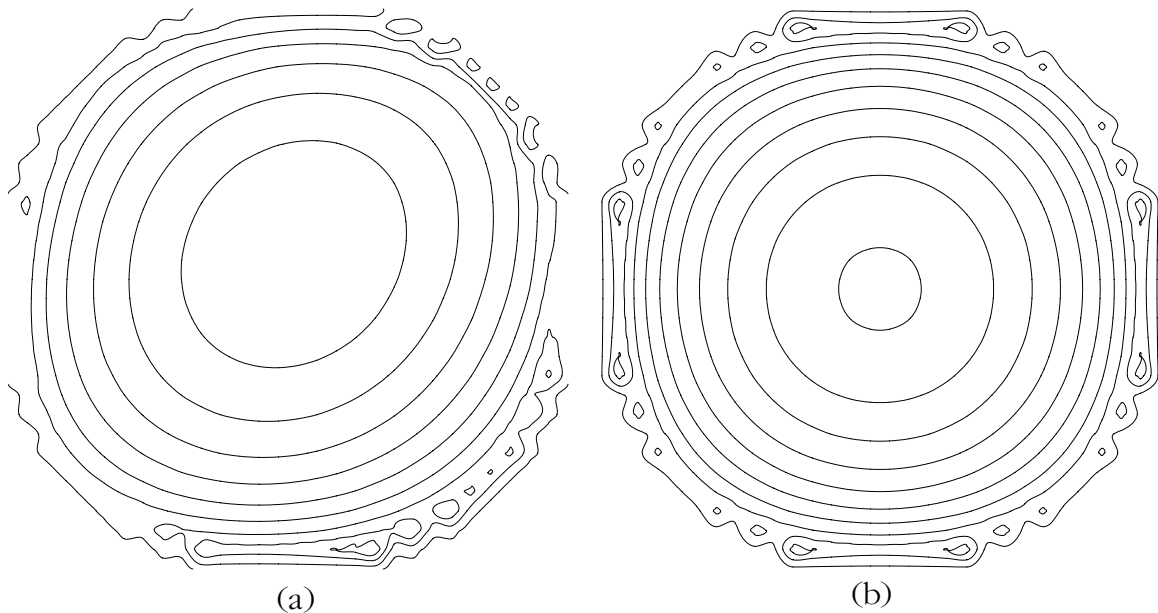


**Fig. 2.12** (a) Contour plot of the gain profile of a prism dye cell pumped with a Gaussian beam. The beam enters from the left as in Fig. 2.11, which leads to a maximum in the gain near the bottom of the hole and a more pronounced departure from azimuthal symmetry than in the case of uniform pumping illustrated in (b). The computation is for  $\alpha r_0 = 0.75$  and the Gaussian width of the pump beam in (a) is twice the diameter of the hole.

dowel both facilitates alignment and prevents the sealer from clogging the hole. After both flanges have been aligned, the spacer bars are tightened slightly and the dowels are rotated to ensure proper alignment. When fully tightened, the dowels are removed and the cell is checked to be sure no silicone rubber obstructs the hole. The silicon rubber should be allowed to dry overnight before the cell is tested for leaks.

From Fig. 2.11 it is clear how a hole of radius  $r$  must be positioned with respect to the right angle of the prism in order for the four beamlets to pump the dye properly. This leaves a thin wall of glass of thickness  $r(\sqrt{2} - 1) \approx 0.4r$ . For a 1-mm diameter hole, as is used in the first dye cell, this is barely more than  $200 \mu\text{m}$  of glass. Juen-Kai Wang proposed a modified Bethune cell that enables this minimum thickness to be increased over four times to  $r(2\sqrt{2} - 1) \approx 1.8r$ . This design is illustrated in Fig. 2.13. Although such a prism has improved mechanical strength, it has a pair of optical drawbacks. First, if the pump beam is not perfectly collimated and incident normal to the prism face, the rays can deviate considerably from the ones indicated in the figure, and even miss the hole entirely. Second, the beamlets travel different path lengths before encountering the hole. For example, beamlet *a* of

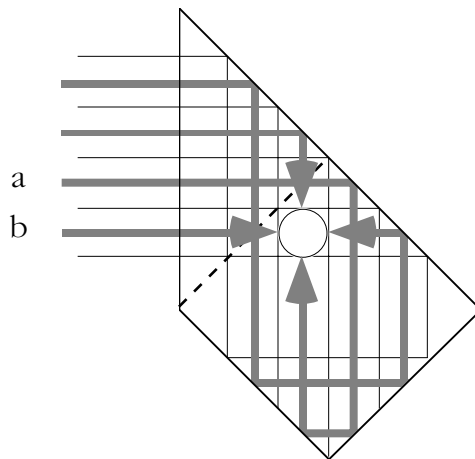


**Fig. 2.13** Modified prism dye cell with greater minimum glass thickness.

Fig. 2.13 lags beamlet  $b$  by approximately  $\Delta t = 2wn/c$ , where  $w$  is the width of the face through which the beamlets enter the prism. This amounts typically to a few tenths of a nanosecond. For a 7-ns pump pulse, this difference is negligible. With a shorter pump pulse, however, it may make it more difficult to synchronize the pump and amplified beams. We have found it expedient to order a few extra cells of small bore in the conventional design of Fig. 2.11 and to take great care in assembling them.

### 2.2.2 Pumping

The 300-mJ energy of the pump beam is divided by a series of beam splitters between the five dye cells as indicated in Table 2.1. The dye solution of the first cell is Kiton red 620 (sulforhodamine 620) in a 1.5% aqueous solution of ammonyx LO surfactant. In aqueous solution, Kiton red has a base- $e$  absorptivity of  $8.68 \times 10^4 \text{ l mol}^{-1} \text{ cm}^{-1}$ , so that a  $1.7 \times 10^{-4}$ -M solution gives the proper absorption

Stage	Bore diameter	Length	Pump Energy	Approx. Gain
1	1 mm	20 mm	6 mJ	1500
2	3 mm	25 mm	15 mJ	35
3	3 mm	38 mm	22 mJ	15
4	6 mm	38 mm	45 mJ	2
5	12 mm	70 mm	210 mJ	16

**Table 2.1** Parameters of prism dye cells. The gain of the second and third stages is measured after the respective saturable absorber jet.

constant ( $\alpha r_0 = 0.74$ ). The dye solution in the remaining cells is sulforhodamine 640 in 1.5% aqueous ammonyx LO, which has a base- $e$  absorptivity of  $6.13 \times 10^4 \text{ l mol}^{-1} \text{ cm}^{-1}$ . Kiton red is used in the first stage because its absorption spectrum is shifted slightly to the orange with respect to the absorption spectrum of the more efficient sulforhodamine 640, and therefore unpumped volumes of dye in the first cell do not significantly attenuate the beam. [Fork 1982]

### 2.2.3 Relay Imaging

Distortion of the beam as it passes down the amplifier chain is minimized by achromatic lenses, spatial filters, saturable absorber jets, and relay imaging. Because space is limited on the optical table, fairly short focal length (4–10 cm) lenses are used between amplification stages. Consequently, achromatic lenses are used to reduce chromatic aberration for  $f$ /numbers less than 25. Single-stack anti-reflection coatings on the lenses reduce reflections that can give rise to lasing in individual gain cells. Pinholes (Fort Wayne Wire Die) are placed at the focus between cells 1 and 2, and between cells 4 and 5 to reject spontaneous emission and to clean up the beam profile slightly (see Fig. 2.10). The pinholes have diameters several times the size of the central Airy disk, given by [Hecht 1979]

$$d = \frac{2.44f\lambda}{D}, \quad (2.3)$$

where  $D$  is the collimated beam diameter,  $f$  is the focal length of the lens, and  $\lambda$  is the wavelength. Two saturable absorber jets of the dye malachite green in ethylene glycol are placed near the focus between cells 2 and 3 and between cells 3 and 4. The jets use standard 200- $\mu\text{m}$  dye nozzles (Coherent) and the dye concentration is adjusted to give a small-signal attenuation of  $\sim 500$ . The absorber jets strongly reduce amplified spontaneous emission from the gain cells and attenuate the leading edge of the pulses, which see the highest gain. To avoid self-phase modulation

and continuum generation, particularly in the second absorber, the jet is slightly displaced from the focus.

The lenses and dye cells are positioned to avoid diffraction distortion of the beam profile, [Murnane 1988] as indicated in Fig. 2.14. The relayed image of the initial aperture (see Fig. 2.10) is close enough to the first lens that the effective object for the second lens is roughly at the position of the first lens. As indicated in the figure, the second lens produces an inverted image of this object at a distance  $f_2(1 + f_2/f_1)$  behind the second lens, near the exit of the amplifier cell.

### 2.2.4 Setup and Alignment Procedure

Like the CPM oscillator, the amplifier is complicated, with dozens of degrees of freedom. Care must be taken to ensure that the beam travels down the axis of each gain cell, that stray reflections are not amplified, that the beam passes cleanly through the pinholes and through the central flat portion of the absorber jets, that the pump beams enter the prism dye cells properly collimated and at the right angle

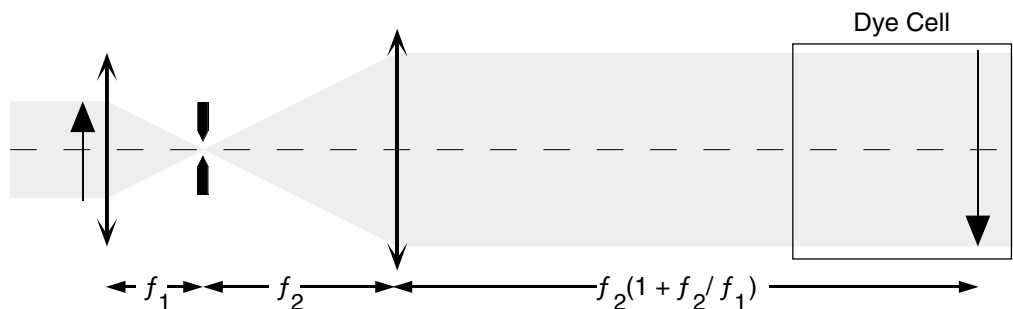


**Fig. 2.14** Relay imaging in the amplifier chain. Lenses of focal length  $f_1$  and  $f_2$  form a telescope that expands the collimated beam by  $f_2/f_1$ . An image of the initial aperture (arrow at left) forms the object for lens  $f_2$ , which produces an inverted image near the exit of the dye cell. At the focus between the lenses, an aperture helps remove stray light from the previous stage and preserve the uniform, filled-in beam profile.

and height, and that the seed pulse and the YAG pulse arrive with the necessary synchronization. For this we have developed the following setup and alignment procedure.

Two widely-separated irises are positioned on the CPM beam path before an aperture (A1 of Fig. 2.10) clips the beam to create the top hat profile. The irises define the beam path; before daily realignment of the amplifier optics, the beam is centered on these two irises. Two hairs taped in an *X* over the aperture A1 create an easy-to-see object for relay imaging. Lens L1 is placed as close as practicable to A1, and L2 is positioned to produce a horizontal collimated beam. Pinhole PH1 is added and its position adjusted to eliminate diffraction rings. Using a white card, the image of the cross hair in A1 is located and the first gain cell is positioned so that the image is formed near the exit window. The cell is aligned (with dye solution circulating) by placing a lens after the cell and examining the diverging beam for roundness and centering through the bore of the prism.

Lens pairs L3–L4 and L5–L6, pinhole PH2, and dye cells D2 and D3 are added in a similar fashion, making sure that the beam height is preserved and cells are positioned about the relayed image. Because the gain in the first cell is so high, lasing can occur off the slight reflection from lenses around the cell. Consequently, lens L3 should be angled slightly to reduce back reflection into the gain medium. The first absorber jet AJ1 should be on when L6 and D3 are positioned because it is thick enough to perturb the beam path slightly.

If the jet already has malachite green in it, the beam will be sufficiently attenuated that alignment of the subsequent stages is difficult without pumping the first stages. The diverging cylindrical lenses and collimating spherical lenses should be positioned as far from the gain cells as is convenient and their height adjusted to match the center of the four pump beamlets (see Fig. 2.11). The mirrors guiding the pump beam should also be adjusted to deliver the beam to the first lens horizontally

at the proper height. A PIN diode and 50- $\Omega$  oscilloscope amplifier are used to monitor the amplified pulse while the timing of the Nd:YAG pulse and the tilt of the pump mirrors are adjusted to maximize the gain. A 620-nm interference filter before the diode cuts out stray green light and calibrated neutral density filters allow a comparison of the pumped and unpumped signal level. Any optics that cause lasing when the seed pulse is blocked at various points on the beam path before the cell should be tilted until the lasing disappears. The gain in the first cell should be 1500–3000.

The pump optics for cells D2 and D3 are aligned and the amplified beam profile after the second absorber jet is monitored while adjusting the pumping of the first three cells to produce a round, uniform profile. The timing of the Nd:YAG pulse is also adjusted for maximum energy. If the intensity is too high in the second absorber jet, it can cause breakdown and continuum generation. In this case the jet should be moved away from the focus to suppress these nonlinear effects. After the final two cells and pinhole have been added, the pumping is optimized to produce maximum energy and a round profile. The dimensions and approximate gain of the five amplifier cells are listed in Table 2.1 and the final energy averages  $\sim 1$  mJ. It is also possible to double-pass the final cell to give an average pulse energy of  $\sim 2$  mJ.

## **2.3 Pulse Compression**

The pulses encounter roughly 20 cm of aqueous dye solution and 16 cm of glass in travelling down the amplifier chain. Consequently, normal dispersion broadens the pulses to roughly 700 fs. To a high approximation, the dispersion produces a linear frequency sweep or chirp that can be removed by either a prism pair [Fork 1984, Kafka 1987] or a grating pair. [Treacy 1969] Prism pairs have the advantage of low loss near Brewster's angle. They also have three main disadvantages:

long path lengths, somewhat awkward adjustment, and possible pulse distortion at high intensity. [Murnane 1988] Grating pairs cause more loss, but are easier to tune and align, and do not distort the pulse at high intensity. We have found that pulses compressed with a pair of 600-lines/mm gratings (Milton Roy) degrade more slowly with distance and focus better than those compressed with a prism pair.

The grating compressor is tuned by adjusting the separation of the gratings. For a perpendicular distance  $d$  between the gratings, line spacing  $\delta$ , and incidence angle  $\theta$ , the dispersion compensation is given by the expression [Treacy 1969]

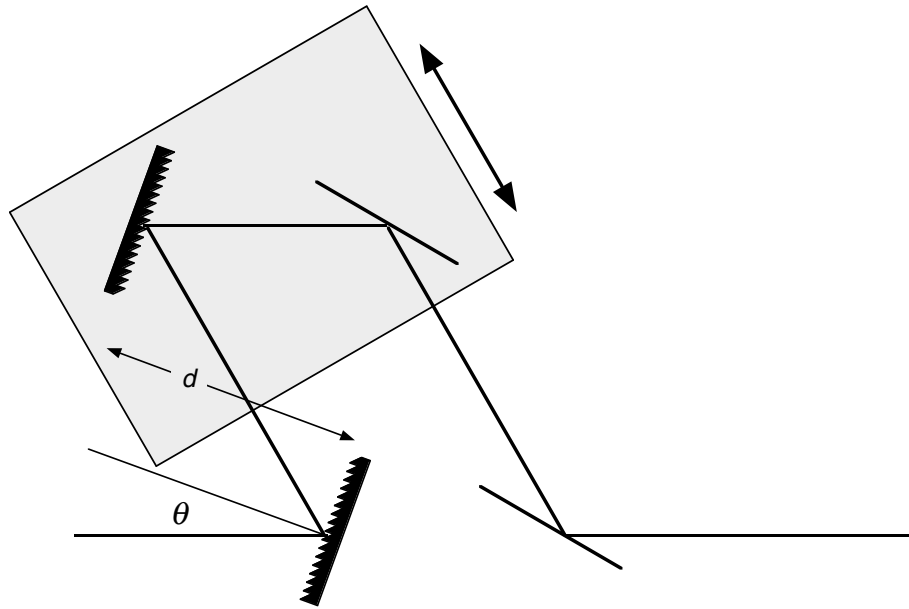


**Fig. 2.15** A pair of matched gratings and a pair of mirrors provide continuously tunable dispersion compensation without altering the subsequent beam path. The second grating and first mirror are mounted on a translation stage that varies the slant separation of the gratings. For higher throughput, the mirrors can be removed, but then tuning produces a lateral displacement of the beam. There is a small lateral displacement of the different wavelength components of the beam, which is estimated to be less than  $\sim 0.5$  mm. Since the beam diameter is greater than 1 cm, this displacement does not noticeably affect the subsequent focusing of the beam.

$$\frac{\partial \tau}{\partial \lambda} = \frac{d\lambda}{c\delta} \frac{1}{\delta[1 - (\lambda/\delta - \sin\theta)^2]^{3/2}} \quad (2.4)$$

Tuning the dispersion compensation by changing  $d$ , however, shifts the output beam parallel to itself. This complicates the alignment of subsequent optics. By adding a pair of mirrors in a configuration due to Fork, [Greene 1988] the beam path after the compressor remains unaltered during tuning, as illustrated in Fig. 2.15.

## 2.4 Autocorrelation

The accurate characterization of the amplitude and phase of short laser pulses requires an interferometric technique. [Diels 1985] Interferometric autocorrelation can reveal not only the intensity envelope, but also information about the frequency

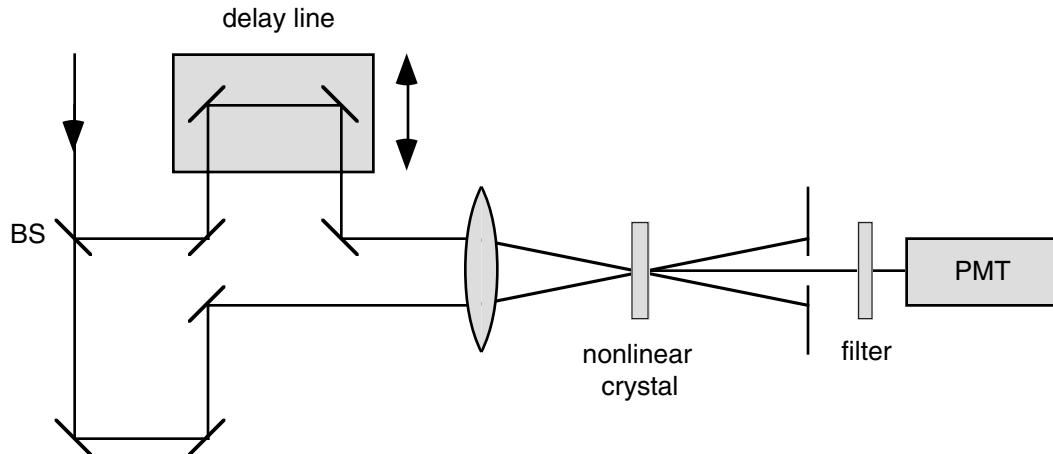


**Fig. 2.16** Experimental configuration for a standard intensity autocorrelation. The beam is divided by a beam splitter. One beam is sent through a variable-length delay line, while the other travels a fixed delay. A lens focuses both beams so they overlap inside a thin nonlinear crystal, such as KDP, which produces light at the sum frequency when the beams overlap in time. A filter rejects light at the fundamental frequency. A photomultiplier tube temporally integrates the light at the second harmonic over the pulse duration.

sweep or chirp of the pulse. However, it reveals this information only after considerable numerical analysis. A zero-background intensity autocorrelation [Ippen 1975] gives the symmetrized pulse duration directly, at the expense of loss of information on chirp. A typical experimental setup to perform such an autocorrelation is indicated in Fig. 2.16. An autocorrelation trace is taken by stepping the delay stage repeatedly by a fixed displacement (typically 1  $\mu\text{m}$ ), averaging a certain number of laser shots at each position. The change in the optical path length is twice the stage displacement in this double-pass arrangement. Hence each micrometer of stage delay corresponds to a time delay of  $2 \mu\text{m} / 3 \times 10^8 \text{ m/s} = 6.7 \text{ fs}$ .

The signal registered by the photomultiplier tube is proportional to the integral of the intensity product of the two pulses [Diels 1985]

$$I_{\text{AC}}(\tau) = k \int_{-\infty}^{\infty} I(t)I(t - \tau) dt , \quad (2.5)$$

where  $I(t)$  is the pulse intensity and  $k$  is a constant that depends on details of the focusing and the nonlinear medium used to produce the sum-frequency signal. Regardless of the symmetry of  $I(t)$ , the intensity autocorrelation  $I_{\text{AC}}(\tau)$  is an even function of  $\tau$ , as can be seen by shifting the origin of the dummy integration variable by  $\tau / 2$

$$I_{\text{AC}}(\tau) = k \int_{-\infty}^{\infty} I(t + \tau/2)I(t - \tau/2) dt . \quad (2.6)$$

Hence, asymmetries in the pulse, such as chirp, are masked in the intensity autocorrelation.

From  $I_{\text{AC}}(\tau)$  one would like to infer  $I(t)$ . This can be accomplished by assuming a functional form for  $I(t)$ , computing  $I_{\text{AC}}(\tau)$  by Eq. (2.6), and fitting this function to the experimental data. Gaussian and hyperbolic secant functions are commonly used. For a Gaussian pulse of the form

$$I(t) = e^{-(t/t_p)^2}, \quad (2.7)$$

the autocorrelation is also a Gaussian function of width  $\tau_p = t_p\sqrt{2}$ . For the hyperbolic secant pulses expected from a CPM laser, [Diels 1985]

$$I(t) = \operatorname{sech}^2(t/t_p), \quad (2.8)$$

the intensity autocorrelation function has the form

$$I_{\text{AC}}(\tau) = k \times 3 \frac{\left( \frac{\tau}{t_p} \coth\left(\frac{\tau}{t_p}\right) - 1 \right)}{\sinh^2\left(\frac{\tau}{t_p}\right)}, \quad (2.9)$$

as can be verified by contour integration. Having extracted  $t_p$  from the fitting procedure the pulse full width at half maximum is given by

$$\Delta t_{\text{FWHM}} = t_p 2\sqrt{\ln(2)} \approx 1.665 t_p \quad (\text{Gaussian}) \quad (2.10)$$

and

$$\Delta t_{\text{FWHM}} = t_p 2\ln(\sqrt{2} + 1) \approx 1.763 t_p \quad (\text{hyperbolic secant}). \quad (2.11)$$

Some indication of the residual chirp in a pulse can be obtained by comparing the pulse's time-bandwidth product to the transform limit. For a pulse with intensity profile  $I(t)$  in the time domain, the intensity profile of the transform-limited pulse in the frequency domain is given by

$$I(\omega) = \left\{ \int_{-\infty}^{\infty} dt e^{i\omega t} \sqrt{I(t)} \right\}^2. \quad (2.12)$$

For the Gaussian and hyperbolic secant pulse shapes, this gives

$$I(\omega) = e^{-\omega^2 t_p^2} \quad (\text{Gaussian}) \quad (2.13)$$

and

$$I(\omega) = \operatorname{sech}^2\left(\frac{\pi\omega t_p}{2}\right) \quad (\text{hyperbolic secant}). \quad (2.14)$$

In terms of the full width at half maximum of the pulse in both the time and frequency domain, the time-bandwidth product is

$$\Delta\omega \cdot \Delta t = 4\ln 2 \approx 2.773 \quad (\text{Gaussian}) \quad (2.15)$$

and

$$\Delta\omega \cdot \Delta t = \frac{8}{\pi} [\ln(\sqrt{2} + 1)]^2 \approx 1.978 \quad (\text{hyperbolic secant}). \quad (2.16)$$

### 2.4.1 Angle Broadening of the Autocorrelation

Refractive optics in the beam path after the pulse compressor introduce chirp and can temporally broaden the pulse before it is used in an experiment. In order to produce the shortest possible pulses at the sample, it is best to perform the pulse autocorrelation at the sample position. In this way, the compressor can be adjusted to compensate not only the chirp introduced during amplification, but also the chirp caused by the optics used in the experiment.

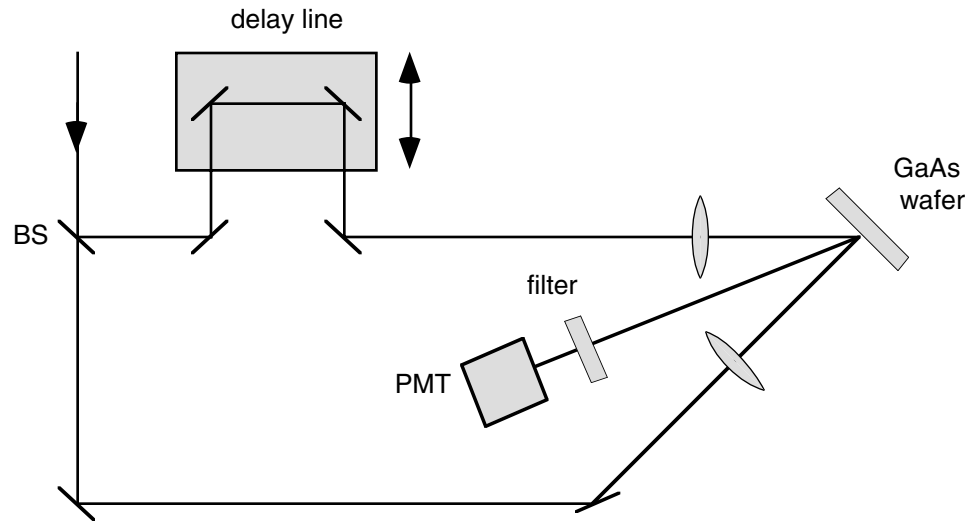


**Fig. 2.17** Setup for a large-angle autocorrelation using a GaAs wafer to produce the second-harmonic signal. The angle between the beams introduces a broadening of the autocorrelation signal that depends on the angles of incidence, the spatial extent of the beams, and the pulse duration.

For the GaAs laser melting experiment described in the following chapter, the GaAs sample itself can be used as the nonlinear crystal for the autocorrelation, as indicated in Fig. 2.17. Because the beams enter at different angles, the measured autocorrelation is broadened. In the geometry used in the experiment, the pump pulse is incident along the sample normal and the probe beam enters at  $45^\circ$ . If we assume a Gaussian pulse shape, the amount of broadening can be estimated as follows. Let  $I_1$  and  $I_2$  be Gaussian beams of the form

$$I_i(x_i, y_i, z_i, t) = \exp\left\{-\frac{(x_i^2 + y_i^2)}{\rho_i^2} - \left(\frac{t - z_i/c}{t_i}\right)^2\right\} \quad (2.17)$$

incident at angles  $\theta_1$  and  $\theta_2$  on the GaAs surface, as indicated in Fig. 2.18. Each beam propagates along its  $z$ -direction, has spatial width  $\rho_i$  in the  $xy$ -plane, and duration  $t_i$ .

The cross correlation is given by Eq. (2.5) with the understanding that the relevant intensities are those in the plane of the GaAs surface at  $z = 0$ . Each pulse's local coordinates can be rotated into the wafer coordinate system to give the expression

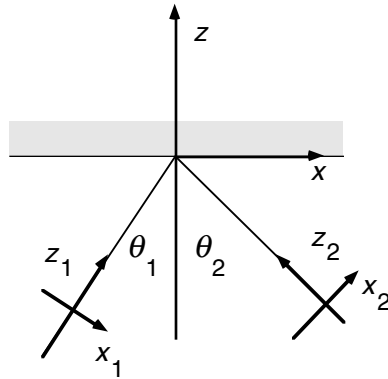


**Fig. 2.18** Geometry of reflection cross correlation between two beams.

$$\begin{aligned}
 I_{cc}(\tau) = & \int_{-\infty}^{\infty} \int_{-\infty}^{\infty} \int_{-\infty}^{\infty} dx dt dy \exp \left\{ - \left( \frac{x \cos \theta_1}{\rho_1} \right)^2 - \left( \frac{ct - x \sin \theta_1}{ct_1} \right)^2 \right\} \times \\
 & \exp \left\{ - \left( \frac{x \cos \theta_2}{\rho_2} \right)^2 - \left( \frac{ct - c\tau - x \sin \theta_2}{ct_2} \right)^2 - y^2 \left( \frac{1}{\rho_1^2} + \frac{1}{\rho_2^2} \right) \right\} . \quad (2.18)
 \end{aligned}$$

The  $y$ -integral has no  $\tau$ -dependence and can be ignored. The  $x$ - and  $t$ -integrals can be done by completing the square. The result is a Gaussian

$$I_{cc}(\tau) = k e^{-(\tau/\tau_p)^2} , \quad (2.19)$$

with  $\tau_p$  given by

$$\tau_p = \sqrt{t_1^2 + t_2^2} \left[ 1 + \frac{(\sin \theta_1 - \sin \theta_2)^2}{c^2(t_1^2 + t_2^2) \left( \frac{\cos^2 \theta_1}{\rho_1^2} + \frac{\cos^2 \theta_2}{\rho_2^2} \right)} \right]^{1/2} . \quad (2.20)$$

If the two pulses have the same temporal profile, as in an autocorrelation, this expression can be simplified to give

$$\tau_p = t_p \sqrt{2} \sqrt{1 + \left( \frac{T}{t_p} \right)^2} , \quad (2.21)$$

where

$$T = \frac{\rho_1 \rho_2 |\sin \theta_1 - \sin \theta_2|}{c \sqrt{2}} \frac{1}{\sqrt{(\rho_1 \cos \theta_2)^2 + (\rho_2 \cos \theta_1)^2}} . \quad (2.22)$$

The leading factor of  $t_p \sqrt{2}$  in Eq. (2.21) is the unbroadened autocorrelation width for Gaussian pulses. The remaining expression gives the relative increase in measured autocorrelation due to the angle between the beams. In this expression,  $T$  sets the scale for broadening effects: pulses of duration  $t_p$  of the same order as  $T$  or shorter are significantly broadened. Note that the broadening does not depend sim-

ply on the relative angle  $\theta_2 - \theta_1$ .

Equation (2.21) can be inverted to give the pulse duration in terms of the measured autocorrelation

$$t_p = \sqrt{\frac{\tau_p^2}{2} - T^2} . \quad (2.23)$$

The Gaussian radii of the pulses used in the experiment are  $40 \mu\text{m}$  for the pump beam incident along the normal and  $15 \mu\text{m}$  for the probe beam at  $45^\circ$ . Substituting this into Eq. (2.22) gives  $T = 31.2 \text{ fs}$ . The autocorrelation data are shown in Fig. 2.19. A Gaussian fit gives  $\tau_p = 148 \text{ fs}$ , which by Eq. (2.23) gives a pulse width of  $t_p = 100 \text{ fs}$  (165 fs FWHM). Substituting this value of  $t_p$  into the square root of Eq. (2.21) indicates that the angle broadening is slightly less than 5%.

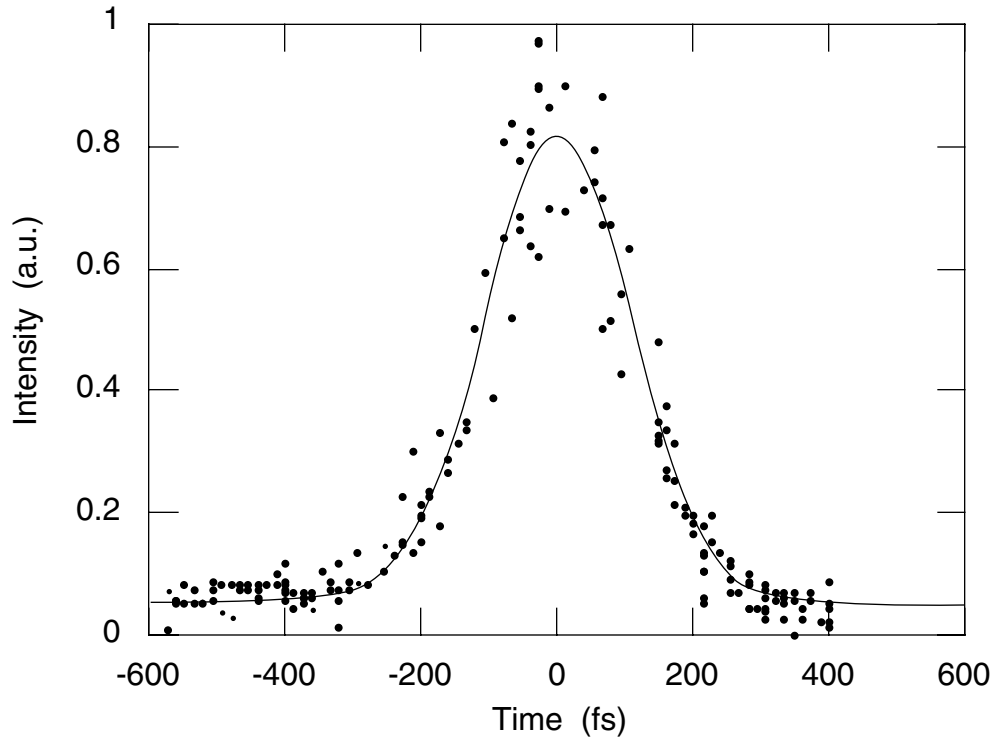


**Fig. 2.19** Autocorrelation of the amplified pulses. The line is a Gaussian fit giving an autocorrelation Gaussian time of 238 fs from which a pulse Gaussian time of 100 fs (165 fs FWHM) is inferred, when account is taken of  $\sim 5\%$  angle broadening.

## **2.5 Conclusion**

The amplified femtosecond dye laser system produces short optical pulses in the red portion of the visible spectrum at a repetition rate of 10 Hz. The pulses have an average energy of 1 mJ before compression; their spectrum and duration can be tuned somewhat by varying the dispersion compensation in the oscillator and in the final pulse compressor. In addition, a broadband continuum pulse can be created by self-phase modulation and self-focusing when a portion of the amplified beam is focused in a cell of water. From this continuum, a frequency-shifted probe can be selected with a filter and amplified, thereby significantly increasing the versatility of the laser system. The laser has been used in a reflectivity and reflection second-harmonic generation study of GaAs during femtosecond laser melting that is described in the following chapter.

# Chapter 3

## Femtosecond Laser Melting of GaAs

### **3.1 Introduction**

The study of the interaction of intense laser pulses with semiconductor surfaces intensified in the 1970s when it was discovered that such pulses could anneal crystals that had been damaged by ion bombardment. [von der Linde 1990] Two different theories were advanced to explain how the laser radiation could bring about the restoration of crystalline order in a damaged surface layer. The first is a thermal model in which the absorbed laser radiation is treated essentially as a source of heat to the crystal. For sufficiently intense radiation, the energy deposited in the material near the surface brings the crystal to the melting temperature and supplies the latent heat of melting, producing a layer of liquid with a thickness roughly equal to the absorption depth of the laser radiation. If this depth brings the liquid in contact with the undamaged crystal, then as it cools and resolidifies it could be expected to regrow epitaxially from the bulk phase.

The second model stresses the importance of the dense electron-hole plasma

created by the absorbed laser radiation. [Van Vechten 1979a, Van Vechten 1979b, Van Vechten 1981] As a high density of electrons is excited from the bonding states of the valence band to the anti-bonding states of the conduction band, estimated to be  $8 \times 10^{21} \text{ cm}^{-3}$  for silicon, the bond charges become so depleted that they are unable to stabilize the transverse acoustic phonon modes. [Van Vechten 1979a] This gives atoms and defects greater mobility. Crystalline order is reestablished as defects and dislocations diffuse to the surface. Energy relaxation from the hot plasma to the lattice is assumed to be slow, so that the lattice temperature rise would be slight on a time scale as long as tens of nanoseconds. [Van Vechten 1979a]

A number of experiments were performed in the early 1980s with nanosecond and picosecond pulses on silicon, germanium, and gallium arsenide to determine whether the laser-excited material melts. Stritzker, Pospieszczyk, and Tagle used a time-of-flight technique to measure the velocity distribution of evaporated Si atoms from a surface irradiated with 50-ns pulses. [Stritzker 1981] It was found that the evaporated Si atoms are well characterized by a Maxwellian distribution, indicating that the surface is molten and can be heated at least a thousand degrees above the melting temperature.

Pump-probe experiments were used to study the time-resolved optical response of the laser-excited material. Reflectivity measurements showed the existence of a high-reflectivity phase during and after excitation with nanosecond and picosecond pulses. The liquid phase of most semiconductors is metallic and has higher reflectivity than either the crystalline or amorphous phase. Thus, the optical experiments supported the existence of a molten phase, in agreement with the thermal model.<sup>1</sup> The picosecond measurements also indicated that the excess energy of photoexcited electrons is converted to lattice vibrations on a time scale shorter than 10 ps.

In GaAs, the dominant mechanism for energy relaxation from photoexcited car-

riers to the lattice is the emission of longitudinal optical (LO) phonons. [Wood 1984, van Driel 1987] Hot electrons cascade down the sides of the zone-center  $\Gamma$  valley by emitting LO phonons of the appropriate momentum, eventually yielding a cooled sea of electrons that fills the bottom of the  $\Gamma$  valley. Kash, Tsang, and Hvam measured the rate of LO phonon emission in GaAs using a time-resolved spontaneous Raman technique. For electron densities below  $10^{18} \text{ cm}^{-3}$ , the emission time was measured to be approximately 165 fs. [Kash 1985] Since 2-eV photons excite electrons from the light- and heavy-hole bands to states about 500 meV above the conduction band minimum, electrons emit roughly fifteen 30-meV LO phonons in relaxing to the band edge. Thus a photoexcited electron sheds its excess energy to lattice vibrations in  $\sim 3$  ps. At higher electron densities the coupling between long-wavelength optical phonons and charge carriers is reduced by screening. [Yoffa 1981] This reduces the intravalley phonon emission rate.

Auger recombination provides a second mechanism for energy relaxation from carriers to the lattice. In an Auger process an electron and hole recombine, giving their recombination energy to a second electron or hole. While decreasing the density of free carriers on a time scale of a few picoseconds, Auger recombination does not cause lattice heating directly because the recombination energy remains in the carrier system. However, the hot carrier rapidly emits phonons, thereby completing the relaxation of laser energy to the lattice. The most detailed version of the thermal model takes into account the diffusion of carriers and heat into the bulk, carrier recombination, changes in the reflectivity and bulk thermodynamic properties as functions of temperature. and the temperature difference between the hot electrons

---

<sup>1</sup> A dense electron-hole plasma could also cause high reflectivity. However, Blinov *et al.* [Blinov 1967] found that their data on the absorption of long-wavelength light during irradiation of GaAs and Si with a ruby laser was more consistent with the existence of a molten layer. See also Wood 1981.

and the lattice. [van Driel 1987] It is successful in accounting for the optical reflectivity data in a variety of picosecond and nanosecond experiments on Si, Ge, and GaAs.

Intense femtosecond laser pulses, however, deposit energy in the carrier system on a time scale short compared to the energy relaxation time of phonon emission and Auger recombination. Such pulses can excite a significant fraction of bonding valence electrons to anti-bonding conduction states before phonon emission can heat the vibrational modes appreciably. Such a level of excitation may severely weaken the restoring forces on ions in transverse acoustic modes, allowing the lattice to disorder rapidly even at room temperature thermal velocities. [Van Vechten 1979a] The first laser melting experiments using femtosecond pulses were reflectivity and second-harmonic studies of silicon. [Shank 1983b, Shank 1983a] For the first time, the high-reflectivity phase appeared after, instead of during, the pump pulse, which had a duration of 90 fs. The second-harmonic generation experiment was refined by Tom *et al.*, who observed a 150-fs decay time for the second harmonic in crystalline silicon after a 100-fs excitation pulse. [Tom 1988] From this decay a loss of cubic order in the electronic system was inferred.

We<sup>1</sup> have performed femtosecond pump–probe experiments on GaAs (100) and (110) surfaces that show a 100-fs decay time for the second-harmonic intensity and a 200-fs rise time for the reflectivity. Since crystalline GaAs lacks a center of inversion, second-harmonic generation in the bulk of the crystal is dipole-allowed. It arises from the asymmetry in the bond between adjacent gallium and arsenic atoms. [Shen 1984] Conduction electrons are nearly free and do not contribute significantly to the second-order nonlinear susceptibility  $\chi^{(2)}$ , which governs second-

---

<sup>1</sup> The experiments were performed by Yakir Siegal, Juen-Kai Wang, and Peter Saeta.

ond-harmonic signal that we detect monitors the  $\bar{4}3m$  symmetry of the valence electron state in roughly the upper 90 atomic layers, which is the absorption depth of light at the second-harmonic frequency in GaAs. Second-harmonic light generated deeper in the sample by the probe beam, which has a much longer absorption depth of 230 nm, is absorbed before reaching the surface.

Because  $\chi^{(2)}$  is so large in bulk GaAs, surface second-harmonic generation can be neglected in these experiments. Surface second-harmonic generation arises from the broken symmetry at the interface. In materials with a center of inversion, surface second-harmonic generation may be as large or even larger than second-harmonic generation from higher-order processes in the bulk. [Shen 1984] This property has opened the door to second-harmonic and sum-frequency experiments on adsorbed monolayers on semiconductor surfaces, in which the polarization dependence of the nonlinear optical signal reveals information about the symmetries of the monolayer. In the current experiments, surface second-harmonic generation is at least three orders of magnitude weaker than the bulk signal and can be neglected.

Above a fluence threshold of approximately  $0.1 \text{ J/cm}^2$ , the reflected second-harmonic intensity is observed to drop to zero and the reflectivity to rise to a steady high value. The 100-fs drop in reflection second harmonic implies a transformation to a centrosymmetric electronic state in at least the upper 90 atomic layers within 100 fs. The reflectivity attains a value characteristic of a metallic molten phase within 0.5 ps. In this time, very little heat is transferred to the lattice by phonon emission. The high level of electronic excitation appears to drive the cold lattice to disorder.

After several picoseconds, the reflectivity is observed to drop and by 200 ps following excitation, it falls considerably below the reflectivity of unpumped crystalline material. Many workers have observed this sort of reflectivity drop in laser melting experiments, [Downer 1985, Malvezzi 1986] although questions remain as to

its cause. Various explanations involve thermal gradients, scattering by inhomogeneities in the plane of the surface, scattering and absorption by ablated material, and roughening of the surface. We have observed a rise in scattering of the probe light away from the specular direction 200 ps after excitation. We have also measured the depth of the pits created by laser excitation and found a very weak dependence on incident fluence. Furthermore, the amount of material ejected from the surface is sufficient to account for the reflectivity drop and scattering rise provided much of it takes the form of droplets of sufficient size. Support for this interpretation is further provided by electron micrographs of the laser-generated pits, which reveal a layer of solidified droplets 100–200 nm in diameter.

## **3.2 Laser Setup**

In order to achieve spatially uniform pumping over the probed area, it is necessary to produce high-energy femtosecond laser pulses with smooth spatial profile. Our laser system consists of a colliding-pulse mode-locked (CPM) laser oscillator, a five-stage dye amplifier, and a grating-pair compressor which generates a 10-Hz train of 100-fs pulses having an average energy greater than 1 mJ/pulse. The 623-nm wavelength pulses have a nearly uniform (“top hat”) spatial profile that focuses to a spot of diffraction-limited extent.

The CPM is a standard 7-mirror cavity [Fork 1984] pumped by an argon ion laser (Coherent Innova 200-10) operating in multiline mode at a typical power of 2.5 W. It is tuned to produce a 125-MHz train of pulses of 100-fs (FWHM) duration. The amplifier employs 5 transverse-pumped prism dye cells [Bethune 1981] (bore diameters 1, 3, 3, 6, and 10 mm; lengths 20, 25, 38, 38, and 70 mm) to provide nearly spatially uniform gain. The cells are pumped by a frequency-doubled Nd:YAG laser (Continuum 200-10) whose 300 mJ/pulse is distributed to the cells as 6, 15, 22, 45,

225 mJ/pulse, respectively. Sulforhodamine 640 in a 2% aqueous solution of ammonyx LO is used in the first cell; Kiton Red 620 in an identical solution is used in the rest of the cells. The CPM pulses enter the amplifier after passing through an aperture which blocks all but the (approximately uniform) central third of the beam to yield a top hat profile. A pair of convex lenses, the first immediately behind the aperture, the second at sufficient distance after the focus of the first to recollimate the beam, produces a relayed image of the aperture near the exit face of the first amplifier cell. Subsequent lens pairs expand the beam and relay the image of the aperture to the successive dye cells. Care has been taken to choose achromatic lenses where necessary to minimize spherical aberration. In this way diffraction distortion of the amplified beam is minimized.

The chirp impressed on the pulses by normal dispersion in the dye solutions of the gain cells and glass of the optics is compensated by a matched pair of holographic gratings. The slant separation of the gratings, and hence the dispersion compensation, is adjusted to minimize the intensity autocorrelation of the pulses at the sample position. A Gaussian fit yields 100 fs for the  $1/e$ -time of the pulses (160 fs FWHM).

### **3.3 Experimental**

Figure 3.1 illustrates the experimental setup. The linearly polarized pulses are divided into pump and probe beams with an energy contrast of 300:1. The pump strikes the sample at normal incidence, while the probe enters at  $45^\circ$ . An optical delay line on the pump beam path permits the probe pulse to be variably delayed with respect to the pump pulse. The probe pulse is focused to probe the central 10% of the pumped area. The large angle between the pump and probe beams isolates the probe detectors from stray pump light. Two different crystallographic ori-

entations and polarization configurations were used. In the first experiment the sample was a (100) GaAs surface in air, oriented so that the [010] axis in the plane of the surface was vertical, as shown in Fig. 3.2. The probe beam was *p*-polarized (electric field in the plane of incidence); the pump was orthogonally polarized so that its electric field was aligned with the [010] crystal axis and therefore could not produce second harmonic. In the second experiment the sample was a (110) GaAs surface in air, and the polarization of each beam was rotated 90° with respect to the first configuration to give an *s*-polarized probe and a pump electric field aligned with the in-plane [001] axis. Both samples were semi-insulating GaAs (Cr doped,  $\rho > 7 \times 10^7 \Omega \text{ cm}$ ), etched with HF prior to mounting on an *xy*-stage. The sample was translated between shots in a raster pattern to avoid cumulative damage effects.

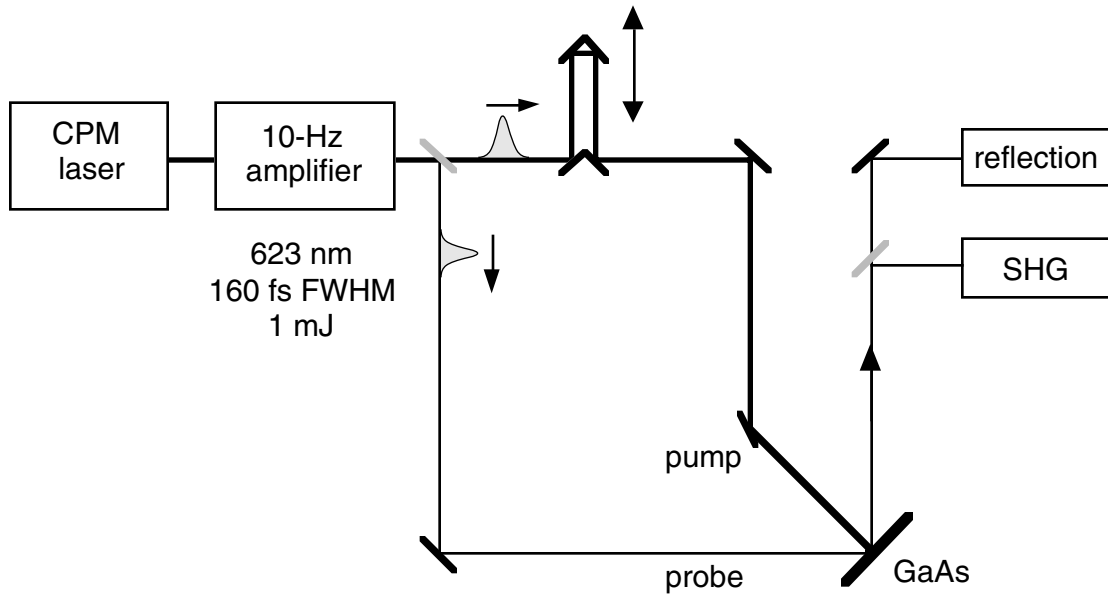


**Fig. 3.1** Experimental setup for studying femtosecond laser melting of GaAs. A beam splitter divides the 160-fs pulse into pump and probe pulses with an energy contrast of 300:1. The pump pulse strikes the sample at normal incidence after a variable delay. The probe pulse is incident at 45° and focused to probe the central 10% of the pumped area. A chromatic beam splitter directs the reflected second-harmonic light to a photomultiplier tube, transmitting the reflected red light which is detected with a phototube.

The origin of time was determined by measuring the intensity autocorrelation of the attenuated pump and probe beams in reflection from the GaAs sample. Due to the large angle between the beams, the autocorrelation Gaussian width of 160 fs was broadened by  $\sim 5\%$  with respect to a small-angle autocorrelation. This small decrease in temporal resolution had a negligible effect on the experiments.

For each laser shot a computer records the incident pump and probe energy, as well as the reflected fundamental and second-harmonic energy. Phototubes with 10-nm bandpass interference filters centered at 620 nm are used to measure signals at the fundamental; a photomultiplier tube behind a 310-nm interference filter detects the second-harmonic radiation. The transient signals are integrated, digitized, aver-

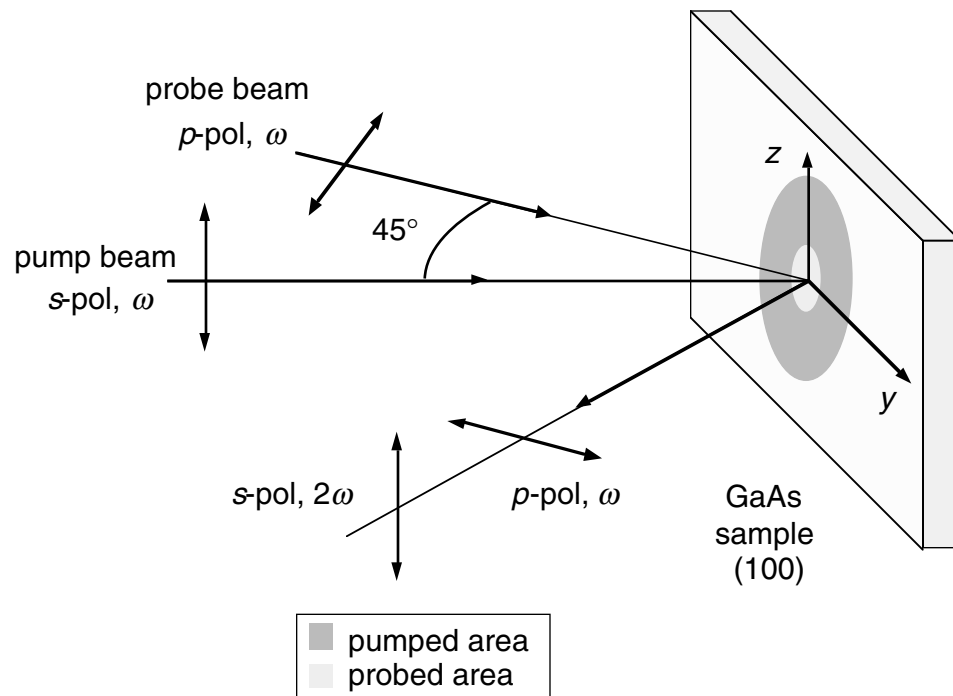


**Fig. 3.2** Detail of the (100) probing geometry. The pump beam enters along the sample normal, which is the crystallographic  $x$  or  $[100]$  axis. Its electric field is aligned with crystallographic  $z$  to suppress second-harmonic generation. The probe beam is polarized in the plane of incidence and has electric field in the  $xy$ -plane.

aged, and normalized relative to the reflectivity and second-harmonic intensities of unpumped crystalline material. Data are collected over a range of incident fluence at fixed time delays. At each delay the signals are checked with the pump blocked to ensure that the reflectivity is independent of probe intensity and that the second-harmonic intensity depends quadratically on the incident probe intensity.

All reflectivity measurements are relative. To deduce absolute values of reflectivity, the low-intensity reflectivities at  $0^\circ$  and  $45^\circ$  incidence were calculated from the Fresnel formulas based on the published value of the refractive index of crystalline GaAs at  $\lambda = 623$  nm,  $n = 3.873 + 0.207i$ . [Palik 1985] For the pump beam at normal incidence, this gives a reflectivity of  $R_0^\perp = 0.349$ . For the  $45^\circ$  angle of incidence of the probe beam, the reflectivities are  $R_0^p = 0.224$  and  $R_0^s = 0.473$ .

### 3.4 Results from a (100) Surface

The reflectivity and second-harmonic response of the (100) surface measured with a *p*-polarized probe is summarized in Figs. 3.3 and 3.4, which displays these signals as functions of fluence and time over the range  $-0.5$  to  $2.5$  ps. The fluence scale for these data is in units of the threshold fluence for decay of the second-harmonic signal at long times.<sup>1</sup> The reflected second-harmonic intensity is seen to drop rapidly to zero for fluences above the threshold. For the same fluence range, the reflectivity rises to a steady value that is slightly more than twice the original reflectivity. In absolute terms, the high reflectivity value is  $R_{hr}^p = 0.47$ .

Below the threshold fluence the opposite behavior is observed: the reflectivity

---

<sup>1</sup> The results for the (110) surface, which were performed with a fluence calibration, indicate that the threshold fluence is  $0.1$  J/cm<sup>2</sup>.

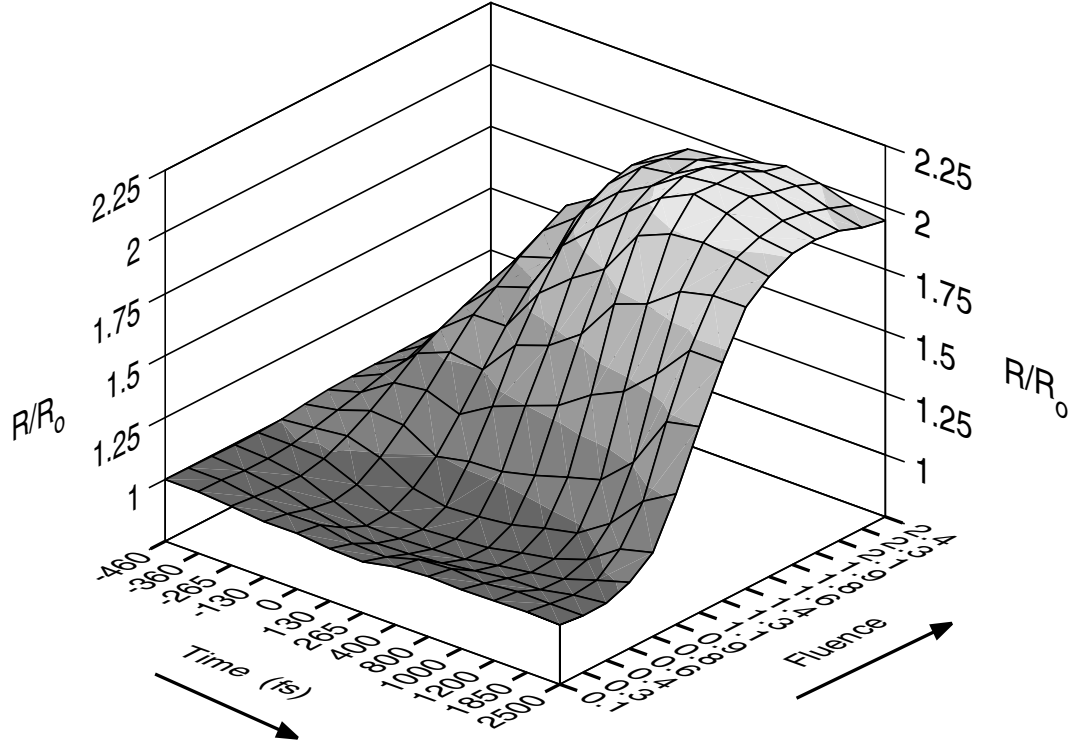


**Fig. 3.3** Relative  $p$ -polarized reflectivity from a (100) GaAs surface as a function of fluence and probe delay time. The probe beam is incident at  $45^\circ$ . The fluence axis is normalized relative to the threshold fluence, as determined from the loss of second-harmonic generation. Note the dip in reflectivity near the origin of time for fluences below threshold.

dense free-carrier plasma created by the excitation pulse. The dielectric response of such a plasma can be well approximated by a Drude model. For a single-component plasma of particles with charge  $q_j$ , mass  $m_j$ , and density  $N_j$ , the Drude expression for the dielectric constant (in Gaussian units) at frequency  $\omega$  is

$$\epsilon_{\text{plasma}}(\omega) = -\frac{4\pi N_j q_j^2}{m_j \omega(\omega + i\gamma_j)} = \frac{-\omega_p^2}{\omega^2 + \gamma_j^2} \left(1 - \frac{i\gamma_j}{\omega}\right) \quad (3.1)$$

In this expression,  $\gamma_j$  is the collision frequency that gives rise to the resistive loss of the plasma, and  $\omega_p = \sqrt{4\pi N_j q_j^2 / m_j}$  is the plasma frequency. For the photoexcited GaAs electron-hole plasma, electrons in the  $\Gamma$  and L valleys and holes at the top of

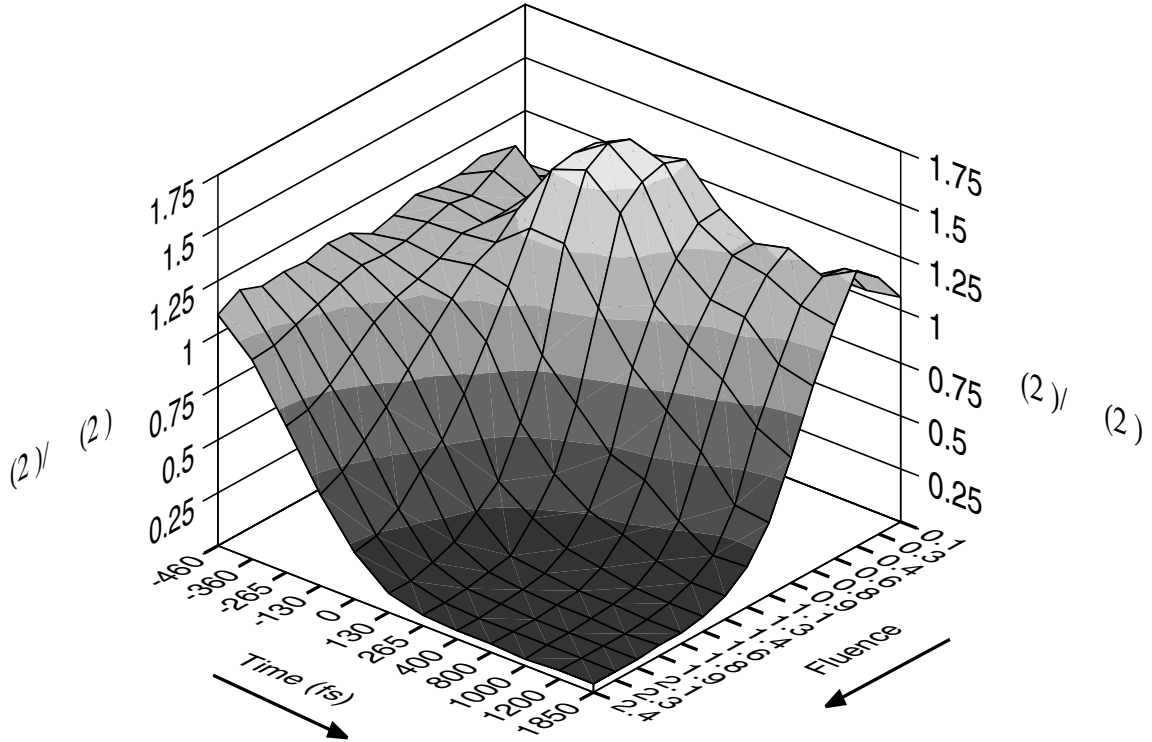


**Fig. 3.4** Relative second-harmonic intensity from a (100) GaAs surface as a function of fluence and probe delay time. The probe is  $p$ -polarized and incident at  $45^\circ$ . Note the rise in second harmonic near the origin of time for fluences below threshold.

the valence band make contributions of the form (3.1). Except for small thermalized carrier densities, it is difficult to know the proper effective mass to use in calculating the plasma frequency. The collision frequency poses a similar problem. Hence,  $\epsilon_{\text{plasma}}$  cannot be calculated easily from the incident fluence.

Nonetheless it is clear from the form of the Drude expression that the plasma reduces the real part of the dielectric constant, which may be expressed as

$$\epsilon = \epsilon_b - |\epsilon_{\text{plasma}}| = n^2, \quad (3.2)$$

where  $\epsilon_b = 1 + 4\pi\chi_e$  is the dielectric constant of the bound electrons. For small changes to the dielectric constant caused by the plasma, the reflectivity is sensitive only to the real part of the plasma dielectric response. The plasma term decreases

the real part of both  $\epsilon$  and  $n$ . This in turn produces a decrease in the reflectivity. A straightforward calculation shows that a drop in the real part of the index to 3.5 can account for the minimum observed relative reflectivity of 0.83.

A change in the refractive index affects the detected second-harmonic signal in two ways. First, lowered reflectivity implies increased transmission of the probe light into the material, where it drives the second-harmonic polarization. Since the energy in the second-harmonic beam depends quadratically on the probe intensity inside the material, the relative change in the observed second-harmonic signal produced by a change in Fresnel factor can be expressed as  $[(1 - R)/(1 - R_0)]^2$ .

Second, a decrease in the real part of the refractive index increases the angle of refraction. This causes a rotation of the electric field direction away from the surface for a  $p$ -polarized beam, changing the components of the electric field along the crystal  $x$  and  $y$  directions. The effect is illustrated in Fig. 3.5. In crystals with  $\bar{4}3m$  symmetry, such as GaAs, 21 of the 27 components of  $\chi^{(2)}$  vanish; the remaining 6 are all equal and proportional to  $xyz$ . [Shen 1984] For constant  $|\mathbf{E}|$  in the  $xy$ -plane,  $E_z(2\omega) = \chi_{xyz}^{(2)} |\mathbf{E}|^2 \sin\theta_r \cos\theta_r$ . Since the detected signal depends quadratically on  $E$ , the polarization rotation effect produces a relative increase of  $[\sin(2\theta_r)/\sin(2\theta_{r,0})]^2$ . This factor is 2–3 times larger than the Fresnel factor for small changes in  $n$ . The two factors and their combined strength are plotted in Fig. 3.6.

Over the region of fluence and time where the reflectivity is reduced, the combined corrections account for slightly more than half the observed increase in detected second harmonic. Although less than perfect agreement, it is clear that the polarization rotation effect plays an important role in producing a rise in second-harmonic intensity when the probe is  $p$ -polarized. This conclusion is also supported by the data taken on a (110) surface presented in the following section.

### 3.5 Results from a (110) Surface

The polarization rotation effect can be eliminated by using an *s*-polarized probe on a (110) surface. By rotating by  $90^\circ$  the polarization of both the pump and probe beams, and by orientating the wafer so that the [001] crystal axis in the plane of the wafer is aligned with the pump electric field, both second-harmonic generation by the pump and polarization rotation of the probe can be suppressed (see Fig. 3.7). The results are summarized in the three-dimensional plots of Figs. 3.8 and 3.9. As before, under the fluence threshold of  $0.1 \text{ J/cm}^2$  the reflectivity dips below the unpumped crystalline value. However, there is no measurable rise in second-harmonic intensity for the range of times and fluences for which the reflectivity is

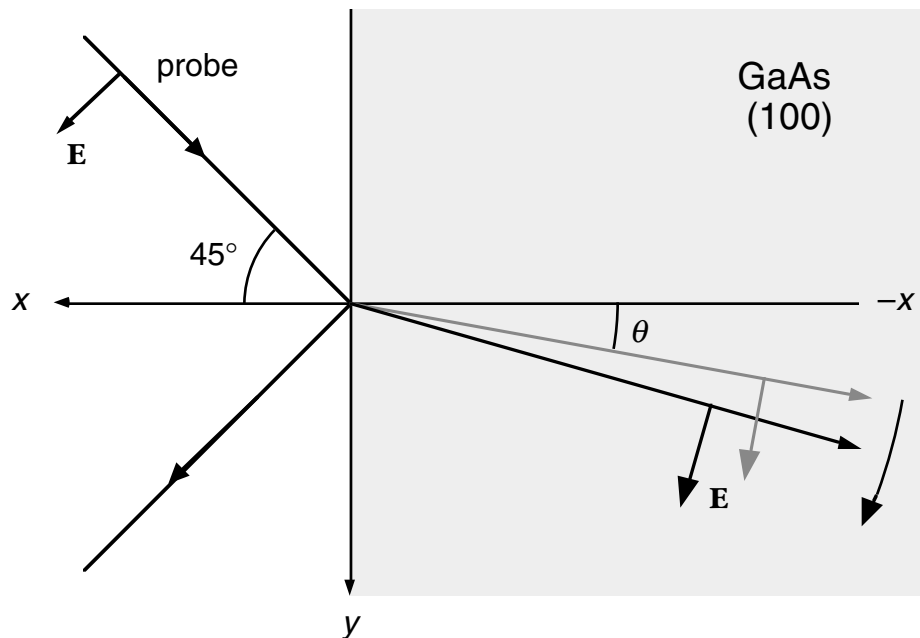


**Fig. 3.5** Polarization rotation effect. By reducing the real part of the index of refraction, the free-carrier plasma causes the refracted beam to swing away from  $x$  axis. This rotates the electric field of the transmitted beam away from the  $y$  axis, leading to more efficient production of second harmonic.

reduced. The data show that indeed the polarization rotation effect is largely responsible for the increase observed with *p*-polarization.

Figure 3.10 shows the normalized reflectivity and second-harmonic signals as functions of incident pump fluence at 120-fs delay. The open squares are the second-harmonic data corrected for changes in the Fresnel factor, as deduced from the reflectivity data. The data display the same trends as were seen in the data taken on the (100) surface, with the exception of the below-threshold rise in second harmonic. At a threshold of  $0.1 \text{ J/cm}^2$  the second-harmonic intensity begins to drop. For fluences above  $0.2 \text{ J/cm}^2$  it effectively vanishes, even at this short time delay. As

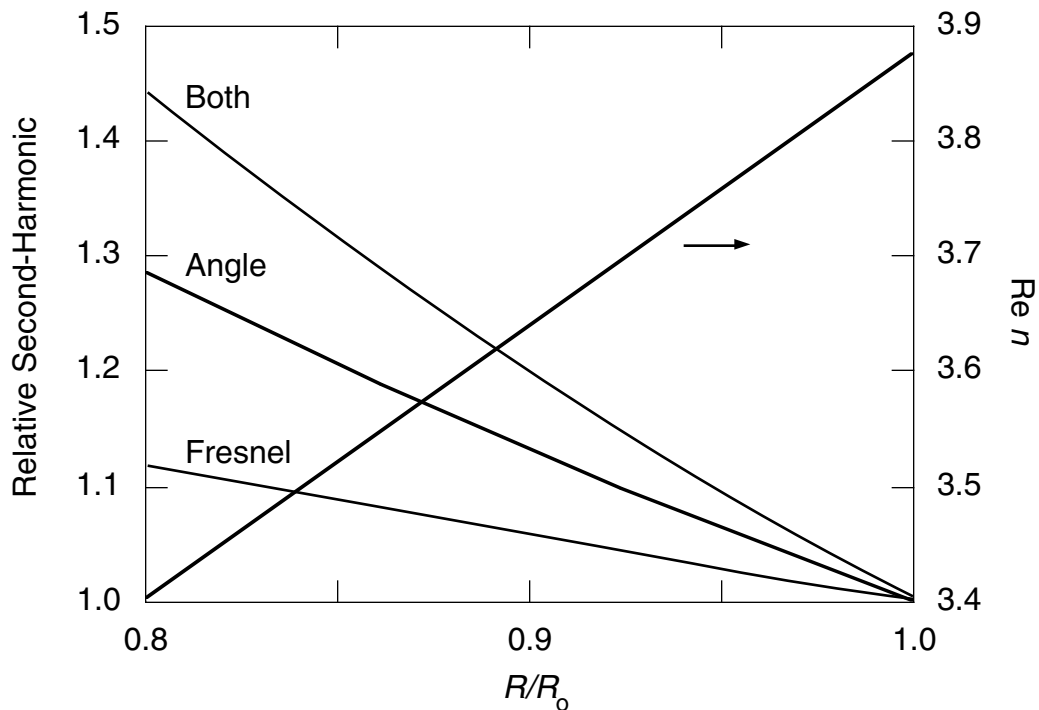


**Fig. 3.6** Factors affecting the second-harmonic intensity from a (100) GaAs surface probed at  $45^\circ$  incidence. The Fresnel factor expresses the change in the light intensity that is transmitted through the interface. The angle factor expresses the change in the direction of polarization of the probe beam inside the material caused by the photoexcited carrier plasma. The combination of these two factors is shown in the upper curve. The line of positive slope shows the index as a function of the relative reflectivity.

is clear from the Fresnel-corrected data, the threshold and high-fluence drop in second-harmonic intensity are not produced by changes in reflectivity. At the highest fluence, the reflectivity rise approaches 44%, corresponding to an absolute reflectivity of 0.68.

In Fig. 3.11 the relative second-harmonic and reflectivity signals are shown as functions of time for a fluence of  $0.33 \text{ J/cm}^2$ . The data are fitted with simple exponential functions of the form

$$\Delta A(t) = (A_f - A_i)(1 - e^{-(t-t_0)/\tau_A}) \quad , \quad (3.3)$$

where  $A_i$  and  $A_f$  represent the initial and final values of reflectivity or second-harmonic intensity, and  $\tau_A$  is the  $1/e$  response time. The fits give response times of

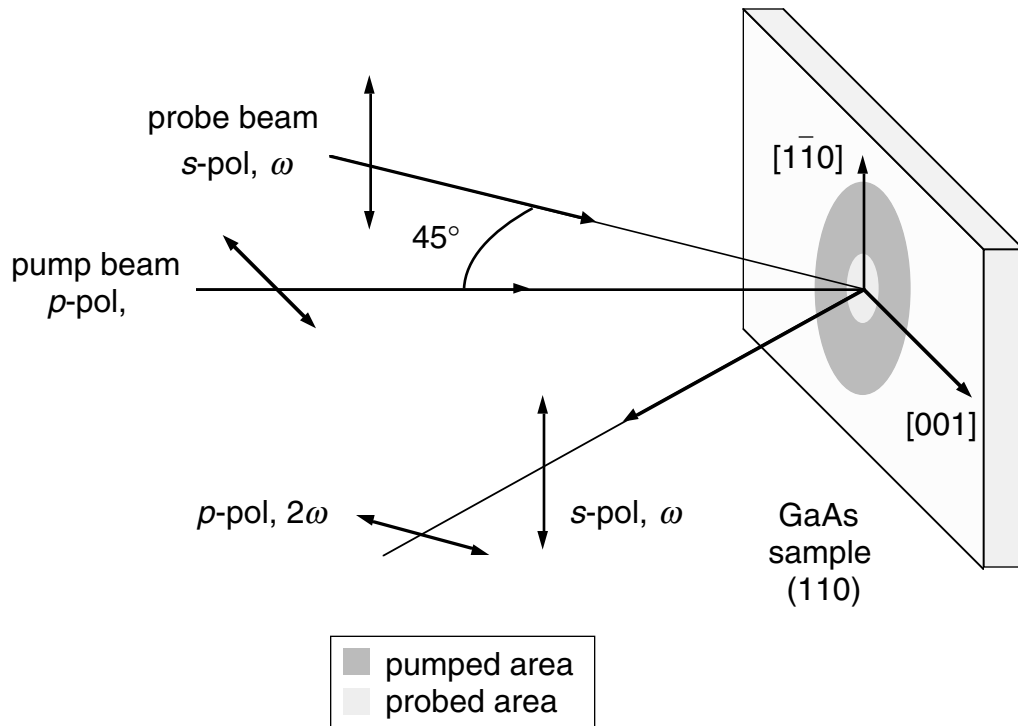


**Fig. 3.7** Detail of the (110) probing geometry. The pump beam is horizontally polarized and incident along the  $[1\bar{1}0]$  direction. The crystal is oriented to align the  $[001]$  axis with the pump electric field to suppress second-harmonic generation. The probe beam is s-polarized and enters at  $45^\circ$ . The probe electric field is aligned with the  $[1\bar{1}0]$  direction.

90 fs for the decay in second-harmonic and 170 fs for the rise in reflectivity. Similar fits for the fluence range 0.15 to 0.37 J/cm<sup>2</sup> are summarized in Fig. 3.12, which displays response times as functions of fluence. Above approximately 0.15 J/cm<sup>2</sup>, the second-harmonic decay time is constant at 100 fs. Similarly, above 0.25 J/cm<sup>2</sup> the reflectivity rise time is constant at 200 fs.<sup>1</sup>

Equation (3.3) does not account for the broadening of the measured response time caused by the finite duration of the pump and probe pulses. Particularly for the second-harmonic response time, which is comparable to the pulse duration, the convolution of the material response with the pulse duration tends to broaden the

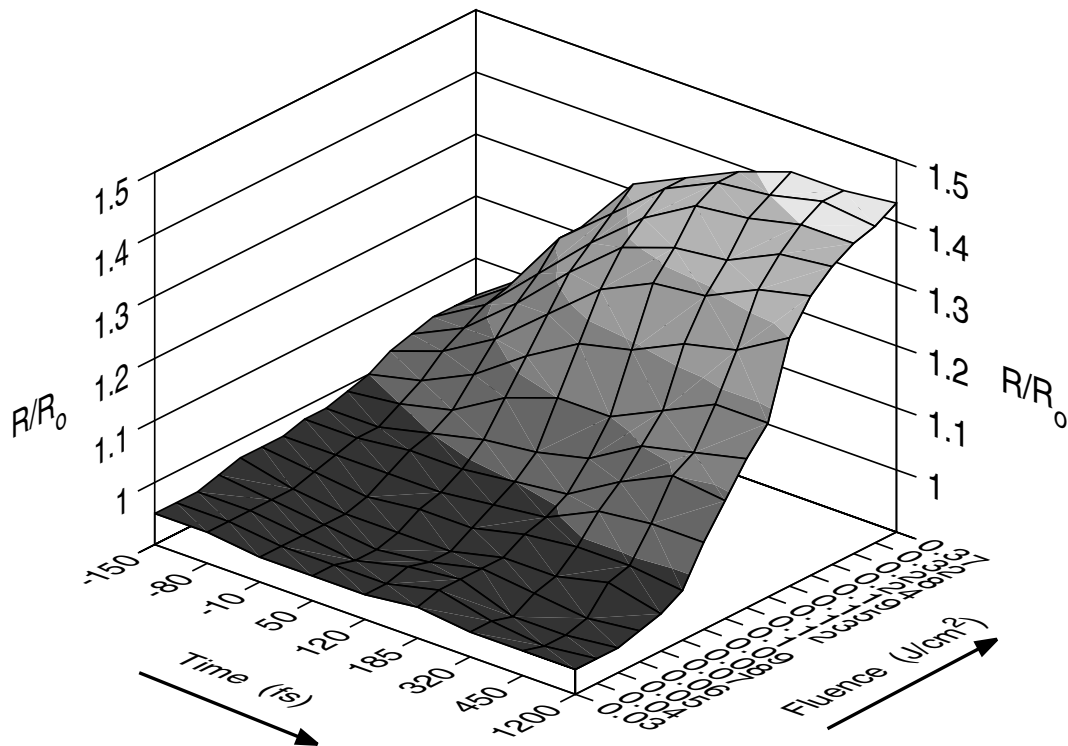


**Fig. 3.8** Relative s-polarized reflectivity from a (110) GaAs surface as a function of fluence and probe delay time. The probe beam is incident at 45°.

<sup>1</sup> There is insufficient data near  $t=0$  to perform similar fits to the data from a (100) surface.

measured response. In Fig. 3.13 the data at fluences of 0.33 and 0.37 J/cm<sup>2</sup> are shown with curves for different exponential response times convolved with the pump-probe cross correlation. The initial and final values of the second-harmonic intensity are assumed to be 1 and 0. From the curves it appears that the second-harmonic response time is about 50 fs, which is half the value obtained from the simple exponential fit.

### 3.6 Discussion of Short Time Results

The detected second-harmonic signal depends on both the linear and the non-linear optical response of the excited GaAs. Photoexcitation modifies the linear

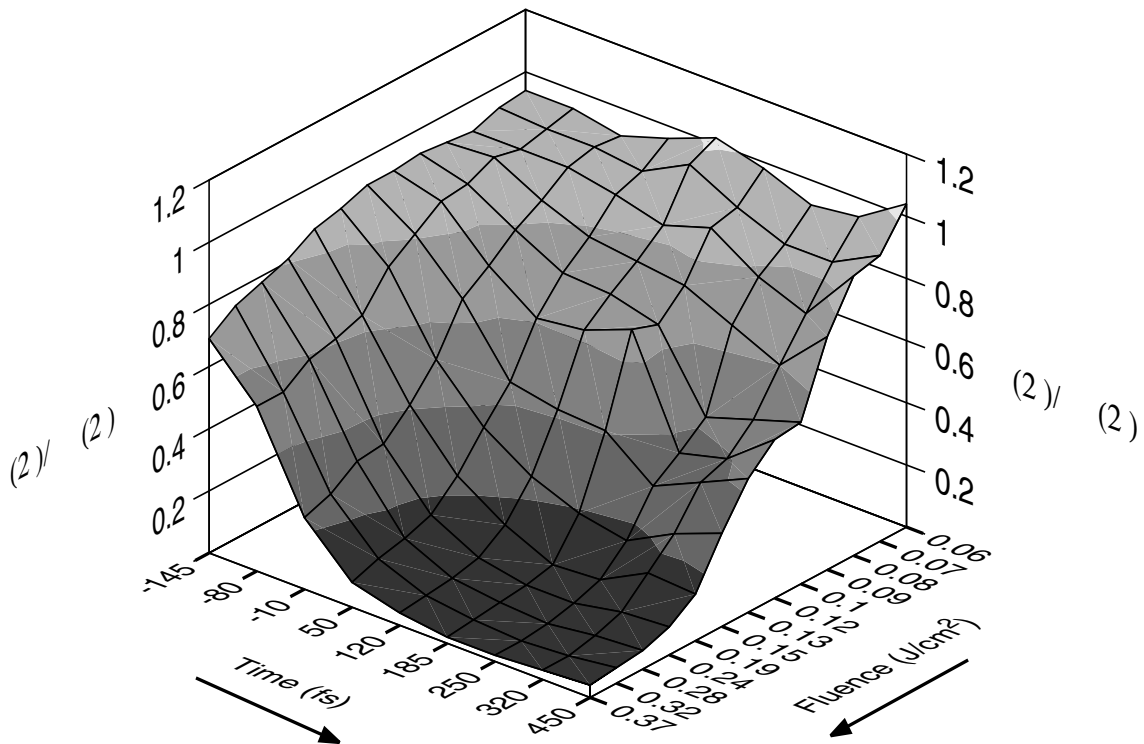


**Fig. 3.9** Relative second-harmonic intensity from a (110) GaAs surface as a function of fluence and probe delay time. The probe is s-polarized and incident at 45°.

response of the crystal by creating a dense electron-hole plasma which adds a free-carrier component to the dielectric constant. As we have seen, this can change the Fresnel factor for the reflection loss of probe intensity at the air-wafer interface. Furthermore, depopulation of the valence states may modify the absorption of light at the pump/probe wavelength. If these changes in the linear response were sufficient to quench the second-harmonic signal, then no change in the nonlinear response, and therefore no change in the electronic symmetry, can be inferred. On the other hand, if the linear effects cannot account for the observed drop, then the second order susceptibility  $\chi^{(2)}$  must undergo a pump-induced decrease.

A drop in  $\chi^{(2)}$  can be caused by two effects. First, depopulation of valence

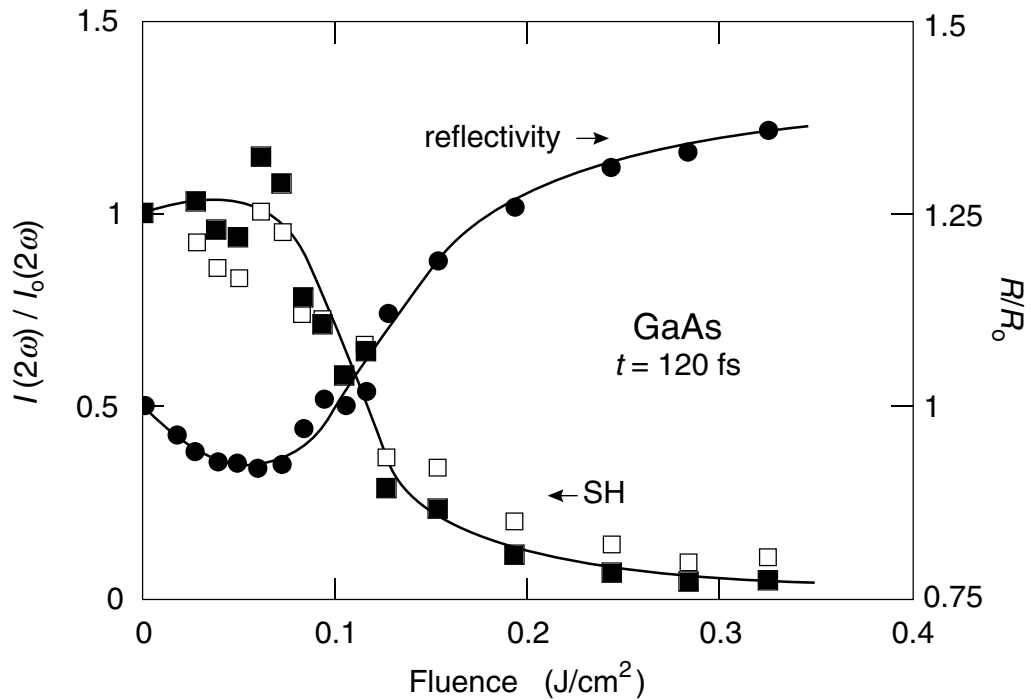


**Fig. 3.10** Fluence dependence of the relative reflected second-harmonic intensity (■) and reflectivity (●) of a (110) GaAs surface. The data were taken at 120-fs delay with 100-fs pulses of 620-nm wavelength at an incidence angle of 45°. The open squares are the second-harmonic data divided by  $[(1-R)/(1-R_0)]^2$  to correct for changes in reflectivity.

states may lower  $\chi^{(2)}$  by removing electrons from the states responsible for the strong dipole signal. Second, a change in the symmetry of the electronic state to a centrosymmetric configuration would cause  $\chi^{(2)}$  to vanish in the electric dipole approximation. [Shen 1984] As will be shown below, the linear changes cannot account for the vanishing of the second harmonic. Consequently, we infer that above a threshold of roughly  $0.1 \text{ J/cm}^2$  the electronic system undergoes a rapid phase transformation to a centrosymmetric, and probably isotropic, state within 100 fs. In less than 0.5 ps, this state exhibits the high metallic reflectivity of molten GaAs, which implies a level of ionization far above that accounted for by linear absorption.

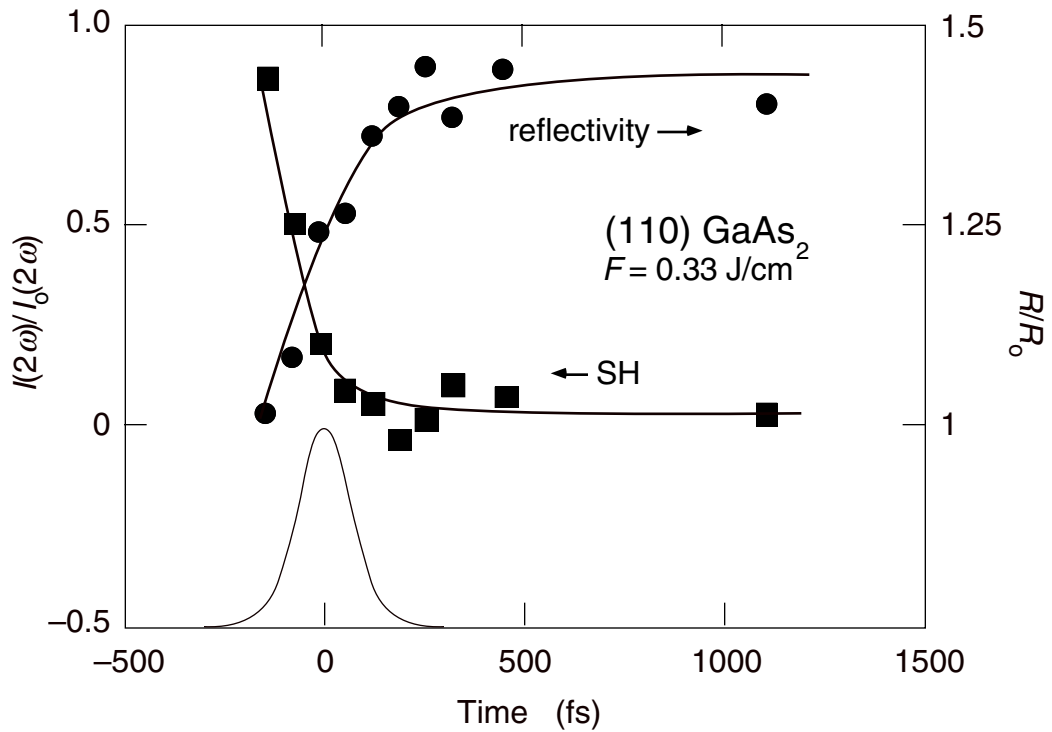


**Fig. 3.11** Time dependence of the relative second-harmonic intensity (■) and reflectivity (●) signals at a fluence of  $0.33 \text{ J/cm}^2$ . The curves are fits to exponentials yielding  $1/e$  times of 90 fs for the second-harmonic decay and 170 fs for the reflectivity rise. The peak at  $t = 0$  shows the duration of the laser pulse.

Linear absorption of 2.0-eV photons from the pump beam excites electrons from the heavy-hole, light-hole, and split-off valence bands to conduction band near the zone center, as indicated in Fig. 3.14. These interband transitions are the dominant absorption mechanism of pump light, provided the field intensity inside the material is not high enough to produce dielectric breakdown. At the upper end of the measured fluence range, the pump field intensity is roughly  $0.6 \text{ V/\AA}$ , which is insufficient to cause breakdown. Thus, interband transitions dominate the absorption.

In the limit of low intensity, a short pulse excites quasi-monoenergetic distributions of electrons at three distinct energies in the  $\Gamma$  valley of the conduction band, leaving corresponding distributions of holes in the light hole, heavy hole, and split-off valence bands. The electrons from the light and heavy-hole bands, which

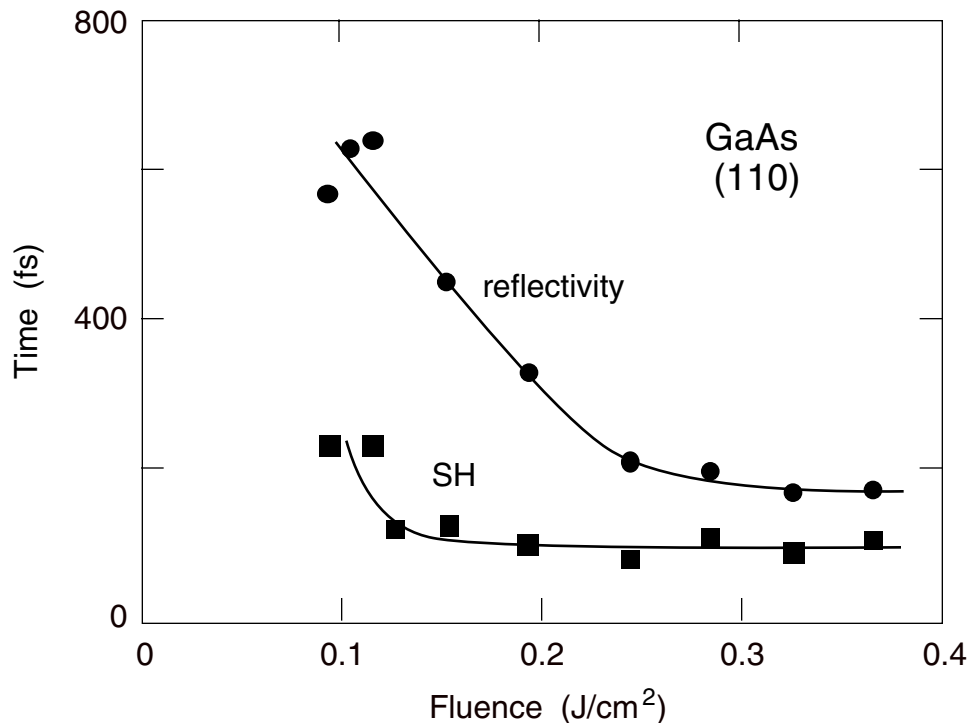


**Fig. 3.12** Fluence dependence of the  $1/e$  response time of second-harmonic decay (■) and reflectivity rise (●). Each data point corresponds to a fit to a full time trace, as in Fig. 3.11.

together constitute roughly 80% of the conduction electrons, [Lin 1988] are injected with  $\sim 500$  meV of kinetic energy above the bottom of the  $\Gamma$  valley. This places them above the minimum of the L valley and roughly even with the X valley. Principally through electron-electron and hole-hole scattering, these narrow distributions broaden substantially in a few femtoseconds. [Yoffa 1980, Shah 1987, Knox 1988] Because of their low momentum transfer, electron-electron collisions in the  $\Gamma$  valley cannot produce scattering into the L and X valleys. However, electrons at energies within the optical phonon energy ( $\sim 30$  meV) of the minimum of the respective satellite valleys can scatter to them by absorbing a high-momentum phonon, and those at energies exceeding the valley minimum by the optical phonon energy can scatter by either phonon emission and absorption.

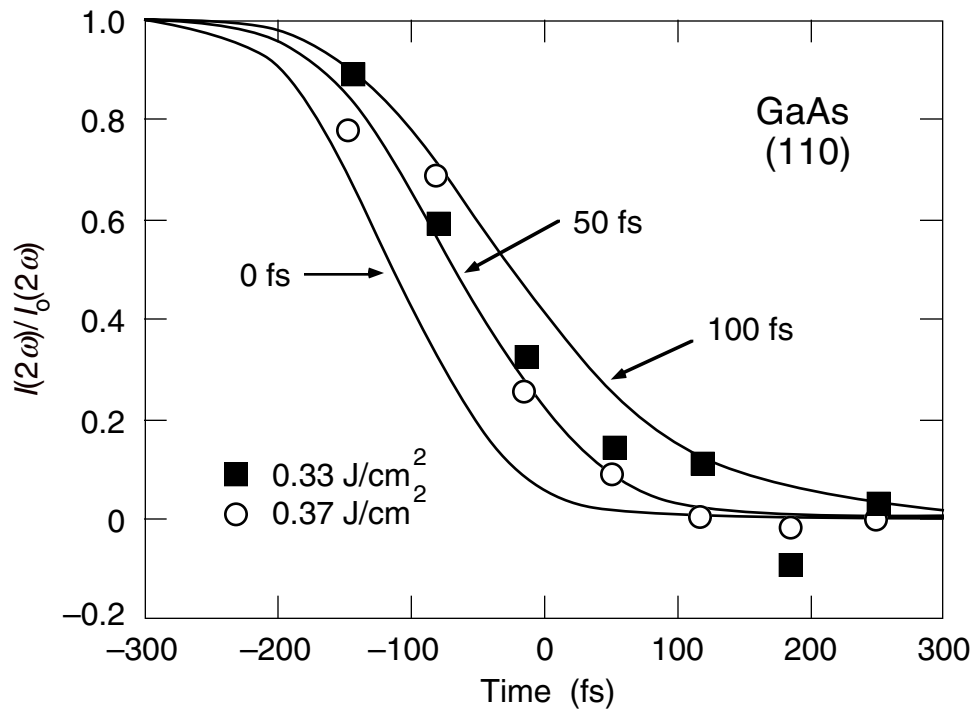


**Fig. 3.13** Second-harmonic response time with account taken for the finite width of the probing pulse. The normalized second-harmonic intensity data for  $0.33$  and  $0.37 \text{ J/cm}^2$  are compared to curves of exponential decay convolved with the pump-probe cross correlation. The data suggest an exponential response time of  $\sim 50$  fs.

The rate of these intervalley scattering processes in GaAs has been investigated by Shah *et al.* using luminescence spectroscopy from 0.5-ps pulses at 2.04 eV [Shah 1987] and by Becker *et al.* using transient absorption spectroscopy with 6-fs pulses having a spectral range from 1.85–2.15 eV. [Becker 1988] Both studies involved photojected carrier densities of order  $10^{18} \text{ cm}^{-3}$ . However, these rates are not particularly sensitive to screening at high carrier density due to the short wavelength of the phonons involved. [Yoffa 1981] For the spectrally narrow 0.5-ps pulses, a scattering time of 100 fs was observed between the  $\Gamma$  and L valleys, with a return time of 2 ps. Much faster scattering was observed with the very broad 6-fs pulses. By varying the

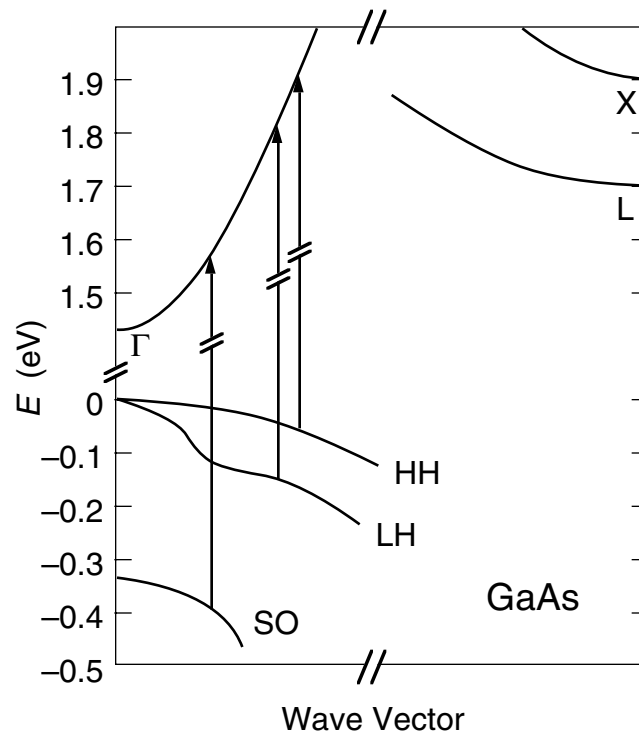


**Fig. 3.14** Vertical 2.0-eV transitions in GaAs. Pump light at  $\lambda = 623 \text{ nm}$  excites electrons in the heavy-hole, light-hole, and split-off valence bands to the  $\Gamma$  valley of the conduction band, with probabilities 40%, 40%, and 20%, respectively. [Lin 1988] Electrons from the light- and heavy-hole bands can scatter into the L satellite valleys by emitting optical phonons. Electrons from the heavy-hole band are excited to states of approximately the same energy as the X valley minima. Figure after Lin 1988.

sample temperature, it was possible to determine a scattering time of 33 fs when both the L and X valleys were accessible, and 80 fs when only the L valley was accessible. It is likely, therefore, that the time scale for scattering out of the  $\Gamma$  valley in the current experiment is less than the pulse duration.

Both types of fast scattering of photoexcited electrons and holes out of the initially occupied states act to moderate bleaching effects, which limit the density of carriers that can be injected. If scattering were immediate, the maximum electron density that could be excited by vertical transitions with 2.0-eV photons would be the integrated density of states of valence electrons within 2.0 eV of the conduction band minimum. This is indicated in the density of states plot of Fig. 3.15, and amounts to less than 5% of the valence electrons, or a density of  $8 \times 10^{21} \text{ cm}^{-3}$ .

The electron density generated by linear absorption of pump photons and the

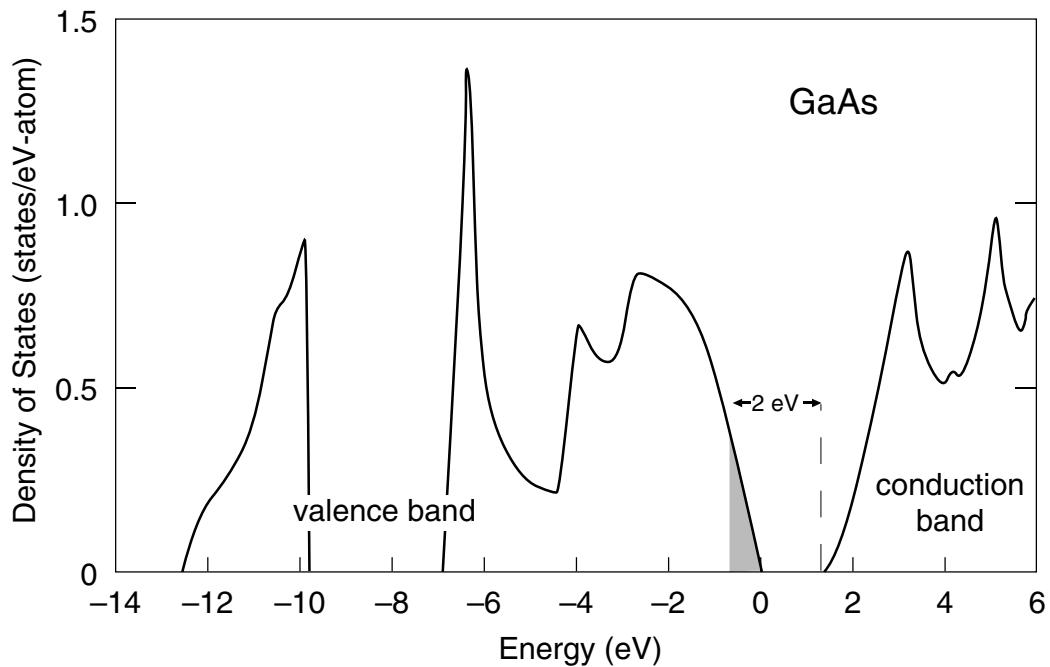


**Fig. 3.15** Density of states of GaAs calculated from pseudopotential theory, after Cohen 1988. The shaded region within 2 eV of the conduction band minimum is less than 5% of the valence band.

energy density deposited in the material are given by the expression

$$u = Nbv = F(1 - R)\alpha . \quad (3.4)$$

At an incident fluence of  $0.1 \text{ J/cm}^2$  this expression gives a photoexcited electron density of  $8 \times 10^{21} \text{ cm}^{-3}$  near the surface, and a deposited energy density of  $2.6 \text{ kJ cm}^{-3}$ , if we take the crystalline values for  $R$  and  $\alpha$ . This agrees with the estimate based on the density of states. Both arguments lead to the conclusion that at threshold roughly 5% of the valence electrons have been excited to conduction states.

This level of valence band depopulation is unlikely to bleach second-harmonic production to the extent observed in, for example, Fig. 3.10. Bonding electrons, and specifically the asymmetry in the Ga–As bond, generate the strong dipole second-harmonic signal in the crystal. Depopulation of bonding electrons does act to decrease second-harmonic generation, as the conduction states produce negligible second harmonic. However, the loss in signal produced by depopulation alone would be a gradual function of carrier density and fluence. Furthermore, the (110) data do not show a significant drop below threshold and the (100) data show an *increase* in second-harmonic intensity (see Fig. 3.4). It is highly unlikely, therefore, that the depopulation of valence electrons produced directly by linear absorption of pump light can account for the drop in second-harmonic intensity.

A final linear mechanism for changing the detected second-harmonic signal is a change in the absorption of light at the second-harmonic wavelength of 311 nm. In the unexcited crystal, the absorption depth for  $\lambda = 311 \text{ nm}$  is  $\alpha^{-1} = 13 \text{ nm}$ . This is a factor of 20 stronger than the absorption at the pump wavelength. Transitions excited by 4.0-eV photons are well separated from the pump-induced transitions at 2.0 eV, both lower than the holes in the valence band and higher than most of the thermalized electrons in the conduction band. Hence, the strong absorption of second-harmonic radiation inside the crystal should not be affected much by valence

band depopulation. Furthermore, any bleaching would act to increase the detected signal.

Having ruled out refractive and bleaching effects at both the probe wavelength and the second harmonic, the remaining possibility is a decrease in  $\chi^{(2)}$  caused by a change in the electronic state to a centrosymmetric configuration. This transformation occurs when approximately 5% of the valence electrons are excited to anti-bonding conduction states. The exponential fits show that this transformation takes place in less than 100 fs.

### 3.6.1 Reflectivity Rise

As the second-harmonic signal drops to zero, the reflectivity begins to rise above the unpumped crystalline value. Within 0.5 ps the *s*-polarized reflectivity rises 44% and the *p*-polarized reflectivity rises 105%, corresponding to absolute reflectivities of 0.68 and 0.47. These high reflectivity values persist unchanged for several picoseconds. Similar reflectivity rises have been observed in short-pulse laser melting experiments on GaAs and other semiconductors as the material attains the metallic character of a molten phase. [Auston 1978, Wood 1981, Liu 1986]

Measurements of the dc electrical conductivity of GaAs at thermal equilibrium near the melting temperature of 1511 K show an increase from  $\sigma_s = 300 \Omega^{-1}\text{cm}^{-1}$  to  $\sigma_l = 7900 \Omega^{-1}\text{cm}^{-1}$  on melting. [Glazov 1969] This is only about a factor of 5 lower than the conductivity of good metals just above their melting temperatures ( $\sigma_{\text{Au}} = 3.2 \times 10^4 \Omega^{-1}\text{cm}^{-1}$  at 1340 K,  $\sigma_{\text{Ag}} = 5.8 \times 10^4 \Omega^{-1}\text{cm}^{-1}$  at 1235 K [Shimoji 1977]). The value reflects the stronger coupling between conduction electrons and ions in GaAs compared with the noble metals. Based on the liquid value of conductivity, the density of free electrons in the high reflectivity phase can be estimated. This presumes that the material has melted in 0.5 ps, an assumption that has not yet

been justified. However, the conductivity reflects the coupling strength of the conduction electrons and ions and so may be reasonably accurate even if the ions have not achieved a thermal velocity distribution above the melting temperature. The Drude expression for the dielectric constant is

$$\epsilon(\omega) = \epsilon_b - \frac{4\pi Ne^2}{m\omega(\omega + i\gamma)} \quad , \quad (3.5)$$

where  $\epsilon_b$  is the polarizability of the valence electrons that remain bound in the liquid state, and  $\gamma$  is the Drude scattering frequency, related to the conductivity by

$$\gamma = \frac{Ne^2}{m\sigma} \quad . \quad (3.6)$$

In the limit of complete ionization,  $\epsilon_b$  tends to 1, the polarizability of the vacuum. Using the free electron mass and 100% ionization of valence electrons, Eq. (3.5) can be used to calculate the *s*- and *p*-polarized reflectivity of the liquid, giving  $R_s = 0.74$  and  $R_p = 0.57$ . These values exceed the measured ones, suggesting that either the valence electrons are not fully ionized in the high reflectivity phase or that their effective mass exceeds the free electron mass. A reflectivity study of the laser melting of GaAs using picosecond pulses at  $\lambda = 0.532, 1.06, \text{ and } 1.9 \mu\text{m}$  also found that the reflectivity of molten GaAs was inconsistent with the assumption of full ionization. [Malvezzi 1986]

The degree of ionization can be estimated by assuming that the susceptibility of the bound charges is proportional to the fraction of charges that remain bound in the molten phase. If  $\varphi$  is the fraction of electrons that ionize, then the susceptibility of the bound charges is given by

$$\chi_b = (1 - \varphi) \frac{n^2 - 1}{4\pi} \quad , \quad (3.7)$$

where  $n$  is the refractive index of the unpumped crystal. By Eqs. (3.5) and (3.6), the susceptibility of the free electrons can be expressed

$$\chi_f = -\frac{\phi N e^2}{m \omega^2} \left[ \frac{1}{1 + i \frac{\phi N e^2}{m \omega \sigma}} \right], \quad (3.8)$$

where  $N$  is the density of valence electrons and  $m$  is assumed to be the free-electron mass. Then the dielectric constant of the system of bound and free charges is

$$\varepsilon(\phi) = 1 + 4\pi(\chi_b + \chi_f) = [n(\phi)]^2. \quad (3.9)$$

The dielectric constant and index of refraction expressed in Eq. (3.9) are plotted in Fig. 3.16. As the free electron density increases, the real part of  $\varepsilon$  decreases, passing through zero at roughly one-quarter ionization. The imaginary part of  $\varepsilon$  increases monotonically, causing both the real and imaginary parts of the index to increase with ionization above the 25% level.

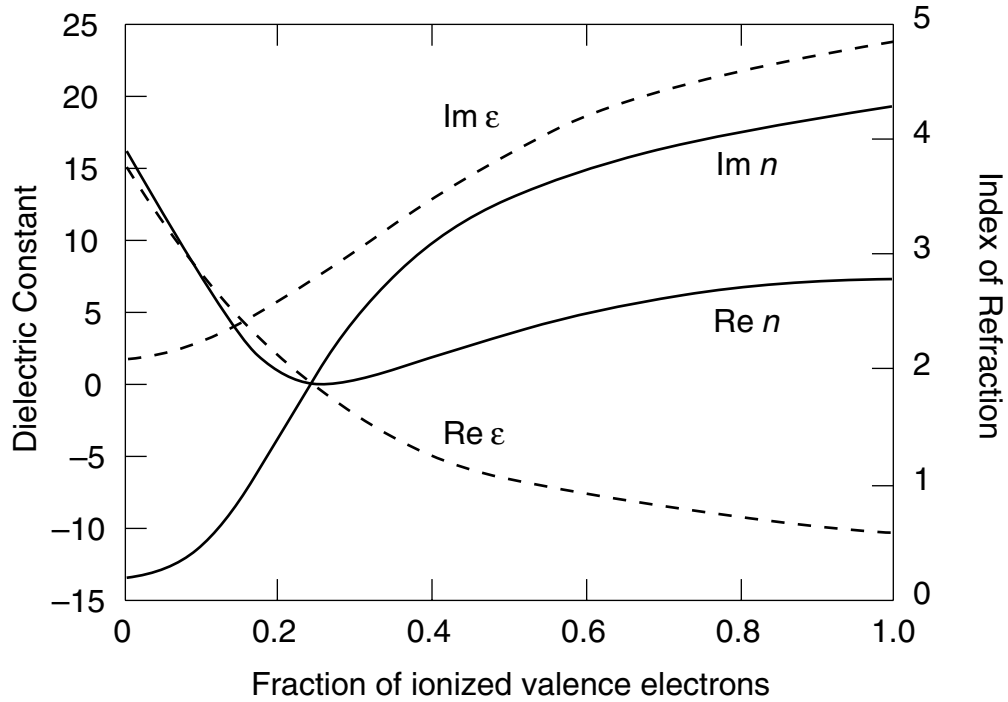


**Fig. 3.16** Dielectric constant and index of refraction as functions of the fraction of valence electrons that are ionized in the molten phase, as calculated from Eq. (3.9).

The reflectivity can be calculated from the index using the Fresnel formulas. Curves of the  $p$ - and  $s$ -polarized reflectivity are plotted in Fig. 3.17. The observed reflectivity peaks are indicated as bars of width corresponding to the standard deviation of the data. Both sets of data agree with  $\sim 45\%$  ionization. Although less than complete ionization, the  $\sim 45\%$  level is an order of magnitude above the 5% obtained by direct excitation with 2.0-eV photons. Evidently, once a critical density of bonding electrons has been excited to anti-bonding conduction states the material ionizes to a degree far beyond that which can be accounted for by linear absorption.

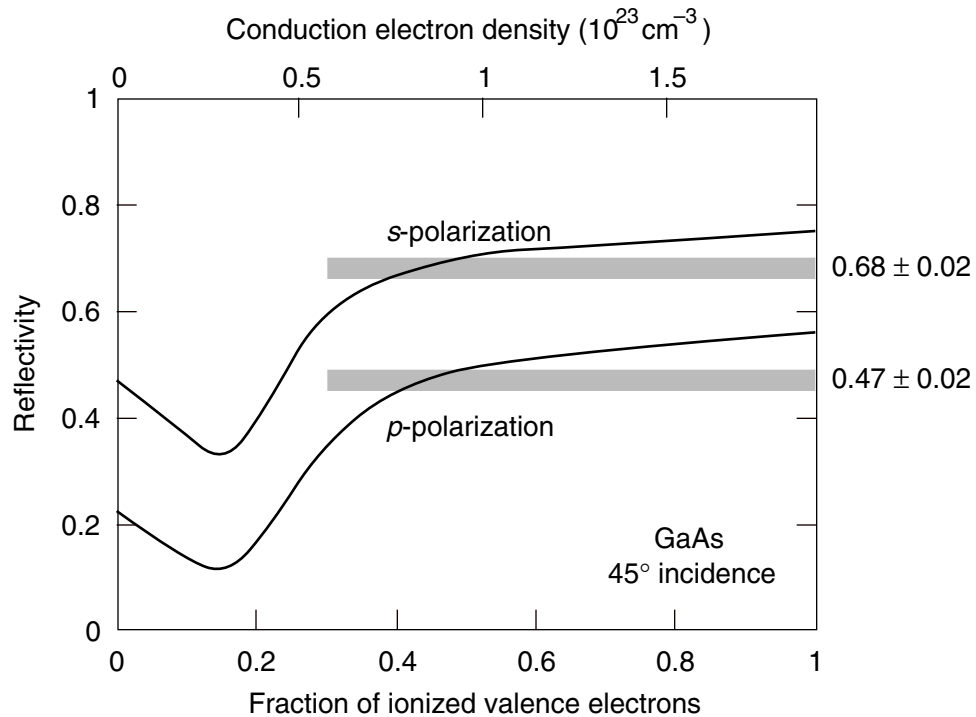


**Fig. 3.17** Computation of the  $s$ - and  $p$ -polarized reflectivity from an optically thick layer of liquid GaAs as a function of the fraction of valence electrons that are ionized in the liquid phase. The polarizability of the valence electrons that remain bound in the liquid is assumed to be that of the unexcited crystal multiplied by the fraction that remain bound. The horizontal shaded bars indicate the measured peak values of reflectivity.

The light energy deposited in the carrier system at the threshold fluence of  $0.1 \text{ J/cm}^2$  is  $\sim 2.6 \text{ kJ/cm}^3$ . This should be compared to the latent heat of melting  $Q_m = 2.83 \text{ kJ/cm}^3$ , which is a measure of the energy necessary to take equilibrium crystalline GaAs at the melting temperature into equilibrium molten GaAs. For a semiconducting material, the latent heat has two distinct components: the energy required to ionize the valence electrons and the heat associated with the increase in entropy on disordering the crystalline lattice of atoms. To the electronic component must be added half the energy required to raise the crystal to the melting temperature, which is the increase in potential energy of the ions stored in the electronic system. This is  $\sim 1 \text{ kJ/cm}^3$ . It may be remarked as well that the energy required to heat the electronic system to the melting temperature under equilibrium conditions is negligible compared to the latent heat. At threshold, therefore, sufficient energy has been absorbed in the electronic system for the electronic structural transition to take place.

### **3.6.2 Lattice Heating**

The high free electron density implies that the laser-excited material has undergone a phase transformation. The question remains whether the high reflectivity phase is molten. At short times, it is likely that the material is far from an equilibrium configuration which could be characterized by a single temperature for both electrons and ions. Initially at least, the electrons will likely be hot and the ions cold. It is clear from numerous carrier thermalization experiments that carrier-carrier scattering is efficient in bringing a high density of electrons to internal thermal equilibrium on a time scale considerably shorter than the duration of the pump pulse. Gallium and arsenic ions, however, are  $10^5$  times heavier than electrons. Their response must be considerably slower. To see whether the lattice has “melted” 0.5 ps after

excitation, it is necessary to consider energy transfer from the hot carrier system to the ions and the disordering of the periodic ionic lattice.

In crystalline GaAs, the dominant energy coupling between hot carriers and the lattice is between electrons and longitudinal optical phonons. For electron densities up to  $10^{18} \text{ cm}^{-3}$ , the LO phonon emission time has been measured to be 165 fs. [Kash 1985] At higher densities the rate decreases due to screening and the reduction of the available phase space. It is also reduced by back transfer of energy from the increasing LO phonon population, the “hot phonon” effect. [Shah 1985] An estimate based on the low-density emission time therefore serves as an upper bound on the energy transfer rate from hot carriers to LO phonons. Taking for the conduction electron density  $N$  the value of  $8 \times 10^{21} \text{ cm}^{-3}$  estimated from the density of states and the low-density emission time  $\tau_{\text{LO}} = 165 \text{ fs}$ , the lattice heating rate is

$$\frac{dT}{dt} = \frac{NE_{\text{LO}}}{\tau_{\text{LO}}c_v} = 150 \text{ K/ps} \quad , \quad (3.10)$$

where the LO phonon energy  $E_{\text{LO}}$  is 31 meV and the lattice specific heat  $c_v = 1.8 \text{ J K}^{-1} \text{ cm}^{-3}$ . At this rate, 8 ps would be necessary to bring the lattice to the melting temperature. Even more time would be required to deliver the latent heat of melting. Consequently, the ions of the lattice gain negligible thermal energy from phonon emission in the 0.5 ps necessary to achieve stable high reflectivity.

### 3.6.3 Lattice Disorder

Let us now turn to the question whether the ions can move far enough in 0.5 ps to get from a  $\bar{4}3m$  to an amorphous configuration in space. At room temperature, the average nuclear thermal velocity can be estimated from equipartition:

$$v_{\text{thermal}} \approx \sqrt{\frac{k_B T}{m_{\text{ion}}}} = 200 \text{ m/s} = 0.2 \text{ nm/ps} \quad . \quad (3.11)$$

Equipartition has been assumed because at room temperature the specific heat is within 4% of the equipartition value. Thermal velocities are sufficient for the ions to move 0.1 nm in 0.5 ps, if the restoring forces on the ions were suddenly removed by the electronic excitation. This is 40% of the bond length of 0.247 nm. Hence even without acquiring appreciable energy from the excitation pulse, the ions can easily disorder on a subpicosecond time scale, provided that the restoring forces are removed.<sup>1</sup>

In fact the bonds are not merely cut by the electronic excitation; the hot electron plasma actively pulls the ions in an ambipolar diffusion process. Because strong electrostatic forces would arise from the spatial separation of electrons and ions, ions are pulled with forces characteristic of the hot electron temperature, which is thousands of degrees above the initial ionic temperature. This is the most rapid mechanism for the transfer of energy from the hot carrier system to the ions.

Hence, the electronic system is observed to undergo a transformation to a centrosymmetric state on a time scale of 100 fs or less when a density of  $8 \times 10^{21} \text{ cm}^{-3}$  electrons is excited to the conduction band. Within 0.5 ps, the density of conduction electrons increases tenfold, yielding a high-conductivity phase with stable reflectivity. By “cutting the springs” that provide the crystal’s cohesion, the electronic excitation enables the ions of the lattice to disorder with room temperature thermal motions. A spatially amorphous configuration can be reached easily in less than 0.5 ps. Furthermore, the plasma interaction of hot electrons with cold ions acts rap-

---

<sup>1</sup> Arguments emphasizing the importance of the electrons at the top of the valence band in stabilizing the transverse acoustic phonon modes in tetrahedrally bonded crystals have been advanced by Phillips [Phillips 1968b, Phillips 1968a], Ridley, and Van Vechten. Based on the temperature dependence of the energy gap, Ridley suggests that “the equivalent of 10 bonds are disrupted per electron-hole pair.” [Ridley 1988 §1.12] Van Vechten estimates that at an electron density of  $8 \times 10^{21} \text{ cm}^{-3}$  the silicon lattice no longer resists shearing stresses. [Van Vechten 1979a]

analysis of the velocity distribution and configuration of the ions has been undertaken, it seems probable that material excited appreciably above the threshold fluence is not far from a molten phase at the density of the solid within half a picosecond, and perhaps considerably faster.

As seen in Fig. 3.12, above a fluence of  $0.25 \text{ J/cm}^2$  the response times of the second-harmonic decay and reflectivity rise cease to decrease with increasing fluence. This is consistent with the onset of electronic disorder once a threshold density of electrons has been excited. Not shown in the figure are the asymptotic values of the second-harmonic and reflectivity signals; these are also independent of fluence, as expected.

Between  $0.15$  and  $0.25 \text{ J/cm}^2$  the second-harmonic response time is constant, but the reflectivity response time decreases with fluence. Furthermore, the asymptotic value of reflectivity is not quite as high in this range as it is above  $0.25 \text{ J/cm}^2$ . This most likely reflects a spatial averaging of the probe beam over a central region that has completely transformed surrounded by material that remains below threshold. Or it may indicate that insufficient energy has been absorbed in the surface layer at this fluence to permit an optically thick layer to melt. It has been remarked that at an incident fluence of  $0.1 \text{ J/cm}^2$  an energy roughly equal to the electronic component of the latent heat of fusion and potential energy rise is deposited in the surface layer, assuming crystalline  $R$  and  $\alpha$ . For the material to melt, the lattice must also be heated to the melting temperature. This requires an additional  $\sim 1 \text{ kJ/cm}^3$  as compared to the  $2.83 \text{ kJ/cm}^3$  of latent heat. At the threshold for the electronic transformation, therefore, the lattice can disorder but not achieve an equilibrium molten phase. For higher absorbed fluence, the material melts and can even be superheated above the vaporization temperature.

The analysis of linear absorption presented above ascribed an upper limit of 5% to the density of valence electrons accessible to 2-eV photons, corresponding to an

absorbed energy density of  $2.6 \text{ kJ/cm}^3$ . Stronger absorption is necessary to achieve melting. A number of mechanisms for this absorption are possible. The narrowing of the gap caused by the high electronic excitation will bring into resonance states lower in the valence band. Two-photon absorption may become important when linear absorption has saturated. And the high density of carriers may begin to absorb appreciable light energy by free carrier absorption.

### **3.7 Reflectivity Drop**

It has been remarked that the reflectivity remains steady at the high metallic value for several picoseconds. By 10 ps, however, it begins a fall that takes it below the unpumped crystalline value within 100 ps. The degree to which the reflectivity is affected increases with fluence until the pump is strong enough to cause a plasma spark to develop in front of the surface. Such reflectivity drops have been observed in a number of semiconductor laser melting experiments with picosecond and femtosecond pulses. [Downer 1985, Liu 1986] There are many conceivable explanations for this behavior, including interference from a receding melt front and various scattering and absorption processes from thermal gradients, surface roughening, or material ejected from the surface, either thermally or otherwise. Gradients in the plane of the surface would produce primarily scattering losses, while ablated material could produce both absorption and scattering losses.

In principle, a grazing-incidence pulse passing at appropriate delay in the vicinity of the pumped spot could determine whether a cloud of ablated material causes the reflectivity drop. In practice it is impossible to focus such a beam to probe the extremely thin volume of interest. To clarify the relative importance of scattering, we have performed time-resolved scattering experiments at probe wavelengths of 620 nm and 650 nm. We have also examined the GaAs surface after excitation to

determine the quantity of material ablated and the morphology of the pump-induced crater. The results suggest that enough material is ejected from the surface to account for the drop in reflectivity.

Figure 3.18 shows the relative *s*-polarized reflectivity as a function of time for three different fluences well above the melting threshold. The data were taken in the same manner as those presented in Fig. 3.11, and simply extend the time axis. From a peak value of 1.44, the relative reflectivity begins to drop somewhat within the first 10 ps. After a delay of 25 ps, the intensity has been cut in half, and it continues to drop, reaching a minimum at 200 ps of between 0.2–0.3 of the crystalline value. By 0.5 ns, the reflectivity appears to begin to recover. Similar behavior is observed with a *p*-polarized probe on a (100) GaAs surface.

Given the limited travel of the translation stage in the optical delay line, half a

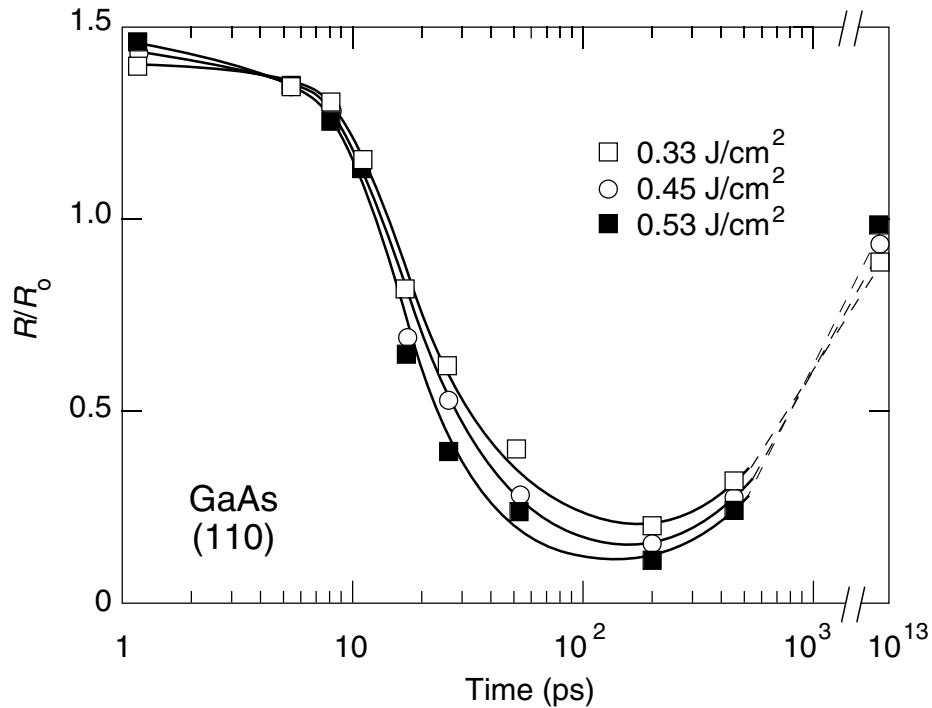


**Fig. 3.18** Drop in relative reflectivity with time for three fluences that are above the melting threshold. Note the values at the extreme right, which were taken several seconds after the excitation pulse.

nanosecond is the maximum delay probed. However, by blocking the pump beam and taking a second probe shot before translating the sample, it is possible to measure the reflectivity of the material several seconds after excitation. These data are indicated at the right of the figure. The reflectivity recovers almost completely to the value of unexcited crystalline material. If deformation of the surface causes the reflectivity loss, by the time the material cools (and resolidifies) it has relaxed sufficiently for a near total recovery in reflectivity. The reflected second-harmonic signal, on the other hand, recovers only to about half the crystalline value and shows considerable shot-to-shot variation. This indicates that the melted material does not regrow epitaxially from the crystalline bulk. It furthermore suggests that femtosecond pulses are ill-suited for laser annealing.

### **3.8 Scattering of Probe Light**

The simplest observation of the scattering of light from the delayed probe pulse can be made by eye: for  $F > 0.2 \text{ J/cm}^2$  and a probe delay of 50 ps or more, the excited spot begins to scatter noticeable red light out of the direction of specular reflection. The scattering does not appear to depend strongly on angle or on the polarization of the probe beam.

To study the time dependence of the intensity of scattered light, a collecting lens with  $f$ /number 3 was positioned above the plane of incidence to collimate scattered light emerging in  $\sim 1.5\%$  of the solid angle in front of the wafer. This light was focused on the entrance slit of a streak camera with 2-ps resolution (Hamamatsu Photonics C1587). Scattered light from the pump beam serves as a time reference. For a probe delay of 200 ps, a strong scattering signal was detected at moderate gain on the multichannel plate. However, due to the strength of elastic scattering from the much stronger pump beam, it was not possible to decrease the

probe delay to less than  $\sim 100$  ps.

The problem of scattering from the pump beam can be eliminated by shifting the probe wavelength and placing frequency-selective optics before the detector. A 10-nm bandpass interference filter at a central wavelength of 650 nm blocks the light scattered from the pump beam completely. The probe beam is shifted to this wavelength by continuum generation in a cell of water. After the continuum beam is recollimated, an interference filter selects the light around  $\lambda = 650$  nm, which is amplified in a Nd:YAG-pumped dye cell. Scattered light from the shifted probe is then detected with a standard photomultiplier tube. Figure 3.19 shows the fluence dependence of the scattered light at probe delays of 20, 50, and 200 ps. The scattering at a fixed delay is only weakly dependent on the pump fluence, and increases

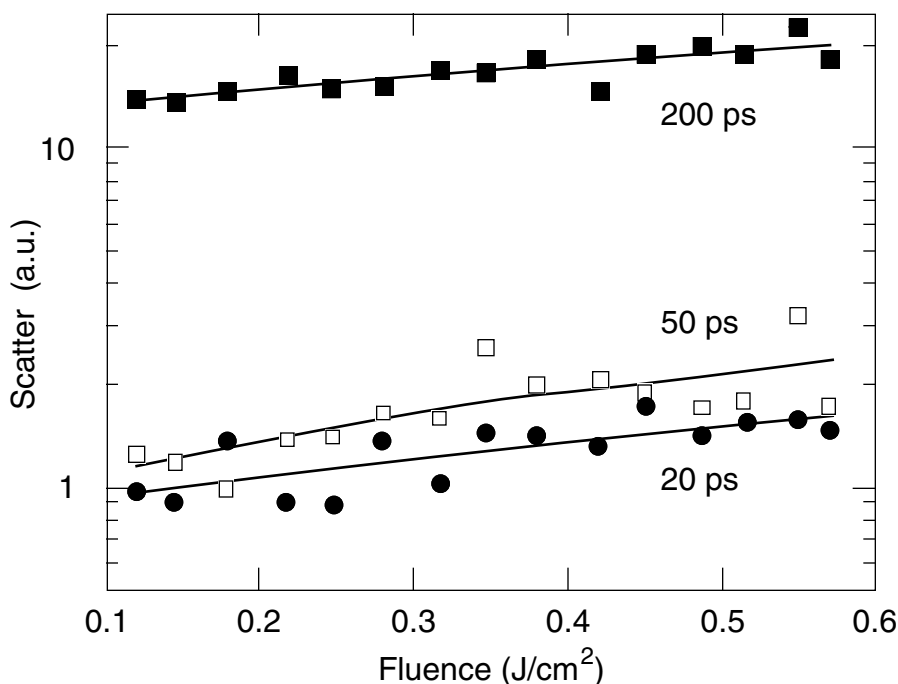


**Fig. 3.19** Scattering of probe light out of the plane of incidence as a function of pump fluence for probe delays of 20, 50, and 200 ps. Scattering losses increase slightly with fluence and more strongly with time.

with probe delay.

### 3.9 Ablation of Material

The amount of material ablated from the excited spot was measured with a Dektak profilometer, which measures the vertical displacements of a stylus that rests on the wafer surface. As the wafer is translated in-plane, a series of roughly flat-bottomed pits is recorded on a strip chart. Figure 3.20 shows the depth of these pits as a function of the incident fluence. Although the data show a fair amount of scatter, it is clear that the depth is only weakly dependent on fluence. The typical depth for the fluence range 0.15–0.35 J/cm<sup>2</sup> is approximately 90 nm.

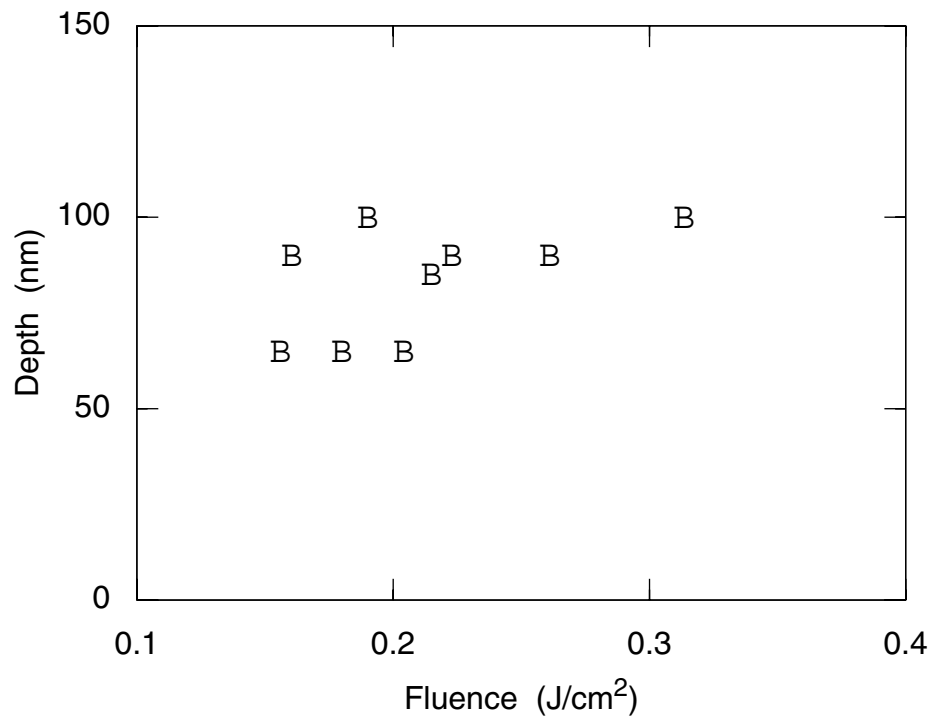


**Fig. 3.20** Depth of pits created by femtosecond laser excitation.

### **3.10 Surface Morphology**

Scanning electron micrographs were taken of several craters to investigate the morphology of the resolidified material. Figure 3.21 shows micrographs taken on an unpumped area, and in the center of spots with fluences 0.07, 0.18, and 0.32 J/cm<sup>2</sup>. The surface inside the craters is seen to roughen with increasing fluence and appears to be covered with a layer of roughly spherical particles whose density increases with fluence. These particles are remarkably uniform in size, having typical diameters in the range 0.1–0.2  $\mu\text{m}$ .

### **3.11 Discussion of the Reflectivity Drop**

The time behavior of the reflectivity signal argues strongly against explanations based on melt fronts and thermal gradients in the plane of the surface. The  $\sim 45\%$  ionization that produces the high reflectivity between 0.5 and 2 ps reduces the penetration depth of the probe light from 230 nm to approximately 15 nm. The boundary between solid and molten material must be deeper than this distance already by 0.5 ps in order to produce the high reflectivity signal. To cause a drop, an interface would have to develop within the shortened absorption depth. Picosecond and nanosecond experiments on resolidification rates in semiconductors and metals have found that the time scale for resolidification is a few tens of nanoseconds. [Brown 1980] Hence a melt front cannot explain the reflectivity drop.

Thermal gradients in the plane of the surface would produce index gradients that scatter probe light. Such gradients would arise from hot spots in the pump beam or defects in the surface. The build up of index gradients would show some delay with respect to the pump pulse as energy relaxes from the hot carriers to the ions. Once the driving field is removed, and most of the excess carrier energy has

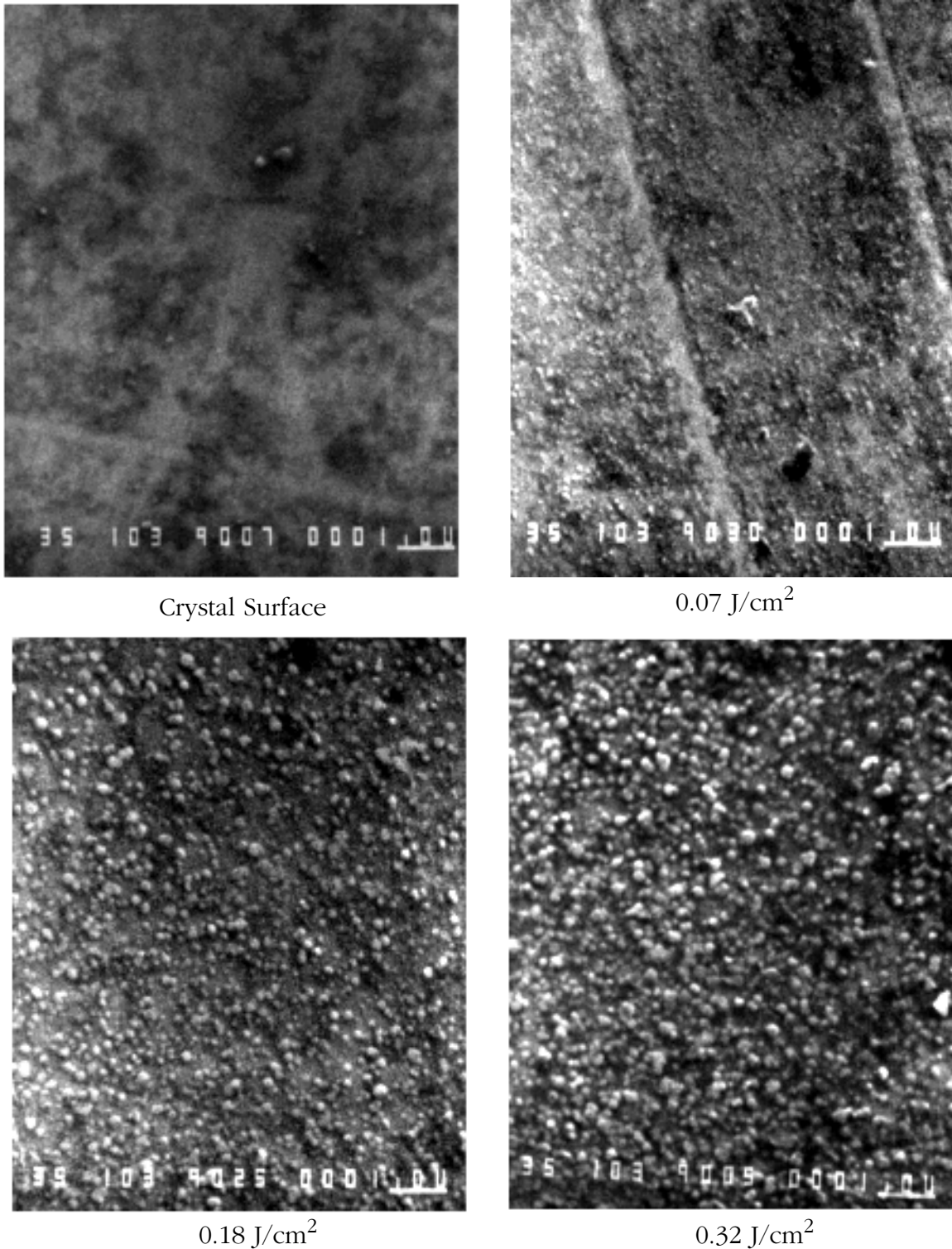


**Fig. 3.21** Electron micrographs of the GaAs surface after laser excitation. The images have the same scale, indicated by the white line in the lower right corner which is 1  $\mu\text{m}$  long. The image at the upper left shows a portion of the wafer surface unexposed to laser radiation.

relaxed to the ions, the gradients would relax and the scattering losses decrease. The time scale for energy relaxation from the hot electrons has been discussed above. For crystalline material, LO phonon emission transfers the excess energy of a photoexcited electron to the lattice in a few picoseconds. Although Auger recombination can maintain a significant temperature difference between electrons and ions for hundreds of picoseconds below the melting threshold, [van Driel 1987] once the material melts ambipolar diffusion rapidly thermalizes the dense plasma. By a few tens of picoseconds after excitation, the only active thermal processes are evaporation of atoms and ions from the surface and diffusion of heat into the bulk.

### 3.11.1 Evaporation

Bloembergen and others have argued that evaporation cannot eject enough material to perturb the probe beam significantly on the picosecond time scale. [Bloembergen 1986] A crude model of the evaporation process for equilibrium liquid and vapor at the surface temperature  $T_s$  is a simple mass flux balance: the mass leaving the condensed phase is equal to the mass fleeing the surface in the vapor phase. The velocity of flight of the vapor is taken to be the characteristic velocity of the vapor phase,  $v_{th} = \sqrt{k_B T_s / m}$ , which is the thermal velocity of an atom at  $T_s$ . For vapor leaving the interface at this velocity, equating the fluxes gives  $v_{th} \rho_g = v_s \rho_l$ , where  $v_s$  is the velocity at which the surface recedes, and  $\rho_g$  and  $\rho_l$  are the densities of the gas and liquid. Material is removed as rapidly as the thermal velocity can carry it away. This expression overestimates the evaporation rate because the binding energy per atom in the condensed phase  $E_{cob}$ , which produces a reduction in the probability of escape given by  $\exp(-E_{cob} / k_B T_s)$ , has been suppressed. Even if one assumes strong superheating above the atmospheric vaporization temperature of 2073 K, and highly compressed vapor  $\rho_g / \rho_l = 10^{-2}$ , the

velocity at which the surface recedes is less than

$$v_s < \frac{\rho_g}{\rho_l} \sqrt{\frac{k_B T_s}{m_{\text{atom}}}} \approx 0.01 \text{ nm/ps} \quad . \quad (3.12)$$

At this rate, the surface recedes only 2 nm in 200 ps, which is the time delay at which the reflectivity is at a minimum. Such a small quantity of material could have at most a slight impact on the reflectivity.

There is ample reason to question the assumptions of equilibrium liquid and vapor phases. Particles leaving the surface to form a cloud of vapor simply do not have the time and space to expand via collisions to the equilibrium density. It is likely that the density of the cloud at early times is only slightly lower than that of the condensed phase material. The hot condensed matter also does not have time to attain an equilibrium density. Diamond structure semiconductors generally become more dense on melting as the coordination of the atoms increases from 4 to roughly 6. In GaAs, the relative increase in density is 10.7%. [Glazov 1969] For a gradual melt into the bulk, the front surface must recede to accommodate the density increase. In the current experiment, the atoms in the molten layer do not have time to move far enough for the melt front to propagate in from the front face. A substantial negative pressure is established after the electronic ionization reaches equilibrium liquid levels that acts both to pull the liquid towards the bulk and to break it apart into small particles. Perhaps the shock wave from the rebound of the material collapsing towards the bulk propels atoms, ions, and small clusters away from the surface.

The presence of a cloud of neutral and ionized particles in front of the surface can affect the measured reflectivity signal through absorption and scattering. Isolated atoms and ions of Ga and As have no absorption lines near 650 nm; [Weast 1976] they have essentially no effect on the probe beam. However, as clusters of increasing size form, the dielectric response of the aggregate of atoms gradually

passes from a collection of discrete lines to the broad response of condensed phase material, either metallic liquid or semiconducting crystal. This transition occurs at a size of between  $10^3$  and  $10^5$  atoms per cluster, [Brus 1986, Andres 1989] corresponding to radii between 3 and 13 nm for spherical particles. In a 1985 paper on the femtosecond laser melting of silicon, Downer *et al.* attributed the presence of a dark spot over the center of the pumped region imaged by white light reflection to absorption by a cloud of silicon droplets ejected from the surface. [Downer 1985] Mie scattering theory was used to estimate the strength of the absorption and its wavelength dependence.

### 3.11.2 Mie Scattering

Mie scattering theory describes the absorption and scattering of a light beam incident on spherical particles characterized by a dielectric constant  $\epsilon$ . [Van de Hulst 1957] The scattering cross section is developed in powers of  $x = 2\pi a/\lambda$ , where  $a$  is the radius of the spherical particle. To fourth order in  $x$ , the absorption and scattering cross sections are

$$\sigma_{\text{abs}} = \frac{8\pi^2 a^3}{\lambda} \left\{ \text{Im} \left( \frac{\epsilon - 1}{\epsilon + 2} \right) + x^2 \text{Im} \left( \frac{1}{15} \left[ \frac{\epsilon - 1}{\epsilon + 2} \right]^2 \frac{\epsilon^2 + 27\epsilon + 38}{2\epsilon + 3} \right) + x^3 \text{Re} \left( \frac{2 \left[ \frac{\epsilon - 1}{\epsilon + 2} \right]^2}{3} \right) \right\} \quad (3.13)$$

and

$$\sigma_{\text{scat}} = \frac{8\pi^2 a^3}{\lambda} x^3 \left( \frac{2}{3} \left| \frac{\epsilon - 1}{\epsilon + 2} \right|^2 \right) . \quad (3.14)$$

For small  $x$ , scattering is negligible compared to absorption. For a beam traveling through a cloud of spherical particles, the attenuation can be expressed

$$\frac{I}{I_0} = e^{-\sigma NL} , \quad (3.15)$$

where  $N$  is the number density of particles and  $L$  the distance traveled. Neglecting lateral transport of material out of the path of the probe beam, the product  $NL$  can be expressed in terms of the depth  $d$  of material ablated from the crystal surface as

$$NL = \frac{\rho_{\text{xtal}}}{\rho_{\text{droplet}}} \frac{6d}{4\pi a^3 \cos \theta} , \quad (3.16)$$

where  $\theta$  is the incidence angle of the probe beam and  $\rho$  is the density.

Using the dielectric constant deduced from the high reflectivity plateau and

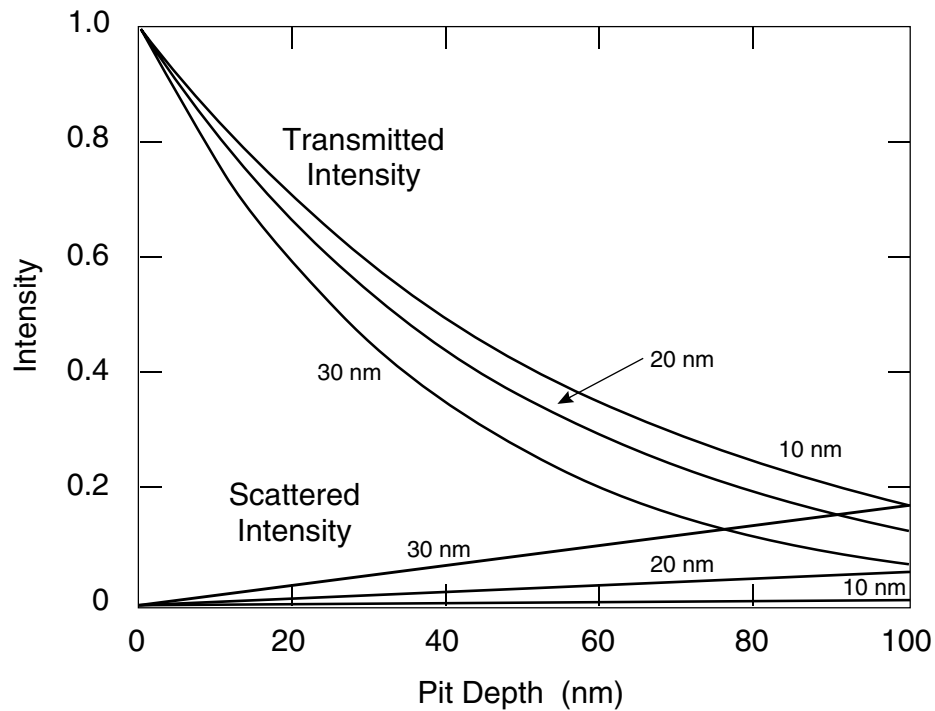


**Fig. 3.22** Fraction of incident probe light transmitted through a cloud of spherical particles having the dielectric constant of laser-excited GaAs as a function of the depth of material ablated from the surface. The curves correspond to particle radii of 10, 20, and 30 nm. The lines at the bottom of the figure indicate the fraction of incident probe intensity that is scattered away from the forward direction.

Eq. (3.9), the total cross section can be computed. For particle radii less than about 10 nm, it is dominated by the size-independent leading term in the absorption expansion. The lowest order scattering term is cubic in  $x$  and nearly equal to the  $x^3$  absorption term. Thus it is necessary to retain all three absorption terms in a regime where appreciable scattering is detected. Figure 3.22 shows the fraction of probe light transmitted by the cloud of ablated material as a function of the depth of material removed from the surface for three different particle sizes. For a depth of 90 nm, which is the depth of the resulting craters, only 10–20% of the probe beam is transmitted through the cloud. This agrees with the minimum observed reflectivity at 200-ps delay. If a fraction of the material remains in particles too small to be described by the liquid dielectric constant, as is quite likely particularly at short times, then the transmitted intensity would be higher. The rise in scattering observed between 20 ps and 200 ps could result both from the greater quantity of ejected material, as well as the increasing cluster size at the later time.

### 3.12 Conclusions

The dynamics of the phase transformation of crystalline GaAs excited with intense femtosecond pump pulses at  $\lambda = 623$  nm have been investigated using time-resolved reflection second-harmonic generation and reflectivity. At a threshold incident fluence of  $0.1 \text{ J/cm}^2$ , the second-harmonic signal vanishes in the pumped material, indicating that the electronic state of roughly the upper 90 atomic layers undergoes a transformation to a centrosymmetric configuration. Above  $0.15 \text{ J/cm}^2$  the time for this transformation is fluence-independent and less than 100 fs. Furthermore, the energy absorbed by the electronic system at threshold is approximately equal to the latent heat of melting of crystalline GaAs. This suggests that when an energy equal to the electronic contribution to the latent heat has been absorbed in

the electronic system, the electronic system undergoes the phase transformation.

Within 0.5 ps the reflectivity is observed to rise to a steady high value that indicates approximately 50% of the valence electrons participate in conduction, assuming the free electron mass. This is an order of magnitude higher than the density of electrons created by the linear absorption of pump light. In the 0.5 ps before the reflectivity stabilizes, very little energy is transferred from the carriers to the lattice by the emission of longitudinal optical phonons, which is the dominant energy transfer mechanism in the crystal. It is likely that the ions of the crystalline lattice disorder while still near room temperature and that they are strongly heated by the electron plasma as the carrier density increases.

Several picoseconds after excitation, the reflectivity is observed to drop. Near 200-ps delay it falls to a minimum which is roughly 20% of the unpumped crystalline reflectivity. By 500 ps it begins to recover. Probe light is observed to scatter out of the plane of incidence at delays from 20 to 200 ps and is considerably stronger at later times. Examination of the pits produced by laser excitation indicates that roughly 90 nm of material is ablated, independent of the incident fluence. Electron micrographs of the bottom of the pits indicates that they are covered with solidified spherical droplets of roughly uniform size. These observations are consistent with the ejection of a cloud of material from the excited surface, provided that the cloud evolves into droplets of sufficient size within 200 ps.

## Chapter 4

# Interlayer Transport of Photoexcited Carriers in Type II Multiple Quantum Well Structures

### 4.1 Introduction

This chapter presents some of the first time-resolved studies of carrier dynamics in staggered type II GaAs/AlAs multiple quantum well structures. Using transient absorption spectroscopy, we demonstrate that electrons excited in the  $\Gamma$  valley of the GaAs layers scatter on a subpicosecond time scale to X states in the AlAs layers.<sup>1</sup> Holes created in the GaAs layers remain confined at the top of the valence band in the GaAs layers, leading to the segregation of charges in adjacent layers and to fairly

---

<sup>1</sup> This research was conducted at AT&T Bell Laboratories, Murray Hill, New Jersey. The time-resolved work was performed by Benjamin I. Greene, John Federici, and Peter Saeta. Low temperature cw luminescence spectra of the samples were taken by Ronnie Spitzer and Barbara Wilson.

to the layers (giving rise to the quantum-confined Stark effect), the field in staggered type II structures is periodic and fails to produce observable shifts in the absorption near the energy of the band gap.

### **4.1.1 Semiconductor Heterostructures**

In the last decade, advances in molecular beam epitaxy and other nanoengineering techniques have opened up the possibility of creating layered structures with precise control over composition almost to the scale of a single atomic layer. These techniques allow one to tailor the electrical and optical properties of a semiconductor heterostructure through careful choice of layer materials and thicknesses. Layers can be doped to provide an excess of either positive or negative charge carriers to increase the conductivity of the structure. The gap can be adjusted to reduce absorption at certain useful laser wavelengths and to heighten optical nonlinearities. These synthetic structures have stimulated a wealth of research activity both for the inherent interest in the electrical and optical properties of heterostructures and for their practical applications in telecommunications, optoelectronics, and potentially optical computing. Excellent reviews on these structures have appeared in the literature. [Esaki 1986, Weisbuch 1987] A brief overview of the properties of quantum wells important for these experiments appears in the following sections.

### **4.1.2 Quantum Wells**

A layer of narrow band gap material sandwiched between barrier layers of material with a wider gap creates a structure in which electrons and holes are (partially) confined to the narrow-gap layer. This layer is called the “well,” and such a heterostructure is called a “quantum well.” The potential acting on electrons and holes in a quantum well closely approximates the square-well potential studied in

introductory quantum mechanics courses. Under appropriate conditions, carriers can be confined to such a quasi two-dimensional layer while retaining high mobility in the plane of the layer.

More complicated structures can be created by increasing the number of layers. Double quantum well structures consist of a five-layer sandwich in an ABCBA pattern. If the barrier C is not too thick, an electron in one well has a nonzero probability of tunneling into the other well. The lowest energy electron wavefunctions become the symmetric and antisymmetric combinations of being in both wells simultaneously. This is the simplest example of coupling between quantum wells.

In a multiple quantum well structure, well layers and barrier layers of a consistent thickness and composition alternate for many periods. If the barrier layers are thick enough that the wavefunctions of carriers confined in the wells do not penetrate appreciably into the wells on either side, the multiple quantum well structure behaves as a set of independent single quantum wells. The advantage of repetition in this case is to increase the total volume of the wells, or equivalently the total areal density of carriers that can be excited.

When the barrier layers are only a few atomic layers thick, so that the wavefunctions of carriers in the well layers extend into the adjacent wells, the structure is called a superlattice. [Esaki 1969] Carriers are no longer confined within a single well, but can hop from well to well. In the plane of the layers, the material displays the periodicity of the unit cell. In the direction perpendicular to the layers, the material shows the additional periodicity of the layered structure. The normal band structure of the crystalline lattice becomes folded on itself to accommodate the reduced Brillouin zone of the superlattice. Bands become divided into sub-bands; new optical transitions are possible between various sub-bands.

Wells of the type described above, in which the highest-lying valence band and the lowest-lying conduction band occur in the same layer (the well), are designated

“type I.” Dingle and coworkers [Dingle 1975] constructed some of the earliest semiconductor heterostructures in 1975, using layers of GaAs and  $\text{Al}_x\text{Ga}_{1-x}\text{As}$ . When  $x < 0.4$ , the wells made of these materials are type I. The gap of the GaAs layers lies entirely within the gap of the  $\text{Al}_x\text{Ga}_{1-x}\text{As}$  layers. The bulk of work on single and multiple quantum well structures before 1988 concentrated on wells constructed of these materials. [Wilson 1988] With a higher aluminum fraction or different materials, other types of wells are possible. In type II structures, the highest valence band and the lowest conduction band occur in adjacent layers. Type II structures can be subdivided into two classes, depending on whether the lowest conduction band is above or below the highest valence band. In the former case, the structure is called “staggered type II”; in the latter, “misaligned type II.” The three cases are illustrated in Fig. 4.1.

## 4.2 Multiple Quantum Well Samples

The samples used in these experiments consist of 50 periods of either 8 or 11

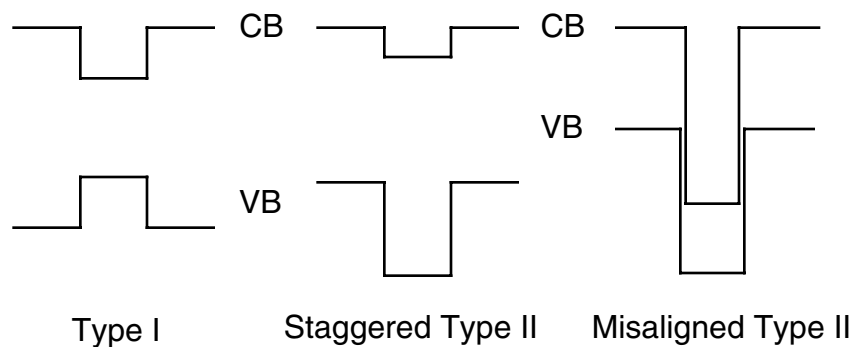


**Fig. 4.1** Schematic representation of the different types of band alignments in semiconductor heterostructures. For  $(\text{GaAs}/\text{Al}_x\text{Ga}_{1-x}\text{As})$  with  $x < 0.40$ , the structure is type I. With higher Al concentration and appropriate well width, these materials can produce staggered type II wells. [After Wilson 1988]

monolayers of GaAs alternating with 25 monolayers of AlAs. They are grown on a GaAs substrate separated by a 100-Å AlAs etch stop layer. The hard, transparent AlAs layer is necessary so that the opaque GaAs substrate can be removed by etching without damaging the wells. A solution of ammonium hydroxide in hydrogen peroxide with a pH of 7.1 at room temperature etches GaAs at the rate of approximately  $1 \mu\text{m}/\text{minute}$ , but is almost inert on AlAs. Therefore, it is possible to remove the substrate by mechanically polishing down to a thickness of a few microns, followed by etching with the ammonium hydroxide solution, stopping the etch when the remaining structure becomes transparent. For this purpose the samples are fixed with the quantum well side down to a fused silica disk, on which they remain

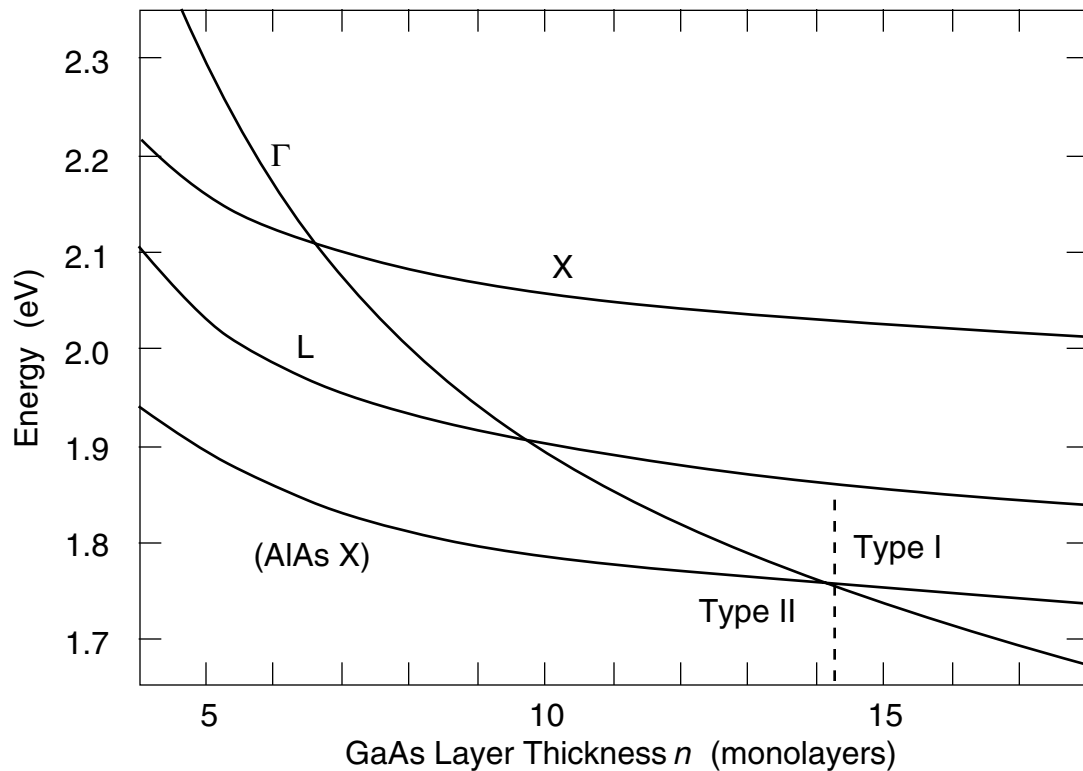


**Fig. 4.2** Direct recombination energies for conduction electrons in the  $\Gamma$ , L, and X valleys of GaAs and the X valley in the AlAs barrier layer with GaAs holes as a function of the well width. Below 14 monolayer thickness, the quantum well structure is staggered type II. [After Wilson 88a]

mounted for the experiments.

The AlAs barriers in these samples are thick enough that the wavefunctions of electrons in the GaAs layers do not penetrate significantly into other GaAs layers. The samples are multiple quantum well structures, not superlattices. They are staggered type II wells because of the large confinement energy of  $\Gamma$  electrons in the GaAs conduction band. For wide GaAs layers, GaAs/AlAs quantum wells are type I. As the well size is decreased, confinement drives the energy of conduction electrons in the GaAs layers up and the energy of valence band holes down. The increase is inversely proportional to the carrier effective mass. Therefore, the light  $\Gamma$  electrons are most strongly affected. In Fig. 4.2 the recombination energies of various conduction band electrons with GaAs holes are plotted as a function of the GaAs layer thickness. For GaAs layers thinner than 14 monolayers, the lowest conduction band states are the X valley states in the AlAs barrier layers, resulting in staggered type II structures.

### 4.3 Luminescence Excitation Spectra

Spectroscopic evidence for the type-II character of these quantum wells can in principle be obtained either from absorption or luminescence spectroscopy. Since the gap is indirect, however, the spectrum is more easily obtained by luminescence excitation spectroscopy. [Finkman 1986, Danan 1987, Dawson 1987, Minami 1987] The low-temperature luminescence spectrum of the 11-monolayer sample is shown in Fig. 4.3. The data are obtained at 6 K with an incident intensity of  $0.25 \text{ W/cm}^2$  at  $\lambda = 514 \text{ nm}$  (photon energy of 2.42 eV) for the indirect  $X \rightarrow \Gamma$  transitions. For the direct  $\Gamma \rightarrow \Gamma$  transition the excitation intensity was increased by a factor of 10. The relative intensities of luminescence for the direct and indirect transitions depend on excitation intensity and temperature. [Finkman 1986, Danan 1987, Dawson 1987,

Minami 1987] For our samples, as the excitation intensity is lowered to the detectability limit for direct luminescence, the relative yield of luminescence, indirect to direct, increases to roughly  $10^4$ .

As indicated in the inset of Fig. 4.3,  $X \rightarrow \Gamma$  luminescence from carriers in the AlAs layers requires the recombination of an electron in one layer with a hole in the adjacent layer. Furthermore, the X electrons of the AlAs have high crystal momentum, whereas the holes in the GaAs layers are near the zone center. However, the normal  $k$ -conservation rule can be broken by leakage and mixing of the electron

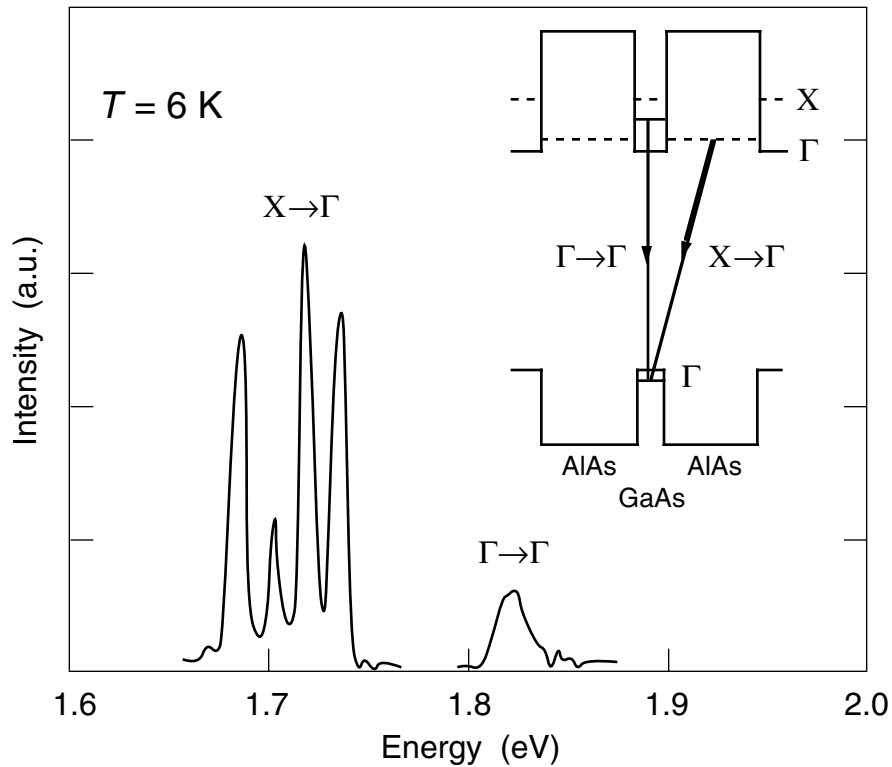


**Fig. 4.3** Low temperature cw luminescence spectrum of the 11-monolayer GaAs/AlAs multiple quantum well structure. The sample was held at  $T = 6$  K and excited with an argon laser at a photon energy of 2.42 eV. The data for the  $\Gamma \rightarrow \Gamma$  transition at  $\sim 1.83$  eV were taken with an excitation energy 10 times that for the  $X \rightarrow \Gamma$  data at  $\sim 1.72$  eV. The inset indicates the direct and indirect transitions observed in the spectrum.

wavefunction into the  $\Gamma$  states of the GaAs. [Dawson 1987] Of the four peaks near  $\sim 1.7$  eV labeled  $X \rightarrow \Gamma$  in Fig. 4.3, the one at highest energy is assigned to a zero-phonon transition. The remaining peaks at lower energy are tentatively assigned to transitions accompanied by the emission of different AlAs phonons. [Dawson 1987]

The very high relative luminescence yield, indirect to direct, at low intensity indicates that very few of the photoexcited carriers remain in the GaAs layers, since direct recombination rates should be much higher than indirect rates for equal carrier densities. The intensity dependence of the relative luminescence yield suggests that considerable nonradiative recombination of carriers takes place for even modest carrier densities.

## **4.4 Femtosecond Transient Absorption Spectroscopy**

The 8- and 11-monolayer samples were studied with a femtosecond pump-probe differential absorption technique using excitation pulses tuned just above the absorption edge. For the 8-monolayer sample, this is at 1.97 eV, and for the 11-monolayer sample it is 1.77 eV. The pulses are generated with a colliding-pulse mode-locked femtosecond dye laser operating at 100 MHz at a wavelength of 630 nm. The pulse train is amplified in a 4-stage dye amplifier pumped by a 300-mJ Nd:YAG laser operating at a repetition rate of 10 Hz. The first three amplifier stages are transversely pumped, and the final stage is a 10-cm long longitudinally pumped cell. The output of the amplifier is divided into pump and probe beams. The probe beam is focused in a cell of  $\text{CCl}_4$  to generate a continuum pulse from which the chirp is removed with a grating pair. In the experiments on the 8-monolayer sample, the pump beam is used at the unshifted wavelength of 630 nm (1.97 eV). For the 11-monolayer sample, the pump beam is used to generate a continuum in the

same manner as the probe. After dispersion compensation, a portion of the continuum is selected by passing the beam through a 10-nm bandpass interference filter, followed by a stage of transverse amplification. A cross correlation of the (attenuated) pump and probe beams yields a full width at half maximum of 200 fs. This indicates that the pulse widths of the pump and probe beams are  $\sim 100$  fs.

In order to minimize Fabry-Perot fringes arising from reflections at the interfaces between the air, the sample, and the fused silica disk, the probe beam is *p*-polarized and strikes the sample at Brewster's angle. The pump beam is orthogonally polarized to minimize coherence coupling between the beams.

#### **4.4.1 Differential Absorption Spectra**

The spectrum of the transmitted probe light is recorded by focusing the recollimated beam onto the entrance slit of a grating spectrometer attached to an optical multichannel analyzer. The dispersion of the grating is small enough to permit the wavelength range 550–800 nm to be recorded simultaneously. A spectrum is taken by accumulating the signal for approximately 20 seconds, effectively averaging over 200 laser shots. To correct for stray light and dark current in the detector, a baseline spectrum ( $S_0$ ) is recorded with the pump and probe beams blocked before taking data. This spectrum is then subtracted from transmission spectra before further analysis.

A differential absorption spectrum is taken in two passes. First, a transmission spectrum ( $S_1$ ) of the probe beam is accumulated with the pump beam blocked. Next, the pump beam is unblocked and a modified transmission spectrum ( $S_2$ ) is recorded with the probe pulse at a fixed optical delay with respect to the pump pulse. The differential absorption spectrum is then computed as

$$S = -\log\left(\frac{S_2 - S_0}{S_1 - S_0}\right), \quad (4.1)$$

which is expressed in units of optical density (*OD*) to remove the dependence on sample thickness. A decrease in absorption (a “bleach”), corresponding to an increase in transmission, produces a *negative* differential absorbance.

The differential absorption spectrum of the 11-monolayer sample at room temperature is shown in Fig. 4.4. The incident excitation intensity was roughly  $1 \mu\text{J}/\text{cm}^2$ . The origin of delay time was assigned to the temporal peak of the sample response. By a delay time of 3.6 ps it is clear that a partial recovery of the initial bleaching has taken place. Further differential absorbance spectra like that of

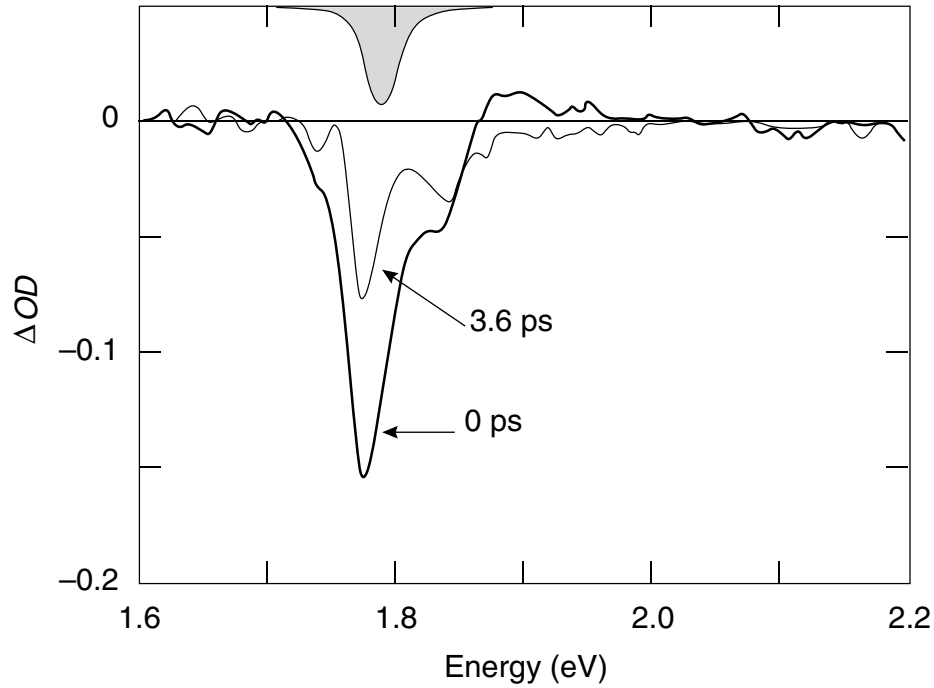


**Fig. 4.4** Differential absorbance spectra of the 11-monolayer GaAs/AlAs MQWS taken at the temporal peak of bleaching (0 ps) and 3.6 ps later. The shaded curve at the top of the figure indicates the spectrum of the excitation pulse.

Fig. 4.4 taken out to delay times of 30 ps show essentially no further change.

#### 4.4.2 Time-resolved Differential Absorption Spectra

To measure the time dependence of the bleaching signal, a slightly modified detection scheme is used. The setup is shown in Fig. 4.5. A portion of the probe

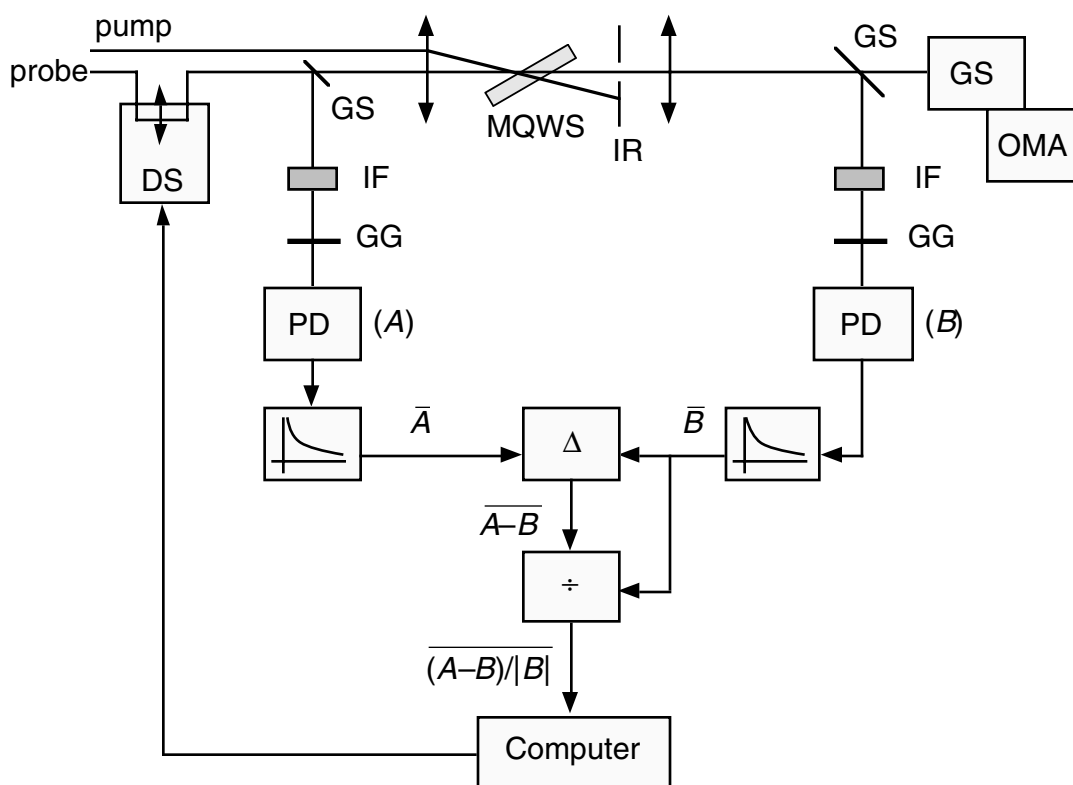


**Fig. 4.5** Setup for time-resolved differential absorption measurements. The probe beam passes through an optical delay line atop a computer-controlled  $\mu\text{m}$ -step delay stage (DS) and a glass slide (GS) that splits off roughly 10% as a reference signal before striking the MQWS sample. The reference signal (A) passes through a 10-nm bandpass interference filter (IF) and a ground glass (GG) before being detected with a photodiode (PD). The transmitted probe beam (B) is detected in similar fashion. The two signals are processed by analog amplifiers that compute the relative difference between the signals, which is recorded by the computer.

beam is split off with a glass slide before the beam strikes the sample and relayed through an interference filter to a photodiode (*A*). A second slide sends a portion of the transmitted beam through an identical interference filter to a second photodiode (*B*). Ground glasses are used to ensure that the energy is distributed evenly over the photodiodes and that they do not saturate. The signals from the photodiodes are fed into “boxcar” integrator/amplifiers that subtract the background level and perform a slight temporal averaging of the signals. Differential amplifiers then compute the relative difference, which is digitized by a computer. The computer averages the signal at a given delay for 3 laser shots, then increases the length of the optical delay line by a fixed increment (either 1 or 2  $\mu\text{m}$ , yielding time steps of 6.7 or 13.3 fs).

Figure 4.6 shows the time-resolved differential absorption of the 11-monolayer sample monitored at a wavelength of 700 nm (1.77 eV). The excitation intensity for these data was roughly half that for the data of Fig. 4.4. The data show a fast bleaching signal followed by a partial recovery to a steady value slightly less than half the initial bleach. An exponential fit to the signal for  $t > 0$  gives a  $1/e$  recovery time of 0.4 ps.

Similar spectral and kinetic results were obtained with the 8-monolayer sample, but the recovery time for this sample was much faster. Due to the higher confinement energy in the narrow-well sample, the band edge was just below the energy of the amplified CPM pulses, which had a spectral range from 622 to 630 nm, centered at 626 nm (1.97 eV). Figure 4.7 displays the temporal response of the 8-monolayer sample at room temperature. Interference filters centered at 630 nm were used to select the probe wavelength range. The fluence of the excitation pulses was approximately  $0.6 \text{ mJ/cm}^2$ . An exponential fit to the decaying portion of the signal gives a recovery  $1/e$  time of 140 fs. As this is comparable to the pulse duration of the pump and probe pulses, the actual response time is likely to be somewhat faster.

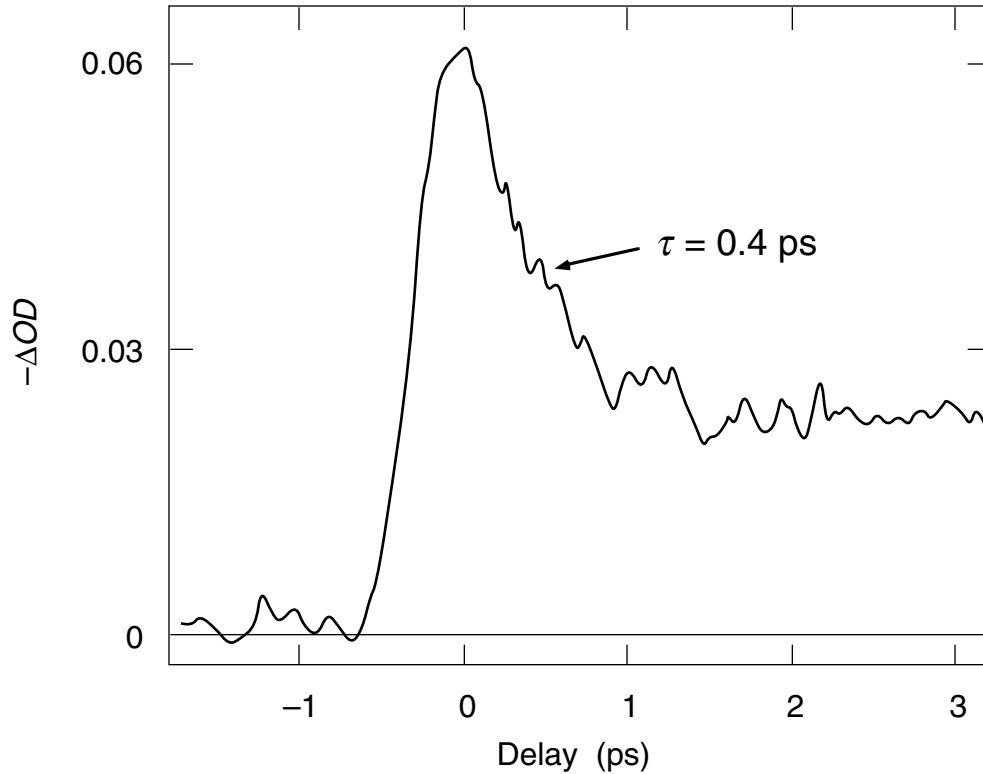


**Fig. 4.6** Temporal trace of the 11-monolayer GaAs/AlAs MQWS sample optical response monitored at 700 nm (1.77 eV). An exponential fit to the signal for  $t > 0$  gives a  $1/e$  recovery time of 400 fs.

After the initial rapid changes that occur within the first  $\sim 3$  ps (see Figs. 4.4, 4.6, and 4.7), essentially no further changes in the differential absorption spectrum are observed out to 30 ps, the longest delay time investigated. Figure 4.8 shows the 11-monolayer sample absorbance spectrum as a function of delay time. The solid line is the unexcited absorbance spectrum, which was taken with a low-intensity cw white light source. The excited absorbance spectra at 0 ps and 3.6 ps were obtained by adding the differential absorption spectra of Fig. 4.4 to the unexcited absorbance spectrum.

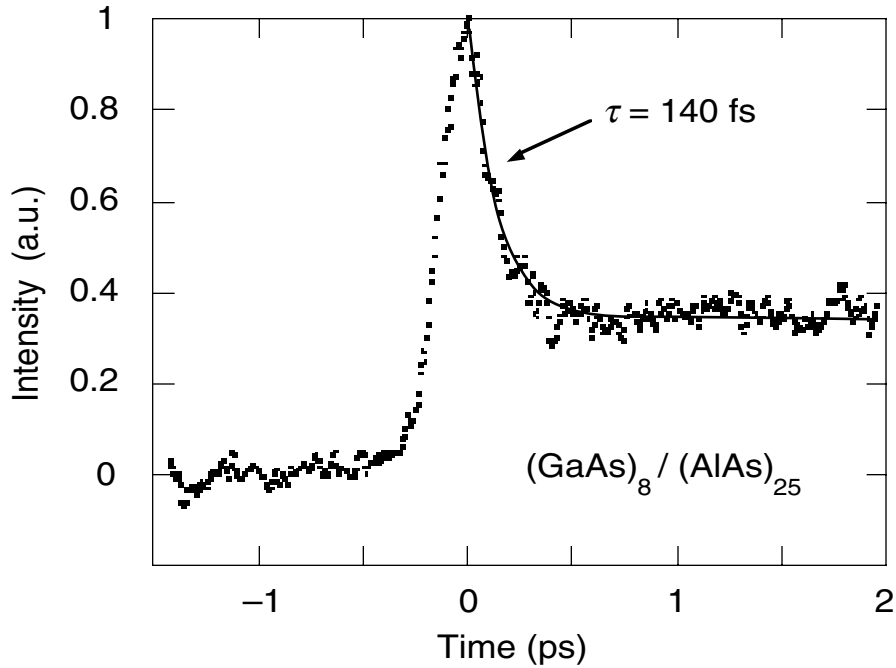


**Fig. 4.7** Transient absorption spectrum of the 8-monolayer sample at  $\lambda = 630 \text{ nm}$ . An exponential fit to the data after the peak at  $t = 0$  gives a  $1/e$  recovery time of 140 fs.

## 4.5 Discussion

The pump-induced bleach in the sample absorption near the origin of time and the partial recovery of the material absorption strongly suggest that the photoexcited electrons scatter rapidly from the  $\Gamma$  valley in the GaAs layers to the conduction minimum X valleys in the adjacent AlAs layers. As will be seen, this interpretation is consistent with the transient absorbance and cw luminescence data, as well as with previous femtosecond studies on type I GaAs multiple quantum well structures. From our data we estimate characteristic material relaxation times of 100 fs for the 8-monolayer sample and 400 fs for the 11-monolayer sample, indicating interlayer scattering of carriers on these time scales.

The first indication of ultrafast scattering of photoexcited carriers is manifested in the spectral width of the peak at  $t = 0$  in Fig. 4.4, which is roughly three times the spectral width of the pump pulse. Similar spectral broadening effects have been observed in femtosecond pump-probe experiments on bulk semiconductors and type I semiconductor quantum wells, [Knox 1988] and have been attributed principally to carrier-carrier collisions. Thermalization times for photoexcited carriers in GaAs at the injected density of these experiments are expected to be shorter than the pulse duration, resulting in a significant spectral broadening near  $t = 0$ .

As is clear from the absorption spectrum (Fig. 4.8) at  $t = 0$ , the excitonic peak<sup>1</sup> at  $\sim 1.77$  eV has disappeared and carriers at the band edge have largely been depleted. Three picoseconds later, the dominant spectral effect is a partial recovery

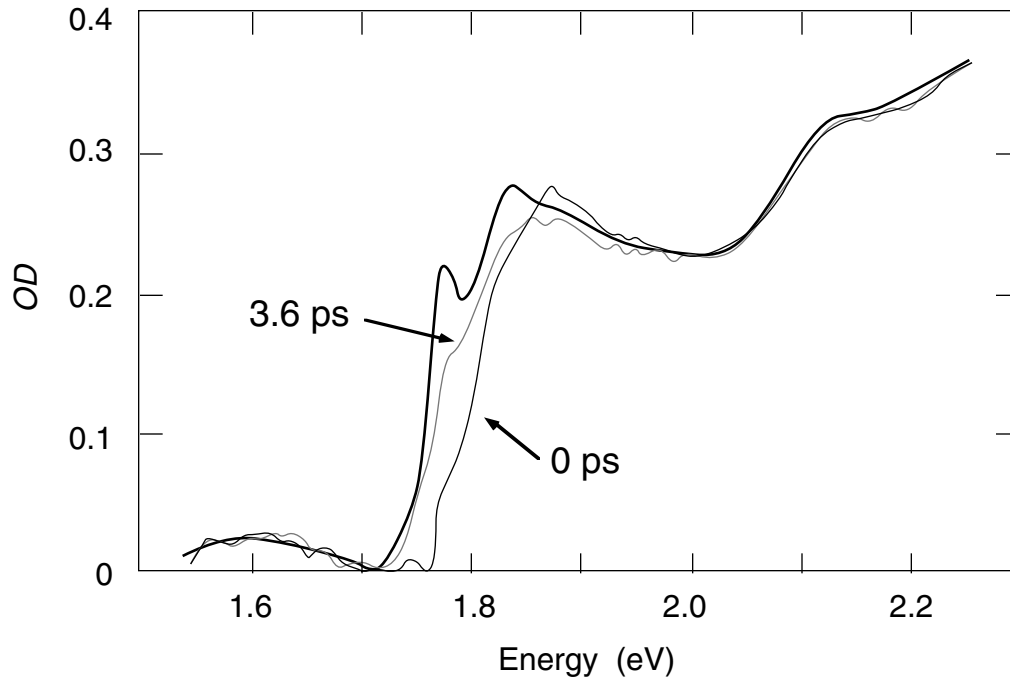


**Fig. 4.8** Absorbance spectra of the 11-monolayer GaAs/AlAs MQWS sample without photoexcitation (dark line), at the temporal peak of the optical response (0 ps, thin line), and after relaxation is complete (3.6 ps, dotted line). The small peak below the band edge is most likely an artifact of multiple reflections from the air-silica and air-sample interfaces.

of the band edge absorption. Additional subtle but reproducible spectral changes appear at higher energies, up to 200 meV above the band edge.

The very low efficiencies for  $\Gamma \rightarrow \Gamma$  luminescence ( $\sim 10^{-4}$ ) rule out the possibility that the persistent bleaching observed after  $\sim 3$  ps is due to  $\Gamma$  electrons in the GaAs layers. This long-lived bleaching can be attributed instead to the presence of zone-center holes in the GaAs layers. The highest point of the valence band in either layer is at the  $\Gamma$  point in the GaAs layers, which is where the holes are created by photoexcitation. Therefore, the holes remain in the GaAs layers until they recombine with conduction electrons. The measured relative yields of luminescence, [Saeta 1989] indirect to direct, are consistent with a  $\sim 100$ -fs  $\Gamma \rightarrow X$  relaxation. The intensity dependence of the relative yields is understood in a model that stipulates a relatively low density of indirect luminescence centers that can be saturated. The low intensity and low temperature luminescence ratio of  $10^4$ , indirect to direct, puts an effective upper limit on the  $\Gamma$  electron lifetime of 100 fs, assuming a 1-ns natural radiative lifetime in GaAs. [Hwang 1973]

$\Gamma \rightarrow X$  relaxation in type II multiple quantum well structures requires electron transport from, in this case, a GaAs layer to an adjacent AlAs layer. This cannot occur any faster than the  $z$ -component (perpendicular to the layers) of the electron velocity would allow. With a sample GaAs layer thickness of  $\sim 25$ – $30$  Å for the 8-monolayer sample, a relaxation time of 100 fs implies a velocity of  $\sim 3 \times 10^6$  cm/s. The typical velocity of injected electrons can be estimated from the Fermi velocity of a free electron gas, which is given by the expression

---

<sup>1</sup> The exciton giving rise to this peak is an electron-hole pair in which the electron and hole are bound in a hydrogenic state by the electrostatic attraction between them. In bulk GaAs, the binding energy is about 5 meV, [Ridley 1988] making the exciton difficult to observe at room temperature. In quantum wells, the binding energy is increased by confinement, [Miller 1984] producing a distinct peak even at room temperature.

$$v_F = \frac{\hbar}{m}(3\pi^2n)^{1/3} , \quad (4.2)$$

where  $n$  is the density of carriers of mass  $m$ . [Ashcroft 1976] The estimated injected carrier density in the GaAs layers is  $2 \times 10^{18} \text{ cm}^{-3}$ , which gives a Fermi velocity of  $5 \times 10^6 \text{ cm/s}$  if one takes for  $m$  the free-electron mass, and significantly higher if one uses the reduced mass of  $\Gamma$ -valley electrons. Interlayer transport of carriers in 100 fs, therefore, appears quite reasonable. This assumes efficient momentum transfer from the in-plane directions to the  $z$ -direction perpendicular to the layers.

### 4.5.1 Quantum-Confined Stark Effect

The separation of electrons and holes in adjacent layers gives rise to electric fields in the direction perpendicular to the layers. These fields may shift the energy levels of electron and hole states near the gap, thereby perturbing the absorption spectrum near the gap. The persistent presence of holes at the top of the valence band, which causes some bleaching of the band edge absorption, makes it difficult to observe spectral shifts caused by the electric fields.

The modified potentials associated with externally applied electric fields, as in the quantum-confined Stark effect, [Miller 1984, Miller 1985] are qualitatively different from the modified potentials resulting from charge separation in type II multiple quantum well structures. The external field that produces the quantum-confined Stark effect uniformly skews the potential, pulling the electron and hole in an exciton to opposite sides of the well, where they are prevented from further separation by the discontinuities in the respective band energies in the barrier layers. This raises the energy of holes and lowers the energy of electrons, while preserving the Coulomb correlation of the exciton, even at quite intense applied field. The resulting shift in the energy of the excitonic resonance can be up to 2.5 times the zero-field binding energy. [Miller 1984]

The field in a type II multiple quantum well structure, on the other hand, produces a periodic distortion in the potential which tends to increase the energy of both electron and hole. A rough estimate for the well widths and excited carrier densities of our samples suggests that shifts would be less than about 5 meV, which is too small to be experimentally resolved.

### **4.5.2 Scattering Rate Dependence on Well Thickness**

The  $\Gamma \rightarrow X$  scattering rate for the 8-monolayer GaAs well is 3 to 4 times faster than that of the 11-monolayer well. In both structures, the 25-monolayer AlAs barrier is thick enough that the GaAs layers are essentially isolated. It appears, therefore, that the rate increases as the well width is decreased. At least three factors associated with the well width may be responsible for the increased scattering rate. First, the energy difference between the  $\Gamma$  and X quantized levels is greater in the narrow-well structure. This increases the density of states to which the  $\Gamma$  electrons in the GaAs layers can scatter in the AlAs layers. Second, roughness at the boundary between layers, which is typically of the order of one monolayer, is proportionally greater in the narrow-well sample. Third, the fraction of the wavefunction of  $\Gamma$  electrons in the GaAs layers that extends into the AlAs layers increases with decreasing well width.

Surface roughness most likely acts to increase the scattering rate by mixing different conduction states at the interfaces, and by providing scattering sites to provide the momentum necessary for electrons to scatter to the high-momentum X states. Increased overlap of the wavefunctions in the GaAs and AlAs layers would also increase the scattering rate.

The dependence of the scattering rate on wavefunction overlap can be calculated by applying Fermi's Golden Rule for an interaction Hamiltonian  $H_i$ . To com-

To compare the scattering rates of the two configurations of this experiment, it is sufficient to calculate the relative scattering rate. If we assume a simple multiplicative interaction Hamiltonian, the contribution to the scattering rate from wavefunction overlap is then proportional to the square of the overlap integral between the initial and final states, or

$$\tau^{-1} \sim |\langle \psi_X | \psi_\Gamma \rangle|^2 . \quad (4.3)$$

The wavefunction envelope for  $\Gamma$  electrons in the GaAs layers can be calculated by solving the one-dimensional Schrödinger equation for an electron in a square-well potential given by the offset in energy between  $\Gamma$  states in the GaAs layers and  $\Gamma$  states in the AlAs layers. The effective mass of  $\Gamma$  electrons is different in GaAs and AlAs. Therefore, the mass of the electron is different inside and outside the well. Similarly, the envelope for X electrons in the AlAs layers can be calculated from the offset in X state energy and the X state effective masses. These are given in Fig. 4.9.

For a well of depth  $V$  and width  $2a$  centered at the origin, we are looking for a solution of energy  $E < V$ . The lowest energy solution has the form

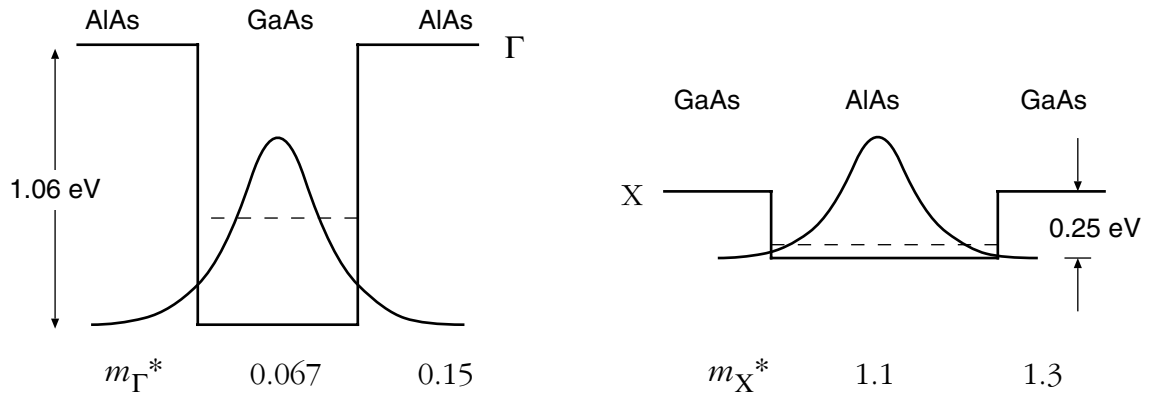


**Fig. 4.9** Effective masses and band offsets for  $\Gamma$  electrons (left figure) and X electrons (right figure) in GaAs/AlAs quantum wells. The values are taken from Adachi 1985. The dashed lines represent the energy of the lowest-lying quantized state in each quantum well.

$$\psi_a(z) = A \cos(kz) \quad (4.4)$$

inside the well and

$$\psi_b(z) = B e^{-K|z|} \quad (4.5)$$

in the barrier. In these expressions, the wave vectors  $k$  and  $K$  are given by

$$k = \frac{\sqrt{2m_a E}}{\hbar} \quad (4.6)$$

and

$$K = \frac{\sqrt{2m_b(V-E)}}{\hbar} . \quad (4.7)$$

The question as to the appropriate boundary conditions to apply at  $z = \pm a$  has inspired some disagreement. [Cho 1987] While it is clear that the wavefunction is continuous at the boundary between layers, it is not so clear what constraint to impose on the derivative of the wavefunction. Two choices are common. The first is the simple carry-over from the original statement of the problem in which the mass of the particles does not change from well to barrier. In this case the first derivative of the wavefunction must be continuous across the boundary. Bastard has argued that when the mass of the particle changes in going from one layer to the next, the appropriate condition is the continuity of the probability current across the boundary. [Bastard 1981] In this case, it is the derivative of the wavefunction divided by the effective mass that is continuous. The boundary conditions applied to the solution of form given by (4.4) and (4.5) yield the constraints

$$A \cos ka = B e^{-Ka} , \quad (4.8)$$

and

$$A k \sin ka = K B e^{-Ka} , \quad (4.9)$$

for the case of continuity of the derivative. If it is the probability current that is con-

tinuous, (4.9) becomes

$$\frac{Ak}{m_a} \sin ka = \frac{KB}{m_b} e^{-Ka} . \quad (4.10)$$

The quotient of the two boundary condition equations gives the eigenvalue equation for the energy of the particle

$$k \tan ka = K , \quad (4.11)$$

and

$$\frac{k}{m_a} \tan ka = \frac{K}{m_b} , \quad (4.12)$$

respectively. These can be solved iteratively to yield  $k$ ,  $K$ , and  $E$ . By applying the normalization condition,

$$2 \int_0^a \cos^2(kz) dz + 2 \int_a^\infty e^{-2Kz} dz = 1 , \quad (4.13)$$

the amplitudes  $A$  and  $B$  can be found for both the  $\Gamma$  and X states. The overlap integral is then given by

$$\langle X | \Gamma \rangle = \int_0^{a_\Gamma} A_\Gamma B_X \cos k_\Gamma z e^{-K_X(z+a_X)} dz + X \leftrightarrow \Gamma , \quad (4.14)$$

where it has been assumed that the penetration of the wavefunction beyond the center of the barrier layer is negligible.

The computation for the (GaAs)<sub>8</sub>/(AlAs)<sub>25</sub> and (GaAs)<sub>11</sub>/(AlAs)<sub>25</sub> quantum wells is summarized in Table 4.1. For the boundary condition expressed in Eq. (4.9), the ratio of the squares of the overlap integral (4.14) for the narrow quantum well with respect to the wider wells is 2.5, predicting a scattering rate 2.5 times higher for the 8-monolayer sample. Considering the crudeness of the calculation, this is reasonably good agreement. When Bastard's continuous probability current boundary condition is used, the ratio decreases to 1.8, which is somewhat lower than the

System	Continuous $\partial_z \psi$	Continuous $\frac{\partial_z \psi}{m}$
(GaAs) <sub>8</sub> /(AlAs) <sub>25</sub>	0.0144	0.0171
(GaAs) <sub>11</sub> /(AlAs) <sub>25</sub>	0.0058	0.0096
ratio	2.5	1.8

**Table 4.1** Squared overlap between GaAs  $\Gamma$  and AlAs X conduction states. The greater overlap for the narrow well system increases the scattering rate.

observed rate, but qualitatively in agreement with the data.

## 4.6 Conclusions

For GaAs layer thickness less than roughly 14 monolayers, GaAs/AlAs quantum well structures are staggered type II. Photoexcited electrons settle at the conduction minimum in the X valleys of the AlAs layers, creating a spatial separation of charges. Radiative recombination rates are low due to the doubly forbidden nature of the recombination, which is indirect both in  $k$ -space and in real space. We have performed femtosecond pump-probe transient absorbance spectroscopy on two type II multiple quantum well samples having GaAs layer thicknesses of 8 and 11 monolayers. Following an initial bleaching of the absorbance produced by the photoinjected carriers, the absorbance partially recovers to a stable value that persists at least 30 ps. The fast recovery, measured to be 100 fs for the 8-monolayer sample and 400 fs for the 11-monolayer sample, is explained by scattering of  $\Gamma$ -valley electrons in the GaAs layers to the X-valley conduction band minimum states in the adjacent AlAs

layers. Persistent bleaching is attributed to the presence of zone-centered holes in the GaAs layers and is expected to persist to a nanosecond time scale.

Research on fast  $\Gamma \rightarrow X$  carrier transfer in type II (Al)GaAs/AlAs superlattices and multiple quantum wells has shown that wavefunction overlap is the most important factor in determining the scattering rate. For wide wells, LO-phonon scattering to X states is the dominant mechanism for charge transfer, whereas in very thin wells, potential fluctuations caused by interface roughness probably dominate the scattering. [Feldmann 1990]

## Chapter 5

# Picosecond Laser Melting of Silicon

Optical reflectivity studies of silicon surfaces during laser annealing with nanosecond and picosecond pulses above a fluence threshold reveal a high-reflectivity phase that is established during the excitation pulse. [von der Linde 1982] Such a high-reflectivity phase is consistent with the melting of an optically thick layer at the surface. Conductivity measurements on silicon demonstrate that it is metallic in the molten phase. [Glazov 1969] The time-resolved optical experiments yield reflectivity values during the high-reflectivity phase that are consistent with a Drude model of molten silicon based on the dc conductivity. [Liu 1983] The model also assumes that the valence electrons are completely ionized and have the free-electron mass. Hence, the above-threshold optical response indicates that the surface layer melts on a time scale of tens of picoseconds.

If the incident pump fluence is significantly higher than the threshold value, strong heating of the molten layer is expected, due to the much stronger absorption of pump light in the metallic phase. [Fauchet 1988] Because the excitation energy is deposited in the molten material in an extremely short time, it may even be possible

to superheat the liquid significantly above the vaporization temperature. Since the conductivity of metals decreases with temperature, the reflectivity of the hot liquid should be lower than that of molten silicon just above the melting temperature. A dip in reflectivity would be short-lived, however. Large temperature gradients and high thermal conductivity in the molten phase rapidly cool the surface. Model calculations indicate that the reflectivity dip lasts only  $\sim 20$  ps. [Fauchet 1988] Experiments to investigate the superheating of the molten layer therefore require time resolution of a few picoseconds.

Standard pump-probe experiments with 20-ps pulses suffer from both spatial and temporal convolution effects. Even when the probe beam is focused completely inside the pumped area, it averages over a region of different pumping conditions. When the profile of the pump beam is less than ideal, this averaging introduces appreciable error. Surface plasma caused by the concentration of excitation energy at imperfections in the silicon surface can also introduce significant error when the detection scheme lacks spatial resolution. [Wang 1989] Furthermore, the time resolution of standard pump-probe measurements is limited to the duration of the probe pulse, which averages reflectivity conditions over its temporal profile.

To obtain spatial resolution and improved time resolution, and to measure the time profile of the reflectivity on a single-shot basis, we have modified the standard pump-probe technique to image the excited area of the silicon surface with a streak camera.<sup>1</sup>

---

<sup>1</sup> This work was performed by Maarten Buijs, Juen-Kai Wang, and Peter Saeta (see Wang 1989 and Buijs 1990). A computer simulation of the experimental conditions was written by Yakir Siegal and Peter Saeta, and is discussed in an appendix to this thesis.

## 5.1 Experimental Technique

At normal incidence the reflectivity of silicon rises from 37.4% in the crystalline phase to 73% in the liquid phase, nearly a factor of 2. For improved sensitivity to changes in the reflectivity, a  $p$ -polarized probe near the Brewster minimum at  $75^\circ$  can be used. [Fauchet 1988] Depending on the precise probing angle in the vicinity of the Brewster minimum, as indicated in Fig. 5.1, the reflectivity can jump by an order of magnitude or more on melting, thereby providing a clear signature of the melting transition.

The setup for the experiment is shown in Fig. 5.2. Pulses for the experiment are produced by frequency-doubling the output of a mode-locked Nd:YAG laser. The

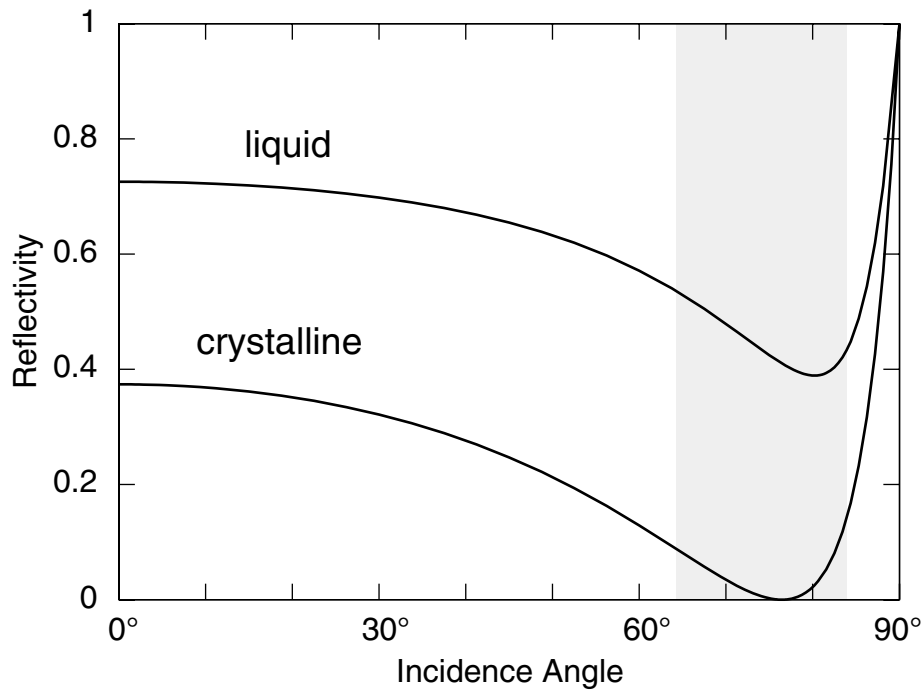


**Fig. 5.1**  $p$ -polarized reflectivity of crystalline and molten silicon as a function of incidence angle. For the shaded region near Brewster's angle, the reflectivity rises by roughly an order of magnitude on melting.

pulses have a wavelength of 532 nm and temporal width of approximately 30 ps (FWHM). A beam splitter divides the YAG beam into pump and probe beams. The pump beam passes through an optical delay line before striking the single-crystal silicon sample at normal incidence. In order to stretch the probe beam in time, it passes through a pair of Michelson interferometers with arms of unequal length. This produces four “images” of the original probe pulse that are delayed with

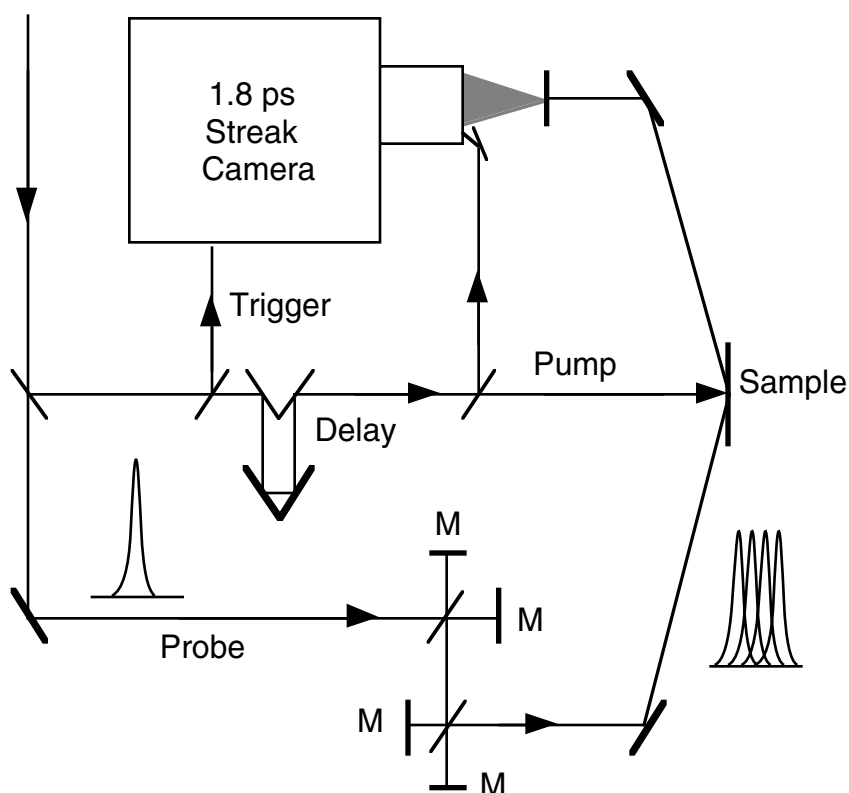


**Fig. 5.2** Experimental setup for picosecond melting studies. A beam splitter divides the 532-nm, 30-ps pulse into pump and probe beams. The pump strikes the single-crystal Si sample at normal incidence after a variable delay. The probe pulse is split into four pulses by a pair of beam splitters and these are recombined to produce a 120-ps probe pulse. The probe beam is incident near Brewster’s angle and images an area around the 100- $\mu\text{m}$  melting spot onto the entrance slit of a streak camera. A portion of the pump beam is directed to the edge of the slit to record the excitation profile.

respect to one another to form a single probe pulse of approximately 120-ps duration. The stretched probe pulse is incident at  $65^\circ$  and focused to illuminate the area around the excited region of the silicon surface.

The pumped area is imaged onto the entrance slit of a streak camera (Hamamatsu Photonics C1587 with Temporal Analyzer unit C2280). Alignment is verified by creating a multiple-shot damage spot on the silicon surface and photographing the spot with the slit opened. A glass slide splits off a portion of the pump beam to a photodiode used to trigger the streak camera. A second slide relays a reflection of the pump beam to the edge of the streak camera entrance slit where it records the pumping intensity profile.

In the streak camera, electrons produced by light focused on a photocathode are accelerated horizontally towards a two-dimensional array of detectors. On the way they are swept in the vertical direction by a ramping electric field that directs the electrons to vertical positions on the detector array that are approximately proportional to delay. The resulting two-dimensional image holds time information on the vertical axis and spatial information on the horizontal.

The time resolution of streak cameras depends on the rate at which the vertical field is swept. The Hamamatsu C1587 has a maximum rated temporal resolution of  $\sim 2$  ps at the highest sweep speed, corresponding to 5 pixels in the image. The resolution is limited by space-charge effects. As a cloud of electrons emerges from the photocathode and is accelerated towards the detection electronics, the individual electrons repel one another, thereby increasing the spatial extent of the cloud and the resulting image on the detector array. Care must be taken, therefore, to ensure that the intensity of light is low enough to avoid significant space-charge broadening of the signal.

## 5.2 Results and Discussion

The streak images of two single-pulse measurements are shown in Fig. 5.3. The time axis is displayed vertically, with time increasing from top to bottom. The full height of the image corresponds to 190 ps. The horizontal axis reflects the spatial profile. The pump pulse is shown on the left side and has a duration of about 30 ps. The stretched probe pulse covers most of the image. The bright part shows where the silicon surface has melted. Spatially it reflects the Gaussian intensity profile of the pump pulse. The time profile allows one to study the melting dynamics.

Both measurements were performed at the same laser fluence of  $0.47 \text{ J/cm}^2$ . In the lower image, some surface irregularity leads to the formation of a surface plasma in the region where the absorbed energy is highest. The plasma absorbs and scatters the incoming probe light, leading to the dark area in the center of the melting region. This clearly emphasizes the need for spatial resolution. An integrating detector would give rise to erroneous conclusions about the reflectivity. [Boyd 1985]

Figure 5.4 shows the reflectivity profile at the center of the melting region, between the two white lines in the upper image of Fig. 5.3. It is calculated by dividing the average signal between the lines to the average signal in the region to the left that does not melt. In this way the temporal variations in the probe pulse intensity are divided out. The reflectivity rises by a factor of 8 to reach the value for liquid silicon near the end of the 30-ps pump pulse.

## 5.3 Conclusions

Single-shot data acquisition using a streak camera represents a significant improvement over the standard detection scheme that averages spatially and temporally over the probing pulse. The streak image reveals both the melting dynamics

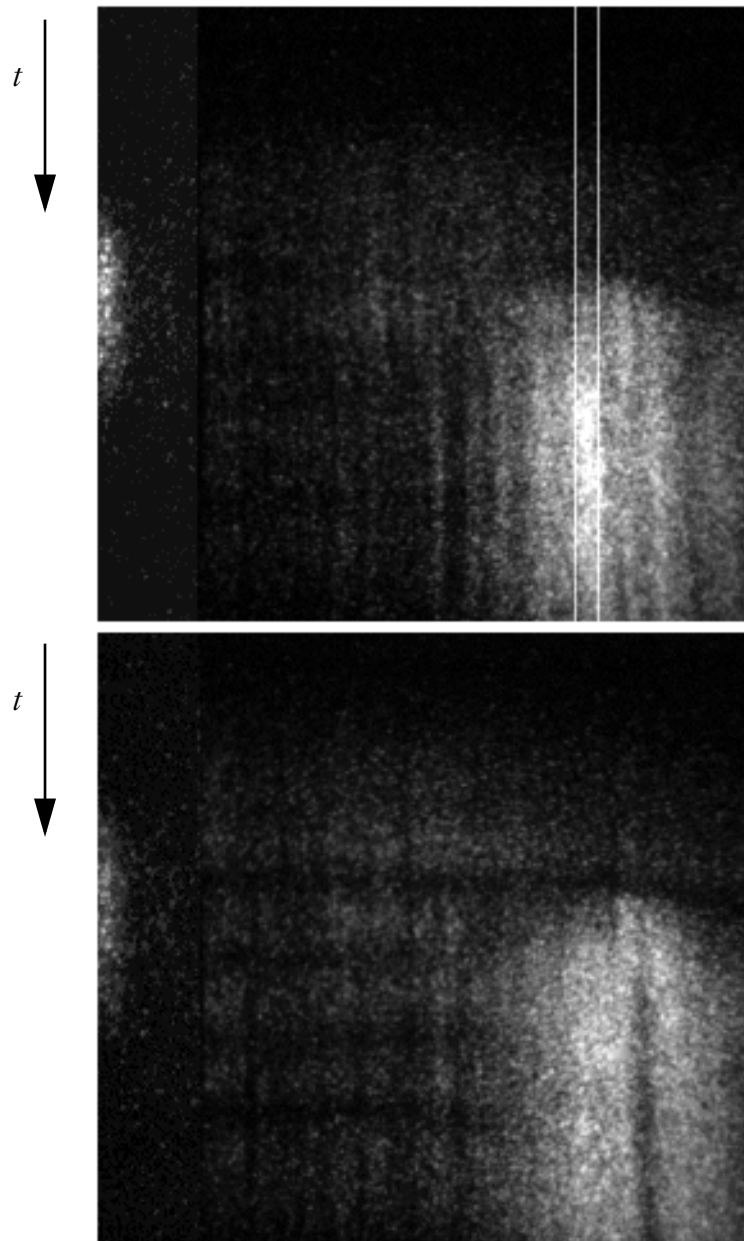


**Fig. 5.3** Streak camera images of the melting silicon surface at an incident fluence of  $0.47 \text{ J/cm}^2$ . The time axis runs from top to bottom and the pumping profile appears at the left. The bright portion of the images comes from the molten region. The data between the white lines in the upper image has been used to compute the reflectivity in Fig. 5.4. The dark streak in the melting region of the lower image results from absorption and scattering by a surface plasma.

and important information about anomalous conditions that could easily lead to incorrect results using the conventional technique. These include absorption and scattering from a surface plasma as well as laser double-pulsing and unsatisfactory mode-locking.

The potential of the technique for reflectivity studies can be realized only with an appropriate probing pulse. Since reflectivity is calculated from the image by forming the ratio of the average data in two spatially separated regions, the probe beam must be smooth across the wafer surface. It must also be smooth on the time scale of the phenomena of interest. By dividing the probing pulse into four mutually delayed pulses, the total duration of the probe is indeed lengthened by roughly a factor of four. However, the combination of pulses does not produce an ideal flat temporal profile. Dark horizontal lines in the images of Fig. 5.3 show that the inten-

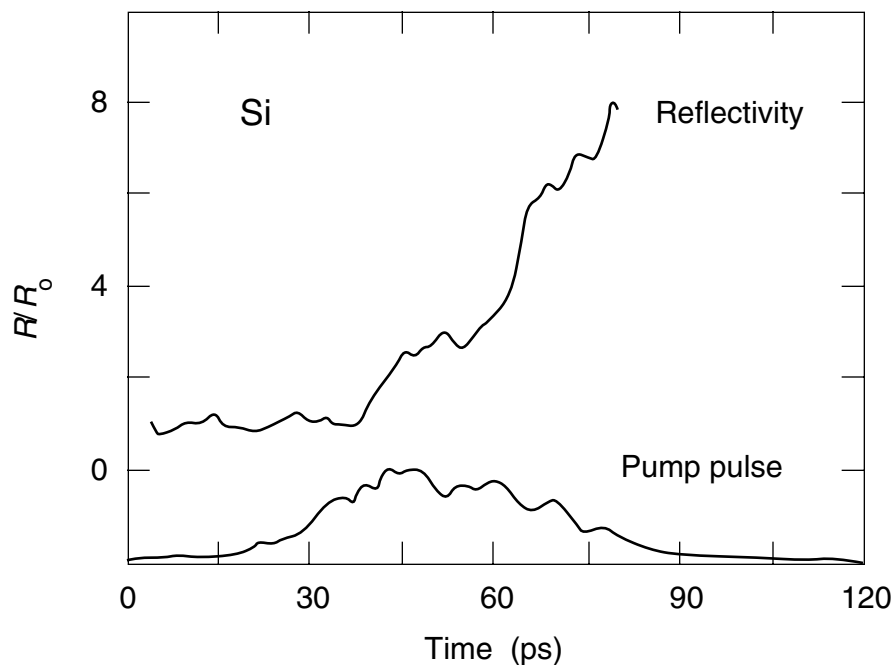


**Fig. 5.4** Reflectivity of silicon during melting with a picosecond laser pulse.  $R_0$  is the reflectivity of unexcited solid silicon. The lower trace shows the intensity of the pump pulse.

sity of the probe varies considerably over its 120-ps duration. Furthermore, curvature in the image plane, caused by space-charge effects and imperfect imaging in the streak camera, can introduce appreciable error and noise in reflectivity data by causing high reflectivity data corresponding to a given time to be divided by reference data at a shifted time. For temporally smooth probing pulses, this would not introduce much error, but when the pulse has structure the distortion can be quite large.

Time-resolved spectral information on the material response would also be useful in studying the carrier dynamics both above and below threshold. Single shot reflectivity spectra could be obtained by using a subnanosecond white light probe and a spectrometer in front of the streak camera. Such spectra could reveal the plasma frequency as a function of time. The difficulty lies in the white light source. The streak camera requires that it be gated in time to begin at the start of the sweep. Light entering the streak unit before the sweep creates photoelectrons that are only imperfectly removed from the region behind the photocathode. As the accelerating voltage is applied to create the image, these stray electrons distort the image and can wash out the true signal entirely. Whereas white light pulses of femtosecond or microsecond duration are relatively easy to produce, it is difficult to generate a 1-ns pulse with picosecond jitter. Solving this problem could open the door to picosecond spectrally resolved studies of a variety of materials under intense photoexcitation and could provide useful information on the PPAR process in silicon.

## Concluding Remarks

The femtosecond experiments on GaAs pose a number of interesting questions. The coincidental agreement between the threshold energy density calculated with the linear absorption constants and by the connected density of states could be investigated by changing the photon energy. For a photon energy near the gap, the density of electrons that can be excited in single-photon transitions can be decreased significantly. The crystal may retain long-range order even after all accessible electrons have been excited to conduction states. Very different behavior might be observed with a pump photon energy near the direct gap at the L point, which would inject electron-hole pairs far from the band-edge states.

Reflectivity studies at different wavelengths of the laser-excited phase of GaAs could help clarify the electronic properties of this highly-excited state. In addition, spectral resolution in below-threshold experiments on both GaAs and Si could yield valuable information on the screening of Auger recombination, and possibly also on plasmon-assisted recombination in GaAs and plasmon-phonon-assisted recombination in Si.

While the basic physics of laser melting with picosecond and longer pulses is well understood, a number of questions remain regarding semiconductors excited both above and below the melting threshold. The reflectivity drop predicted for strong heating of the molten surface layer awaits clear experimental verification. A nanosecond laser system using fiber compression techniques to generate a picosecond excitation pulse could provide the smooth spatial and temporal profile necessary for use with a streak camera, at least at a single frequency. Although a nanosecond continuum probe remains a technological difficulty, spectral informa-

tion could still be obtained at discrete frequencies by harmonic generation and Raman down-conversion.

# Appendix A

## Computer Model for Picosecond Laser Melting of Silicon

As discussed in the first chapter, a great many carrier absorption and scattering processes take place during and immediately following laser excitation of a semiconductor surface. These processes affect the temperature and free carrier density profile inside the material, and therefore the reflectivity of the surface. A number of computer codes of varying sophistication have been devised to understand the carrier and/or melting dynamics and to compare theoretical models to experimental results. [Banfi 1978, Shah 1987, van Driel 1987] On the shortest time scales it is necessary to keep track of the momentum distribution of carriers to account for degeneracy and intervalley scattering rates. Such a computation using a Monte Carlo technique that accounts for electron-electron scattering, electron-polar optical and acoustic phonon scattering, intervalley scattering through the deformation potential, and hot phonon effects has been used to model the transient optical response of GaAs to subpicosecond excitation. [Shah 1987] Many of the picosecond results on silicon have been modeled by the Boltzmann equation in the relaxation-time

approximation by van Driel. [van Driel 1987] While models that keep track of momentum distributions are more detailed and potentially more accurate than simpler schemes, they require greater computational resources and time. We<sup>1</sup> have written a program in the context of the thermal model that calculates the temperature of the laser-excited silicon as a function of depth and time, keeping track of delayed heating caused by Auger recombination and (optionally) plasmon-phonon-assisted recombination (PPAR).

## A.1 Physical Model

In the thermal model, photoexcited carriers are assumed to relax rapidly to the band edge (principally via optical phonon emission), thereby delivering their excess kinetic energy from photoexcitation to the lattice. Hence the absorption of a photon of energy  $h\nu$  delivers immediately the energy  $E \approx h\nu - E_g$  to the lattice in the form of heat. In this expression,  $E_g$  is the energy of the gap, which depends on the temperature  $T$ . Because of degeneracy the equality is inexact; the effective gap has to be increased to account for the Fermi levels of conduction electrons and valence holes. These add an extra factor of  $3k_B T$  to the gap, assuming non-degeneracy. [Malvezzi 1988] Here,  $k_B$  is Boltzmann's constant and a single temperature  $T$  describes the carriers and the lattice. The laser source term can therefore be written

$$W_L(\mathbf{r}, t) = I(\mathbf{r}, t) \alpha(\mathbf{r}, t) \left( 1 - \frac{E_g + 3k_B T}{h\nu} \right), \quad (\text{A.1})$$

where  $I$  is the laser intensity inside the material and  $\alpha$  the linear absorption con-

---

<sup>1</sup> The program was written by Yakir Siegal and Peter Saeta along the lines of the computer code PLASMA described by P. G. Gobbi. [Banfi 1978]

$$I(x) = I_0(1 - R)\exp\left[-\int_0^x \alpha(\xi)d\xi\right] \quad (\text{A.2})$$

Carrier recombination and the temperature dependence of the gap provide additional delayed heating mechanisms, given by

$$W_R = \left[-\left(\frac{dN}{dt}\right)_{\text{Auger}} - \left(\frac{dN}{dt}\right)_{\text{PPAR}}\right](E_g + 3k_B T) \quad (\text{A.3})$$

and

$$W_G = -N\frac{dE_g}{dt}, \quad (\text{A.4})$$

where  $N$  is the density of photoexcited electrons. Neglecting screening, the Auger recombination rate is given by [Malvezzi 1987]

$$\left(\frac{dN}{dt}\right)_{\text{Auger}} = -\gamma N^3, \quad (\text{A.5})$$

where  $\gamma$  is the Auger recombination coefficient.

The rate of plasmon-phonon-assisted recombination depends on both carrier density and temperature, and is given approximately by the expression [Rasolt 1989]

$$\left(\frac{dN}{dt}\right)_{\text{PPAR}} = p_0(N) + p_1(N)T + p_2(N)T^2, \quad (\text{A.6})$$

with

$$\begin{aligned} p_0(N) &= p_{00} + p_{01}N \\ p_1(N) &= p_{10} + p_{11}N + p_{12}N^2. \\ p_2(N) &= p_{20} + p_{21}N \end{aligned} \quad (\text{A.7})$$

The coefficients  $p_{ij}$  in Eq. (A.7) are obtained from curve fits to plots of the PPAR rate; their values will be given in § A.3.

Because of the (approximately) exponential attenuation of the incident laser intensity, thermal and carrier density gradients are established inside the material. Since the typical laser spot size ( $\sim 100 \mu\text{m}$ ) is much greater than the absorption

depth of the laser radiation ( $<1 \mu\text{m}$ ), the lateral flow of heat and carriers can be neglected. The problem reduces to the diffusion of heat (and carriers) in the direction of the surface normal (the  $x$ -direction). This is described by the equation

$$c \frac{\partial T}{\partial t} - \frac{\partial}{\partial x} \left( \kappa \frac{\partial T}{\partial x} \right) = W_L + W_R + W_G \quad , \quad (\text{A.8})$$

where  $c$  is the specific heat and  $\kappa$  the thermal conductivity of the excited material. This equation is highly nonlinear for three reasons: 1) the thermal constants depend on temperature, 2) the delayed heating mechanism expressed in  $W_R$  and  $W_G$ , and 3) the phase transformation that takes place for excitation above the threshold fluence. Consequently, Eq. (A.8) requires a numerical solution.

## A.2 Numerical Method

Equation (A.8) can be solved numerically by dividing the two-dimensional space of time and depth into a discrete grid. Thanks to the one-dimensional character of the diffusion, it is possible to calculate the solution efficiently in a manner that scales linearly with the number of spatial and temporal grid points. Schematically, we have

$$c \Delta T \approx \left[ \frac{\partial}{\partial x} \left( \kappa \frac{\partial T}{\partial x} \right) + W \right] \Delta t \quad , \quad (\text{A.9})$$

and it appears that the computation can be done quite simply by an explicit method. That is, at a given time the temperature distribution is known, so the right-hand side of Eq. (A.9) can be computed directly. For any reasonable time step  $\Delta t$ , however, such an explicit computation scheme is unstable (see *e.g.* Press 1987). By averaging the values of the right-hand side computed at the beginning and at the end of the time step, however, the computation is second-order accurate in time and stable even for quite large time steps. [Press 1987] This is called the Crank-

Nicholson scheme.

It is conventional to use a spatial grid of equally spaced points. Such a grid is ill-suited to the current problem because of the prohibitively large number of grid points required. Because of the strong gradients near the surface, the grid spacing must be quite small. On the other hand, the grid must extend deep enough that elements at the rear do not heat appreciably in order to avoid errors introduced by reflections at the artificial back boundary. Both conditions can be satisfied by using a grid of geometrically increasing steps given by

$$\Delta x_j = (\Delta x)s^j . \quad (\text{A.10})$$

Typical values for the front element width  $\Delta x$  and scale factor  $s$  are 1 nm and 1.15, respectively. A grid of 40 points based on these values extends over 1  $\mu\text{m}$  into the material.

The spatial derivative of the temperature for grid (A.10) is given by expressions of the form

$$\left. \frac{\partial T}{\partial x} \right|_{x=x_{j\pm 1/2}} \approx \frac{\pm(T_{j\pm 1} - T_j)}{2(\Delta x_{j\pm 1} + \Delta x_j)} , \quad (\text{A.11})$$

where

$$x_{j\pm 1/2} = x_j \pm \left( \frac{\Delta x_j}{2} \right) . \quad (\text{A.12})$$

Hence, the conductivity term can be written

$$\left. \frac{\partial}{\partial x} \left( \kappa \frac{\partial T}{\partial x} \right) \right|_{x_j} \approx \frac{(\kappa_{j+1} + \kappa_j)(T_{j+1} - T_j) - s(\kappa_j + \kappa_{j-1})(T_j - T_{j-1})}{(\Delta x_j)^2[(1+s)/2]} , \quad (\text{A.13})$$

where the thermal conductivity at  $x_{j\pm 1/2}$  has been approximated by the average of the conductivities at  $x_j$  and  $x_{j\pm 1}$ .

To implement the Crank-Nicholson scheme, the right-hand side of Eq. (A.13) evaluated at the current temperatures  $\left\{ T_j^n \right\}$  is averaged with the same expression

evaluated at the temperatures  $\{T_j^{n+1}\}$  to be calculated during the  $(n+1)$ st time interval, and the result is inserted into Eq. (A.9). Separating the resulting expression for the unknown  $\{T_j^{n+1}\}$  yields

$$A_j T_{j-1}^{n+1} + B_j T_j^{n+1} + C_j T_{j+1}^{n+1} = D_j, \quad (\text{A.14})$$

where the coefficients  $A_j$ ,  $B_j$ ,  $C_j$  and  $D_j$  are given by the expressions

$$A_j = \frac{-s(\kappa_j^{n+1} + \kappa_{j-1}^{n+1})}{2(1+s)(\Delta x_j)^2}, \quad (\text{A.15})$$

$$B_j = \frac{c_j}{\Delta t} + \frac{(\kappa_{j+1}^{n+1} + \kappa_j^{n+1}) + s(\kappa_j^{n+1} + \kappa_{j-1}^{n+1})}{2(1+s)(\Delta x_j)^2}, \quad (\text{A.16})$$

$$C_j = -\frac{\kappa_{j+1}^{n+1} + \kappa_j^{n+1}}{2(1+s)(\Delta x_j)^2}, \quad (\text{A.17})$$

and

$$D_j = \frac{c_j T_j^n}{\Delta t} + W_j + \frac{[(\kappa_{j+1}^n + \kappa_j^n) + s(\kappa_j^n + \kappa_{j-1}^n)]}{2(1+s)(\Delta x_j)^2}. \quad (\text{A.18})$$

This gives  $m - 1$  equations for the  $m + 1$  different  $T_j^{n+1}$ . Two more equations are provided by boundary conditions at the interface and the end of the grid in the bulk. Neglecting heat transfer to the air in front of the sample, the temperature gradient must vanish at the interface. The exact nature of the boundary condition in the bulk should have negligible effect on the solution for a deep enough grid. To facilitate checking, we have used the same energy-conserving boundary condition at  $j = m$  as at  $j = 0$ . With the addition of these boundary conditions, the tridiagonal system of  $m + 1$  equations has a unique solution that can be computed in a straightforward manner. Starting at the front face ( $j = 0$ ), we have

$$B_0 T_0^{n+1} + C_0 T_1^{n+1} = D_0, \quad (\text{A.19})$$

from which  $T_0^{n+1}$  can be expressed

$$T_0^{n+1} = E_0 - F_0 T_1^{n+1}, \quad (\text{A.20})$$

with

$$E_0 = (D_0/B_0) \quad \text{and} \quad F_0 = C_0/B_0. \quad (\text{A.21})$$

Similarly,  $T_j^{n+1}$  can be expressed in terms of  $T_{j+1}^{n+1}$  as

$$T_j^{n+1} = E_j - F_j T_{j+1}^{n+1} \quad (1 \leq j < m), \quad (\text{A.22})$$

with

$$E_j = \frac{D_j - A_j E_{j-1}}{B_j - A_j F_{j-1}} \quad (\text{A.23})$$

and

$$F_j = \frac{C_j}{B_j - A_j F_{j-1}}. \quad (\text{A.24})$$

At the end of the grid, the second boundary condition is used to solve for  $T_m^{n+1}$ , and then the rest of the  $T^{n+1}$  can be found in reverse order from the set of equations (A.22).

Thus far the temperature dependence of the coefficients  $c$ ,  $\kappa$ ,  $R$ , and  $\alpha$  has been ignored to enable Eq. (A.9) to be solved by linear algebra. This defect can be remedied by a ‘‘predictor-corrector’’ iterative technique as follows. After calculating (predicting) the new temperature distribution  $T^{n+1}$  based on the value of the material parameters at the beginning temperatures  $T^n$ , the average temperature for the time step  $\bar{T}_j = (T_j^{n+1} + T_j^n)$  is computed. This average temperature is then used to recompute (correct) the material coefficients and the tridiagonal system is solved again using the ‘‘average’’ coefficients. This procedure is repeated until the maximum relative difference of temperatures between iterations is less than some tolerance. Although not rigorously equivalent to solving the full nonlinear equation, such a scheme is computationally tractable and for reasonable step sizes should give fairly accurate results. Another method for treating the temperature depen-

dence of the material parameters, in the spirit of implicit differencing, is to Taylor expand the coefficients' temperature dependence, keeping only the linear term. [Press 1987] The conductivity is then approximated by

$$\kappa(T_j^{n+1}) = \kappa(T_j^n) + (T_j^{n+1} - T_j^n) \left. \frac{\partial \kappa}{\partial T} \right|_{j,n}, \quad (\text{A.25})$$

with similar expressions for the other parameters.

When a grid point attains the melting temperature, the heat energy expressed in the right-hand side of Eq. (A.9) is used to supply the latent heat of fusion. Since the gap collapses on melting, the energy stored in the conduction electrons is counted against the latent heat. Until the full latent heat has been supplied, the element's phase is described as "slush" [Wood 1981] and its temperature is held at the melting temperature. After melting, the liquid values of material constants are used. Because melting introduces effective boundaries on diffusion in the interior of the grid, it is helpful to slow the simulation down when the front face attains the melting temperature and continue to use the smaller time step until the melt front has penetrated the surface by several grid spacings.

### A.3 Material Properties

The temperature dependence of the density, specific heat, reflectivity, and to a lesser extent the absorption constant of silicon are reasonably accurately known in the crystalline phase. The following expressions<sup>1</sup> for the specific heat and thermal conductivity come from fits to data in Touloukian 1970

$$c = 0.852 + 1.09 \times 10^{-4} T \quad [\text{J g}^{-1} \text{K}^{-1}] \quad (\text{A.26})$$

<sup>1</sup> All temperatures are in Kelvin and carrier densities in  $\text{cm}^{-3}$ .

and

$$\kappa = 960.2 T^{-1.15} [\text{W cm}^{-1} \text{K}^{-1}] \quad . \quad (\text{A.27})$$

The density of crystalline silicon is given in Glazov 1969

$$\rho = \begin{cases} 2.33 - 4.0 \times 10^{-6} T [\text{g cm}^{-3}] & (T < 874 \text{ K}) \\ 2.37 - 5 \times 10^{-5} T [\text{g cm}^{-3}] & (874 \text{ K} < T < 1683 \text{ K}) \end{cases} \quad . \quad (\text{A.28})$$

The reflectivity and absorption constant of the crystal at 532 nm has been measured by Jellison and Modine under equilibrium conditions, [Jellison 1984] giving the expressions

$$R = 0.35635 + 5.0 \times 10^{-5} T \quad (\text{A.29})$$

and

$$\alpha = 4970 e^{2.326 \times 10^{-3} T} [\text{cm}^{-1}] \quad . \quad (\text{A.30})$$

The free carrier plasma will have some influence on these values, but until the plasma frequency approaches the laser frequency, this effect should be small. This effect is neglected in the program.

The band gap energy decreases with temperature, given by the expression [Malvezzi 1988]

$$E_g = 1.167 - 8.6 \times 10^{-5} T - 2.2 \times 10^{-7} T^2 [\text{eV}] \quad . \quad (\text{A.31})$$

The melting temperature is 1683 K and the latent heat 1800 J/g. [Wood 1984] See also van Driel 1987 for the material properties of crystalline silicon. Finally, the PPAR coefficients of Eq. (A.7) have been obtained by curve fits to plots of the PPAR rate made by Rasolt [Rasolt 1987, Rasolt 1989]. They are

$$\begin{aligned} \{p_{00}, p_{01}\} &= \{-1.48 \times 10^{10}, 8.23 \times 10^{-11}\} \quad , \\ \{p_{10}, p_{11}, p_{12}\} &= \{5.02 \times 10^7, -3.68 \times 10^{-13}, 1.38 \times 10^{-34}\} \quad , \\ \{p_{20}, p_{21}\} &= \{-3.38 \times 10^4, 3.01 \times 10^{-16}\} \quad . \end{aligned} \quad (\text{A.32})$$

The material properties of the molten phase pose a difficult problem. Accurate data on the properties of molten silicon, particularly at elevated temperatures, unfortunately do not exist. The difficulty is discussed by Wood *et al.* [Wood 1984] who observe that the accuracy of available experimental data is insufficient to be particularly useful. Some data on the specific heat for a small temperature range above the melting temperature are available [Touloukian 1970] and have been used to develop the expression

$$c = 0.894 + 9 \times 10^{-5} T \text{ [J g}^{-1}\text{K}^{-1}] \text{ .} \quad (\text{A.33})$$

Using the Wiedemann-Franz law, Wood *et al.* find for the thermal conductivity [Wood 1984]

$$\kappa = 2.97 \times 10^{-4} T \text{ [W cm}^{-1}\text{K}^{-1}] \text{ .} \quad (\text{A.34})$$

Silicon and other zincblende semiconductors contract on melting and expand with temperature in the liquid phase. The data of Glazov *et al.* are described by [Glazov 1969]

$$\rho = 3.21 - 1.43 \times 10^{-4} T \text{ [g cm}^{-3}] \text{ .} \quad (\text{A.35})$$

The reflectivity and absorption constant of liquid silicon at 532 nm have been estimated from a fit to experimental data of Lampert *et al.* [Lampert 1981] using a Drude model of molten silicon, giving

$$R = 1.213 - 3.11 \times 10^{-4} T \quad (\text{A.36})$$

and

$$\alpha = 2.759 \times 10^6 e^{-5.272 \times 10^{-4} T} \text{ [cm}^{-1}] \text{ .} \quad (\text{A.37})$$

## A.4 Results

For an incident fluence of  $0.2 \text{ J/cm}^2$ , which is roughly the threshold fluence for

melting, the program indicates that the surface layer melts to a depth of approximately 20 nm. Traces of temperature as a function of time at the surface and at different depths inside the sample are shown in Fig. A.1. The front ~20 nm of the silicon surface melts by the end of the 20-ps excitation pulse. As a check on the consistency of the simulation, the temperature of the final element of the grid at a depth of 1.3  $\mu\text{m}$  is also plotted. It is seen to undergo a very modest rise, indicating that almost no heat has penetrated to this depth. Therefore, the simulation should not be influenced by the detailed choice of boundary condition at the end of the grid.

A similar plot for an incident fluence of 0.25  $\text{J}/\text{cm}^2$  is shown in Fig. A.1. Due to the strong absorption of pump light in the metallic liquid, the surface temperature

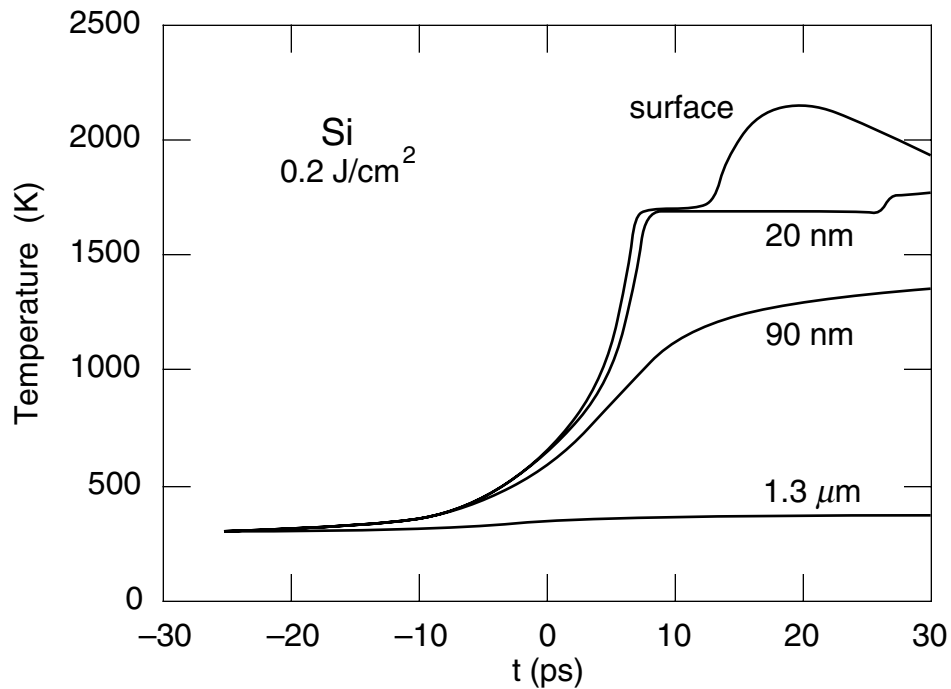


**Fig. A.1** Temperature profiles as a function of time for near-threshold excitation of a silicon surface. The incident fluence is 0.2  $\text{J}/\text{cm}^2$  in a 20-ps pulse (FWHM). The temperature trace at a depth of 20 nm shows that the material at this depth melts just at the end of the pulse. Note that the temperature barely rises at a depth of 1.3  $\mu\text{m}$ , which is the back boundary of the simulation.

rises above 4000 K. While this is qualitatively the correct behavior, the magnitude of the rise must be considered very uncertain because of the large uncertainties in the extrapolation of the material properties of molten silicon above 2000 K.

In general the program indicates that diffusion of heat in the crystalline phase is not very effective in lowering the surface temperature on the picosecond time scale. Although the thermal conductivity rises on melting, the much greater increase in the absorption constant more than offsets the greater efficiency of diffusion and the surface temperature rises strongly, probably well above the vaporization temperature (3540 K) for fluences appreciably above the threshold. As pointed out by Fauchet and Li, [Fauchet 1988] this should produce a drop in electrical conductivity and hence in reflectivity. After the pulse, the surface cools rapidly due to high thermal

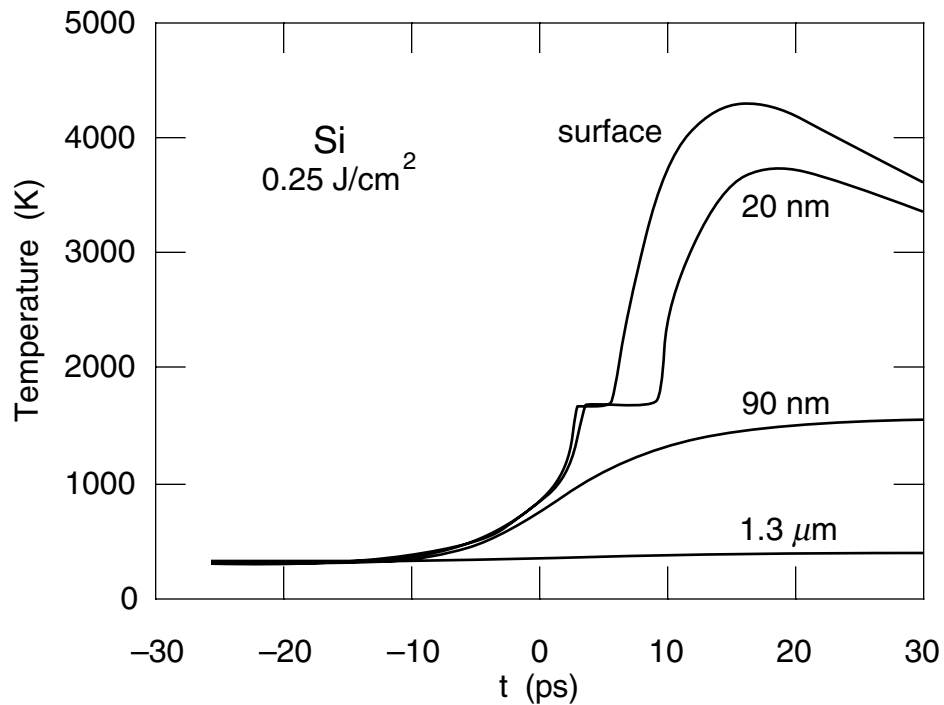


**Fig. A.2** Temperature profiles of a silicon surface at an incident fluence of  $0.25 \text{ J/cm}^2$  in a 20-ps pulse (FWHM). Because of the strong absorption of pump light in the molten phase, the temperature of the liquid rises sharply after melting to a temperature exceeding 4000 K.

conductivity and large temperature gradients in the liquid. The reflectivity should then rise to the peak value for an optically thick layer of molten silicon at the melting temperature and remain at this high level until the surface resolidifies.

## **A.5 Possible Improvements**

Although carrier density is computed during the simulation to handle delayed heating via carrier recombination, the diffusion of carriers is neglected. This can easily be remedied with the same sort of Crank-Nicholson scheme as is used to calculate the temperature. Furthermore, the carrier dependence of the gap and of the optical properties should be taken into account, as in van Driel 1987. Adding a plasma contribution to the dielectric constant from the free carriers, as discussed in Chapter 1, and computing the *p*-polarized reflectivity as a function of time would facilitate direct comparison with experimental data.

Although the model assumes that the temperature remains fixed while the material melts, there is some evidence that the solid material superheats considerably. Kluge *et al.* have performed a molecular dynamics simulation of the laser melting process [Kluge 1987] that suggests that the solid superheats to 2650 K before melting begins. Once melting has started, the temperature reportedly falls to 1750 K, with the excess thermal energy being converted to latent heat. This lowers the latent heat to roughly 930 J/g. Such a superheating mechanism would have the effect of raising the threshold fluence slightly, because the material would have to be heated nearly 1000 degrees above the equilibrium melting temperature for melting to begin to take place.

# References

- Adachi, S., *J. Appl. Phys.*, **53**, 3, R1 (1985).
- Akhmanov, S. A., N. I. Koroteev, G. A. Paitian, I. L. Shumay, M. F. Galjautdinov, I. B. Khaibullin, and E. I. Shtyrkov, *Opt. Comm.*, **47**, 3, 202 (1983).
- Andres, R. P., R. S. Averback, W. L. Brown, L. E. Brus, W. A. Goddard, A. Kaldor, S. G. Louie, M. Moscovits, P. S. Peercy, S. J. Riley, R. W. Siegel, F. Spaepen, and Y. Wang, *J. Mater. Res.*, **4**, 3, 704 (1989).
- Ashcroft, N. W. and N. D. Mermin, *Solid State Physics* (Holt, Rinehart and Winston, Philadelphia, 1976).
- Auston, D. H., C. M. Surko, T. N. C. Venkatesan, R. E. Slusher, and J. A. Golovchenko, *Appl. Phys. Lett.*, **33**, 437 (1978).
- Banfi, G. P. and P. G. Gobbi, *Plasma Physics*, **21**, 845 (1978).
- Bastard, G., *Phys. Rev. B*, **24**, 10, 5693 (1981).
- Bechtel, J. H. and W. L. Smith, *Phys. Rev. B*, **13**, 8, 3515 (1976).
- Becker, P. C., H. L. Fragnito, C. H. B. Cruz, J. Shah, R. L. Fork, J. E. Cunningham, J. E. Henry, and C. V. Shank, *Appl. Phys. Lett.*, **53**, 21, 2089 (1988).
- Bethune, D. S., *Appl. Opt.*, **20**, 11, 1897 (1981).
- Blinov, L. M., V. S. Vavilov, and G. N. Galkin, *Sov. Phys. Semicond.*, **1**, 1124 (1967).
- Bloembergen, N. and P. S. Pershan, *Phys. Rev.*, **128**, 2, 606 (1962).
- Bloembergen, N., R. K. Chang, S. S. Jha, and C. H. Lee, *Phys. Rev.*, **174**, 3, 813 (1968).
- Bloembergen, N., *Mat. Res. Soc. Symp. Proc.*, **51**, 3 (1986).
- Born, M. and E. Wolf, *Principles of Optics* (Pergamon, Oxford, 1980).
- Boyd, I. A., S. C. Moss, T. F. Bogess, and A. L. Smirl, *Appl. Phys. Lett.*, **46**, 366 (1985).
- Brown, W. L., in *Laser and Electron Beam Processing of Materials*, edited by C. W. White and P. S. Peercy (Academic Press, New York, 1980).

## References

- Brown, W. L., in *Energy Beam-Solid Interactions and Transient Thermal Processing*, edited by J. C. C. Fan and N. M. Johnson (North-Holland, 1984).
- Brus, L., *IEEE J. Quant. Electron.*, **QE-22**, 9, 1909 (1986).
- Buijs, M., J.-K. Wang, P. Saeta, and E. Mazur, in *Nonlinear Optics and Ultrafast Phenomena*, edited by R. R. Alfano and L. J. Rothberg (Nova Publishers, New York, 1990).
- Cho, H.-S. and P. R. Prucnal, *Phys. Rev. B*, **36**, 6, 3237 (1987).
- Cohen, M. L. and J. R. Chelikowsky, *Electronic structure and optical properties of semiconductors* (Springer-Verlag, Berlin, 1988).
- Conwell, E. M. and M. O. Vassel, *IEEE Trans. Electron. Devices*, **13**, 22 (1966).
- Danan, G., B. Etienne, F. Mollot, R. Planel, A. M. Jean-Louis, F. Alexandre, B. Jusserand, G. LeRoux, J. Y. Marzin, H. Savardy, and B. Sermage, *Phys. Rev. B*, **35**, 6207 (1987).
- Dawson, P., K. J. Moore, and C. T. Foxon, *SPIE*, **792**, 208 (1987).
- Diels, J.-C. M., J. J. Fontaine, I. C. McMichael, and F. Simoni, *Appl. Opt.*, **24**, 9, 1270 (1985).
- Dingle, R., A. C. Gossard, and W. Wiegmann, *Phys. Rev. Lett.*, **34**, 1327 (1975).
- Downer, M. C., R. L. Fork, and C. V. Shank, *J. Opt. Soc. Am. B*, **2**, 4, 595 (1985).
- Esaki, L. and R. Tsu, *IBM Res. Note*, RC-2418 (1969).
- Esaki, L., *IEEE J. Quantum Electron.*, **QE-22**, 1611 (1986).
- Fauchet, P. M. and K. D. Li, *Mat. Res. Soc. Symp. Proc.*, **100**, 477 (1988).
- Feldmann, J., J. Nunnenkamp, G. Peter, E. Göbel, J. Kuhl, K. Ploog, P. Dawson, and C. T. Foxon, *Phys. Rev. B*, **42**, 9, 5809 (1990).
- Finkman, E., M. D. Sturge, and M. C. Tamargo, *Appl. Phys. Lett.*, **49**, 1299 (1986).
- Fork, R. L., B. I. Greene, and C. V. Shank, *Appl. Phys. Lett.*, **38**, 9, 671 (1981).
- Fork, R. L., C. V. Shank, and R. T. Yen, *Appl. Phys. Lett.*, **41**, 3, 223 (1982).
- Fork, R. L., C. V. Shank, R. Yen, and C. A. Hirlimann, *IEEE J. Quantum Electron.*, **QE-19**, 4, 500 (1983).
- Fork, R. L., O. E. Martinez, and J. P. Gordon, *Opt. Lett.*, **9**, 5, 150 (1984).
- Fröhlich, H., *Proc. R. Soc. London Ser. A*, **160**, 230 (1937).
- Glazov, V. M., S. N. Chizhevskaya, and N. N. Glazoleva, *Liquid Semiconductors* (Plenum Press, New York, 1969).
- Goodnick, S. M. and P. Lugli, *Appl. Phys. Lett.*, **51**, 584 (1987).

## References

- Gordon, J. P. and R. L. Fork, *Opt. Lett.*, **9**, 5, 153 (1984).
- Greene, B. I., private communication (1988).
- Haug, A., *Solid-State Electron.*, **21**, 1281 (1978).
- Hecht, E. and A. Zajac, *Optics* (Addison-Wesley, Reading, 1979).
- Höpfel, R. A., J. Shah, and A. C. Gossard, *Phys. Rev. Lett.*, **56**, 7, 765 (1986).
- Hwang, C. J., *Phys. Rev. B*, **8**, 646 (1973).
- Ippen, E. P. and C. V. Shank, *Appl. Phys. Lett.*, **27**, 488 (1975).
- Jackson, J. D., *Classical Electrodynamics* (Wiley, New York, 1975).
- Jellison, G. E. and Modine, in *Semiconductors and Semimetals*, edited by R. K. Williardson and A. C. Beer (Academic Press, Orlando, 1984).
- Kafka, J. D. and T. Baer, *Optics Letters*, **12**, 6, 401 (1987).
- Kash, J. A., J. C. Tsang, and J. M. Hvam, *Phys. Rev. Lett.*, **54**, 19, 2151 (1985).
- Kash, J. A. and J. C. Tsang, *Solid-State Electron.*, **31**, 3/4, 419 (1988).
- Kash, J. A., private communication (1991).
- Kluge, M. D., J. R. Ray, and A. Rahman, *J. Chem. Phys.*, **87**, 4, (1987).
- Knox, W. H., C. Hirlimann, D. A. B. Miller, J. Shah, D. S. Chemla, and C. V. Shank, *Phys. Rev. Lett.*, **56**, 11, 1191 (1986).
- Knox, W. H., D. S. Chemla, G. Livescu, J. Cunningham, and J. E. Henry, *Phys. Rev. Lett.*, **61**, 11, 1290 (1988).
- Kühlke, D., W. Rudolph, and B. Wilhelmi, *Appl. Phys. Lett.*, **42**, 4, 325 (1983).
- Kuhnle, G., G. Marowsky, and G. A. Reider, *Appl. Opt.*, **27**, 13, 2666 (1988).
- Lampert, M. O., J. M. Koebel, and P. Siffert, *J. Appl. Phys.*, **52**, 8, 4975 (1981).
- Lin, W.-Z., R. W. Schoenlein, J. G. Fujimoto, and E. P. Ippen, *IEEE J. Quantum Electron.*, **24**, 2, 267 (1988).
- Liu, J. M., H. Kurz, and N. Bloembergen, *Mater. Res. Soc. Symp. Proc.*, **13**, 3 (1983).
- Liu, J. M., A. M. Malvezzi, and N. Bloembergen, *Appl. Phys. Lett.*, **49**, 11, 622 (1986).
- Malvezzi, A. M., N. Bloembergen, and C. Y. Huang, *Phys. Rev. Lett.*, **57**, 1, 146 (1986a).
- Malvezzi, A. M., C. Y. Huang, H. Kurz, and N. Bloembergen, in *Beam Solid Interactions and Phase Transformation in Solids*, edited by H. Kurz, G. L. Olson, and J. M. Poate (Materials Research Society, Pittsburgh, PA, 1986b).
- Malvezzi, A. M., in *Excited-State Spectroscopy in Solids* (Soc. Italiana di Fisica,

## References

- Bologna, Italy, 1987).
- Malvezzi, A. M., private communication (1988).
- Migus, A., C. V. Shank, E. P. Ippen, and R. L. Fork, *IEEE J. Quantum Electron.*, **QE-18**, 101 (1982).
- Miller, D. A. B., D. S. Chemla, T. C. Damen, A. C. Gossard, W. Wiegmann, T. H. Wood, and C. A. Burrus, *Phys. Rev. Lett.*, **53**, 22, 2173 (1984).
- Miller, D. A. B., D. S. Chemla, T. C. Damen, A. C. Gossard, W. Wiegmann, T. H. Wood, and C. A. Burrus, *Phys. Rev. B*, **32**, 1043 (1985).
- Minami, F., K. Hirate, K. Era, T. Yao, and Y. Masumoto, *Phys. Rev. B*, **36**, 2875 (1987).
- Murnane, M. M. and R. W. Falcone, *J. Opt. Soc. Am. B*, **5**, 8, 1573 (1988).
- Murnane, M. M., H. C. Kapteyn, and R. W. Falcone, *Phys. Rev. Lett.*, **62**, 2, 155 (1989).
- Oudar, J. L., *Phys. Rev. Lett.*, **55**, 19, 2074 (1985).
- Palik, E. D., Ed., *Handbook of Optical Constants of Solids* (Academic Press, Orlando, 1985).
- Phillips, J. C., *Phys. Rev. Lett.*, **20**, 550 (1968a).
- Phillips, J. C., *Phys. Rev. Lett.*, **166**, 3, 832 (1968b).
- Pierret, R. F., *Advanced Semiconductor Fundamentals* (Addison Wesley, Reading, Massachusetts, 1987).
- Press, W. H., B. P. Flannery, S. A. Teukolsky, and W. T. Vetterling, *Numerical Recipes* (Cambridge University Press, Cambridge, 1987).
- Rasolt, M. and H. Kurz, *Phys. Rev. Lett.*, **54**, 772 (1985).
- Rasolt, M., A. M. Malvezzi, and H. Kurz, *Appl. Phys. Lett.*, **51**, 26, 2208 (1987).
- Rasolt, M., private communication (1989).
- Ridley, B. K., *Quantum Processes in Semiconductors* (Oxford University Press, Oxford, 1988).
- Saeta, P., J. F. Federici, R. J. Fischer, B. I. Greene, L. Pfeiffer, R. C. Spitzer, and B. A. Wilson, *Appl. Phys. Lett.*, **54**, 17, 1681 (1989).
- Schäfer, F. P., *Appl. Phys. B*, **39**, 1 (1986).
- Seeger, K., *Semiconductor Physics: an Introduction* (Springer-Verlag, Berlin, 1989).
- Shah, J., A. Pinczuk, A. C. Gossard, and W. Wiegmann, *Phys. Rev. Lett.*, **54**, 18, 2045 (1985).
- Shah, J., B. Deveaud, T. C. Damen, W. T. Tsang, A. C. Gossard, and P. Lugli, *Phys. Rev. Lett.*, **59**, 19, 2222 (1987).

## References

- Shank, C. V., R. Yen, and C. Hirlimann, *Phys. Rev. Lett.*, **51**, 10, 900 (1983a).
- Shank, C. V., R. Yen, and C. Hirlimann, *Phys. Rev. Lett.*, **50**, 6, 454 (1983b).
- Shen, Y. R., *The Principles of Nonlinear Optics* (John Wiley & Sons, New York, 1984).
- Shimoji, M., *Liquid Metals* (Academic Press, London, 1977).
- Spaepen, F., in *Ultrafast Phenomena V*, edited by G. R. Fleming and A. E. Siegman (Springer-Verlag, Berlin, 1986).
- Stritzker, B., A. Pospieszczyk, and J. A. Tagle, *Phys. Rev. Lett.*, **47**, 5, 356 (1981).
- Tom, H. W. K., G. D. Aumiller, and C. H. Brito-Cruz, *Phys. Rev. Lett.*, **60**, 14, 1438 (1988).
- Touloukian, Y. S. and E. H. Buyco, *Thermophysical Properties of Matter* (Plenum, New York, 1970).
- Treacy, E. B., *IEEE J. Quantum Electron.*, **QE-5**, 454 (1969).
- Valdmanis, J. A., R. L. Fork, and J. P. Gordon, *Opt. Lett.*, **10**, 3, 131 (1984).
- Valdmanis, J. A. and R. L. Fork, *IEEE J. Quant. Electron.*, **QE-22**, 112 (1986).
- Van de Hulst, H. C., *Light Scattering by Small Particles* (Wiley, New York, 1957).
- van Driel, H. M., *Phys. Rev. B*, **35**, 15, 8166 (1987).
- Van Vechten, J. A., R. Tsu, and F. W. Saris, *Phys. Lett.*, **74A**, 6, 422 (1979a).
- Van Vechten, J. A., R. Tsu, F. W. Saris, and D. Hoonhout, *Phys. Lett.*, **74A**, 6, 417 (1979b).
- Van Vechten, J. A. and A. D. Compaan, *Solid State Comm.*, **39**, 8, 867 (1981).
- von der Linde, D. and N. Fabricius, *Appl. Phys. Lett.*, **41**, 991 (1982).
- von der Linde, D., in *Resonances—a Volume in Honor of the 70th Birthday of Nicolaas Bloembergen*, edited by M. D. Levenson, E. Mazur, P. S. Pershan, and Y. R. Shen (World Scientific Publishing Co. Pte. Ltd., Singapore, 1990).
- Wang, J.-K., P. Saeta, M. Buijs, A. M. Malvezzi, and E. Mazur, in *Ultrafast Phenomena VI*, edited by T. Yajimo, K. Yoshihara, C. B. Harris, and S. Shionoya (Springer-Verlag, 1989).
- Weast, R. C., Ed., *Handbook of Chemistry and Physics* (CRC Press, Cleveland, 1976).
- Weiner, A. M., J. G. Fujimoto, and E. P. Ippen, *Opt. Lett.*, **10**, 2, 71 (1985).
- Weisbuch, C., in *Semiconductors and Semimetals*, edited by R. Dingle (Academic, San Diego, 1987).
- Wight, D. R., in *Gallium Arsenide*, edited by M. J. Howes and D. V. Morgan (John Wiley & Sons, Chichester, 1985).

## References

- Wilson, B. A., *IEEE J. Quantum Electron.*, **24**, 1763 (1988).
- Wood, R. F. and G. E. Giles, *Phys. Rev. B*, **23**, 6, 2923 (1981).
- Wood, R. F., C. W. White, and R. T. Young, in *Semiconductors and Semimetals*, edited by R. K. Willardson and A. C. Beer (Academic Press, Orlando, 1984).
- Yoffa, E. J., *Phys. Rev. B*, **21**, 6, 2415 (1980).
- Yoffa, E. J., *Phys. Rev. B*, **23**, 4, 1909 (1981).
- Ziman, J. M., *Principles of the Theory of Solids* (Cambridge University Press, London, 1986).